Scanning Tunnelling Microscopy of Co-impurified Noble Metal Surfaces:
Kondo-Effect, Electronic Surface States and Diffusive Atom Transport

Dissertation
zur Erlangung des Doktorgrades
der Mathematisch-Naturwissenschaftlichen Fakultäten
der Georg-August-Universität zu Göttingen

vorgelegt von
Norbert Quaas
aus Bremen

Göttingen, 2003

D 7

Referent: Prof. Dr. R.G. Ulbrich

Korreferent: Prof. Dr. K. Schönhammer

Tag der mündlichen Prüfung: 10. Dezember 2003

The real voyage of discovery consists
not in seeing new landscapes
but in having new eyes.

Marcel Proust

Übersicht

Die Eigenschaften von nanoskaligen Strukturen auf (111)-orientierten Ag- und Cu-Filmen wurden mit dem Rastertunnelmikroskop (STM) untersucht. Spezielles Interesse gilt den elektronischen Zuständen der Oberfläche und den von eingebetteten Übergangsmetallatomen hervorgerufenen Effekten. Die (111)-orientierten Edelmetalloberflächen besitzen elektronische Oberflächenzustände, die als ein zweidimensionales, nicht wechselwirkendes Elektronengas in den obersten Atomlagen des Kristalls beschrieben werden können. Inselstrukturen von nur einer atomaren Höhenstufe können dieses Elektronengas lokal einschließen, was zur Quantisierung dieser Zustände führt. Diese Quantisierung wird hier anhand von Tunnelspektroskopiebildern sichtbar gemacht. Während solche Messungen nur bei tiefen Temperaturen möglich sind, zeigten vorbereitende Experimente bei Raumtemperatur, dass Inseln hier zum Zerfall neigen und sich innerhalb von einigen Stunden auflösen können. In diesem Zusammenhang wurde in dieser Arbeit ebenfalls die Dynamik von diffusivem Massentransport entlang von Stufenkanten quantitativ untersucht. Wenn die Edelmetallfilme mit Übergangsmetallen verunreinigt werden, etwa mit Co Atomen, entsteht eine verdünnte magnetische Legierung. Die lokalen magnetischen Momente der Fremdatome bringen einen zusätzlichen Freiheitsgrad mit ein, der den Leitungselektronen die Möglichkeit zur Spin-Umklappstreuung an den Co Atomen bietet. Bei niedrigen Temperaturen führt diese Umklappstreuung zu typischem anomalen Verhalten in den physikalischen Eigenschaften der Edelmetallmatrix, bekannt als der Kondo-Effekt. Das Tunnelmikroskop bietet direkten Zugang zu einzelnen atomaren Oberflächendefekten und erlaubt es, die elektronischen Eigenschaften lokal in deren Umgebung zu messen. Die Kondo-Temperatur eines solchen Systems wurde durch Tunnelspektroskopie an einzelnen Co Atomen in einer Cu Oberfläche bestimmt.

Abstract

The scanning tunnelling microscope (STM) was used to investigate the properties of nanoscale structures on (111)-oriented Ag and Cu films. The special focus is on their electronic states and the properties of single transition metal impurities embedded in such films. The (111) noble metal surfaces exhibit electronic surface states that can be described as a two-dimensional non-interacting electron gas located in the topmost crystal layers. Island structures with only monatomic height are capable of confining the surface state electrons, which results in quantization of these states. This quantization is visualized using scanning tunnelling spectroscopy mappings of such islands. While these measurements are possible only at low temperatures, preparatory room temperature studies demonstrate that island structures tend to disintegrate on time scales of several hours. In this context, the dynamics of diffusive mass transport along monatomic step edges has also been investigated in this work. If transition metal impurities such as Co atoms are dissolved in a noble metal film, they form a dilute magnetic alloy. The local moments of the impurity atoms introduce an additional degree of freedom that enables spin-flip scattering of the conduction electrons at the impurity atoms. Towards low temperatures, this spin-flip scattering gives rise to typical anomalies in the fundamental physical properties of the host crystal, known as the Kondo-effect. The tunnelling microscope offers direct access to single surface impurities and allows to locally probe the electronic states in their vicinity. The Kondo-temperature of such a system was determined via tunnelling spectroscopy of single Co impurities in a Cu surface.

Contents

Chapter 1

Introduction

The invention of the scanning tunnelling microscope (STM) in 1981 by Binnig and Rohrer [1] has had an enormous impact on the research in solid state physics and related fields. The possibility to locally investigate a surface with a resolution that ideally is better than one nanometer has led to fascinating insights into the properties of condensed matter even on the atomic scale [2]. Today, scanning probe methods have become a well-established means of gaining spatially resolved information on the properties of a sample surface [3]. A widespread purpose of using a scanning probe microscope (SPM) simply is to acquire images of surface structures on a length scale far beyond the resolution of a conventional optical microscope. But more importantly, SPMs also provide the possibility to conduct local measurements of a large variety of physical properties with nano-scale resolution. An impressive example of how a local quantity like the magnetic stray field can be mapped using a SPM is shown in Fig. 1.1. The two images represent a) the morphology and b) the force gradient of the out-of-plane magnetic field component of a 75 nm Ni film as measured by a magnetic force microscope (MFM) under ambient conditions. In the depicted surface area, the surface profile *and* the magnetic force on the magnetized tip placed 100 nm above the sample profile were recorded simultaneously. The existence of stripe domains with a size of about 210 nm in width is evident, even if a quantitative analysis to recover the exact sample magnetization is a rather complex task and may not always be possible [4].

The magnetic force microscope is one of the many scanning probe instruments that were derived from the scanning tunnelling microscope. From a fundamental point of view, the original STM has a very important capability superior to many of its derivatives: it can selectively probe and spatially resolve the electronic states present at the surface [5]. This is due to the fact that under UHV conditions, the specific electronic wave functions at the clean surface give rise to the tunnelling current that is measured at the tip. Thus, the possibility of measuring voltage-current curves with the STM enables a local electron spectroscopy with a spatial resolution of atomic dimensions. From these tunnelling spectroscopic measurements, detailed information on the electronic properties of the surface can be gained.

In this thesis, the STM was used to investigate the properties of nanoscale metal islands, as well as that of single transition metal impurities embedded in (111)-oriented noble metal films. A new UHV preparation chamber for thin film deposition and the surface preparation of single crystals has enabled STM work on well-defined metal surfaces. Homoepitaxial metal films were evaporated onto single crystal substrates at room temperature, which in case of the noble metals is known to result in 3D island growth [6, 7]. However, at room-temperature this surface morphology is not stable on long time scales. Thermally activated diffusion leads to a rearrangement of step and island structures that is noticeable within minutes using sequential STM imaging. Experiments that require much longer recording times, such as STS mappings taking up to several hours, run into difficulties when the system geometry changes during data acquisition. On the other hand, a satisfactory quality of tunnelling spectroscopy measurements on metal surfaces has been found to require cryogenic temperatures. Therefore, a low-temperature (LT)-STM operating at liquid Nitrogen or liquid Helium temperatures is necessary for successfully probing electronic states. At the same time, this guarantees for the conservation of nanoscale surface structures. Furthermore, cryogenic conditions clearly enhance the quality of data by freezing out lattice vibrations and thus inhibiting surface diffusion through the tunnelling junction. On their [111] surfaces, noble metals exhibit electronic surface states that can be described as a two-dimensional non-interacting gas of quasiparticles in the topmost
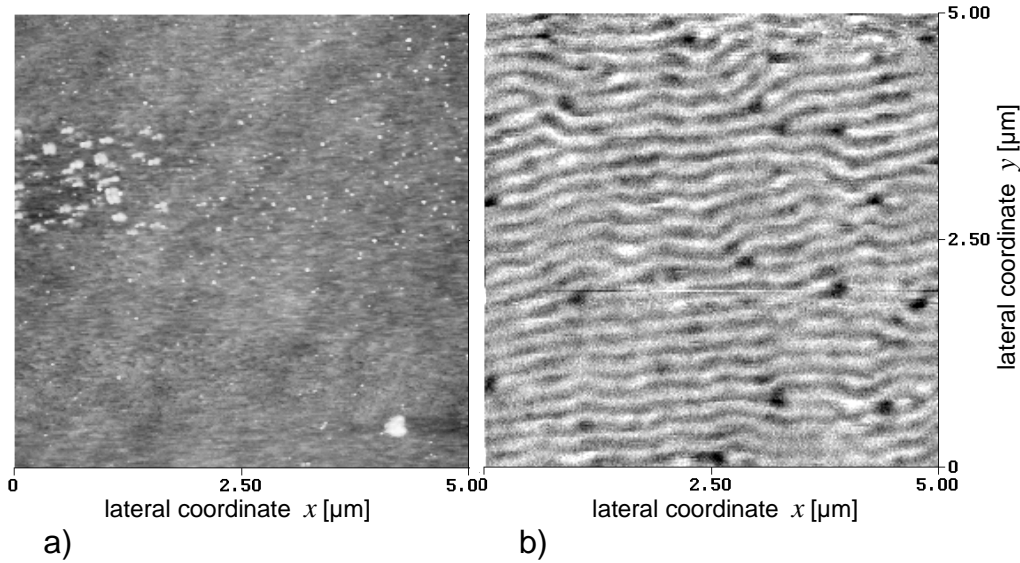
Figure 1.1: *Magnetic force microscopy data recorded on a 75 nm Ni film on Si at room temperature. The surface profile is shown in a), revealing a grainy film structure with some larger surface defects. In b), the force gradient of the magnetic stray field is displayed, which exhibits a streaky magnetic structure of the sample distinct from the morphological appearance in a). The sample was provided by Kun Zhang, II. Physikalisches Institut, Georg-August-Universität Göttingen.*

crystal layers [8, 9]. These states are very well detected with the tunnelling tip, and they prove to be very sensitive to surface defects such as adsorbates, impurities or step edges. Such defects act as scattering centers for the electrons [10], which makes island structures capable of confining surface state electrons to a clearly defined surface area. This results in the formation of quantized electronic states that are found on small islands and on narrow terraces [11]. A single-particle picture is sufficient for a theoretical description in this case. A much more difficult theoretical problem arises, when impurities of transition metal atoms are dissolved in the noble metal, forming a dilute magnetic alloy [12]. The impurity atoms, due to their incompletely filled d-levels, retain a localized magnetic moment in their host crystal environment. The local moment then introduces an additional degree of freedom that enables spin-flip scattering processes of the host's band electrons at the impurity atom. Towards low temperatures, this spin-flip scattering gives rise to typical anomalies in the fundamental properties of the host crystal. The picture shortly outlined here is termed the Kondo-effect, which is an ongoing challenge in current experimental and theoretical work. Kondo-systems represent an example of a highly-correlated electron system which can only be described correctly using a many-body approach. Experimentally, the STM offers the unique opportunity to access *single* surface impurities and to directly probe the electronic states in their vicinity.

The present work thus examines three different aspects of the physics at metal surfaces using UHV-STM and UHV-LT-STS techniques:

1. The thermal stability of island structures on Ag(111) is investigated at room-temperature, clarifying the role of step edge diffusion via sequential STM imaging including the time parameter (Chapter 4).

2. The properties of the quasi-free electron gas formed by electronic surface states, confined to hexagonal islands, are analyzed on Ag(111) and Cu(111) using spatially resolved scanning tunnelling spectroscopy (STS) at liquid Helium temperatures (Chapter 5).

3. The many-body resonance of the Kondo-effect, arising at low temperatures at magnetic impurity atoms, is studied using spatially resolved STS, which for the first time has been measured here at single embedded and buried Co atoms in Cu(111) (Chapter 6).

Chapter 2 starts with an introduction to the principles of STM and STS and gives a description of the data acquisition and processing used in this work. It is followed by Chapter 3, which accounts for the experimental equipment that was developed and operated to prepare the specific metallic surface systems.

Chapter 2

Scanning Tunnelling Microscopy

In this chapter, the principles of scanning tunnelling microscopy are described and the standard model for a theoretical description of the tunnelling current is introduced. The modes of STM operation that were used in this work – constant-current imaging and spatially resolved $I(U)$ spectroscopy – are explained, and their interpretation according to STM theory is discussed, considering some examples from experiment.

2.1   The principle of STM

The operation of the scanning tunnelling microscope (STM) relies on the vacuum tunnelling of electrons between two conductive electrodes in very close proximity. Spatial resolution is introduced by forming one electrode to a very fine, sharp tip, that ideally is terminated by one single atom at the end. This tip, usually consisting of tungsten or platinum-iridium wire, is brought closely in front of the other electrode, the sample, and held there at a distance of several Ångstrøms. At these distances, the electron wave functions of tip and sample, which in the undisturbed case decay exponentially into the vacuum, start to overlap in a region of atomic dimensions. The overlap is synonymous with a finite transfer probability for electrons to tunnel from tip to sample and vice versa. This overlap is the physical origin of a net tunnelling current of the order 10^{-9} A, which is measured when a small bias voltage U is applied between tip and sample. It leads to an exponential dependence of the current on the distance d

$$I_T(z) \propto exp(-2\kappa d) \tag{2.1}$$

with $\kappa = \sqrt{2m|E|/\hbar^2}$ [13]. This current is generated by electrons tunnelling elastically through the vacuum barrier into the unoccupied states of the positively biased electrode. Depending on the spatial extension of the sample wavefunctions, the tunnelling current
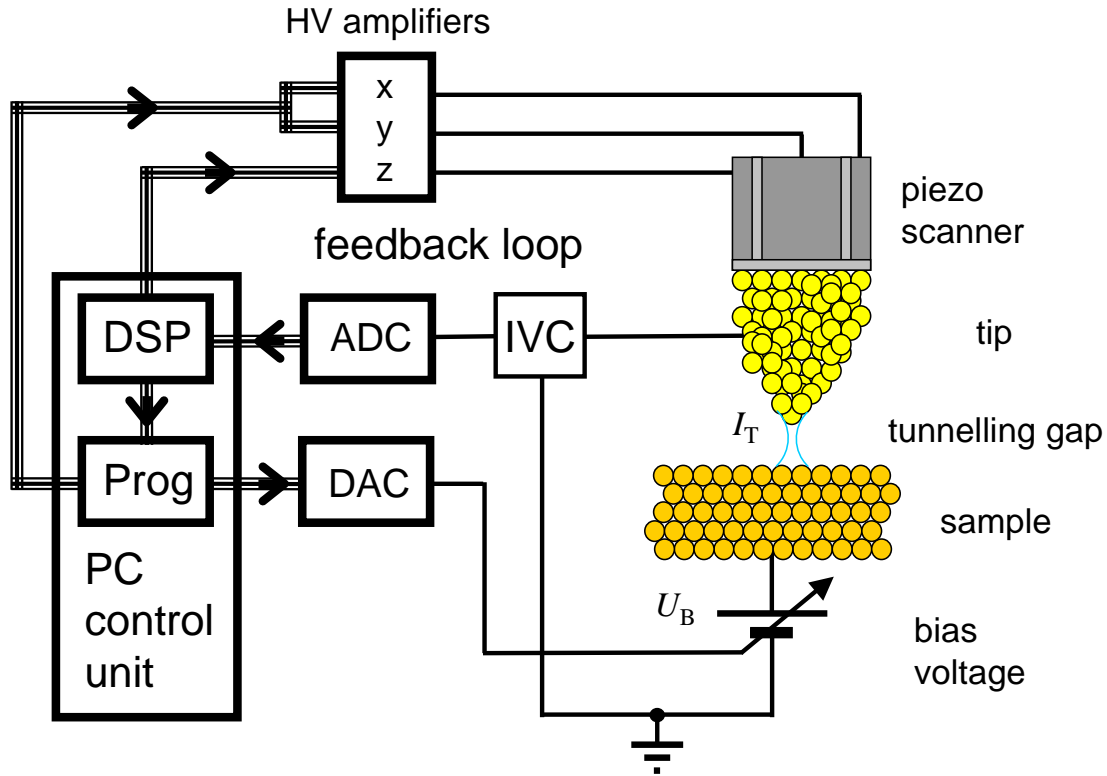
15

Figure 2.1: *The principle of STM (schematically). The tunnelling current is measured using a highly amplifying current-voltage converter (IVC). Atomic scale tip movement is achieved by high-voltage-driven piezoelectric tube scanners. The tip-sample distance is stabilized by a feedback loop using a digital signal processor (DSP).*

can vary locally if the tip is scanned across the surface. In constant current operation, this variation is observed in respective height changes of the tip according to its lateral position on the sample surface. Adjacent line scans of the local tip height assembled to a real space image can, in the limit of ultimate resolution, reveal the atomic-scale structure of the sample surface.

From the technical point of view, the challenge of STM is to stabilize the tunnelling gap with sub-Ångstrøm accuracy using precise mechanical actuators and a feedback circuit. As actuators, high-voltage-driven piezo-electric ceramic tubes are widely used, which provide sufficient stability even at room- and higher temperatures. Since the tunnelling current shows an exponential variation with the tip height, it is a very sensitive input for a feedback loop that actively stabilizes the tip-sample distance. While the tip is scanned by piezo motion in x-y direction, the current is held constant by the feedback loop, that operates on the z-direction and continuously corrects the tip height. An I-V amplifier is employed

to convert the nA current signal to a voltage of the order 1 Volt. This high-gain amplifier is the essential piece of STM instrumentation. The bandwidth of a standard amplifier is on the order of one kilohertz, while very well-designed equipment can reach an order of magnitude better performance. The data acquisition and control unit of the STM is a PC including a digital signal processor board and an external set of highly linear, low-noise AD- and DA-electronics operated with stabilized and decoupled power supplies. Some references characterizing the setup used in this work are given in Section 2.4.1.

2.2   Theory

In contrast to the rather simple principle of STM, a complete theoretical description is comparably complex. With a few simplifications, a widely used basic theory for STM can be constructed describing elastic tunnelling processes. The treatment makes use of the perturbation approach of Bardeen [14]. It was originally meant to describe electron tunnelling in one dimension observed in experiments of metal-oxide-metal tunnelling junctions [15]. Its accurate application in the case of STM requires modifications due to the small distances between tip and sample, which account for the altered potential barrier of the interacting system. This *modified Bardeen approach* gives a simple formulation of the STM problem with reasonable accuracy, even for very narrow-spaced electrodes [13]. The fundamental relations needed for an interpretation of the experiments will be outlined in the following paragraphs.

Transfer Hamiltonian approximation

Based on time-dependent perturbation theory, the tunnelling current can be expressed in terms of the undisturbed eigenfunctions that describe the two isolated subsystems. In the case of the modified Bardeen approach, the treatment of isolated systems is maintained, but a modified tunnelling barrier is introduced and modified eigenfunctions are used on both sides of the barrier [13]. In general, the tunnelling current at a bias voltage U is given by

$$I = \frac{4\pi e}{\hbar} \sum_{\nu,\mu} \left[f(E_\mu^S - E_F^S, T) - f(E_\nu^T - E_F^T, T) \right] \cdot |M_{\nu\mu}|^2 \cdot \delta(E_\nu^T - E_\mu^S - eU) \qquad (2.2)$$

where $f(E,T)$ is the Fermi-function evaluating the occupation probability of the discrete states ν (tip) and μ (sample). The Delta-function represents the condition for elastic tunnelling, and $M_{\nu\mu}$ is the transition matrix element between tip and sample states. This matrix element can be shown to have the form of a surface integral evaluated at a separating surface C dividing both subsystems (see Fig. 2.2), where only the wavefunctions of tip and sample enter:

$$M_{\nu\mu} = -\frac{\hbar^2}{2m} \int_C d\vec{S} \ (\psi_\nu^* \nabla \psi_\mu - \psi_\mu \nabla \psi_\nu^*). \qquad (2.3)$$

In order to get closer to experimental parameters, the summation over discrete states can be replaced by an integration in the energy range over the density of states (DOS), which in its general form is $\rho(E) = \int \frac{d\mathbf{k}}{4\pi^3} \delta(E - E(\mathbf{k}))$. A further simplification is introduced for experiments at low temperatures, where the Fermi-function can be approximated by the step function. The expression for the tunnelling current is then transformed to

$$I = \frac{4\pi e}{\hbar} \int_0^{eU} d\epsilon \; \rho^T(E_F^T - eU + \epsilon) \cdot \rho^S(E_F^S + \epsilon) \cdot |M|^2. \tag{2.4}$$

It is seen here, that the current is determined by the sample DOS ρ^S, but also, equally important, by the tip DOS ρ^T. The spatial dependence of the tunnelling current on a homogeneous surface is still contained in the transition matrix element M. Differentiation yields an expression for the differential conductance dI/dU, which is the quantity determined in the spectroscopic mode. If the bias voltage U is small compared to the barrier height, then

$$\frac{dI}{dU} = \frac{4\pi e}{\hbar} \; \rho^T(E_F^T) \cdot \rho^S(E_F^S + eU) \cdot |M(E_F^S + eU, E_F^T)|^2. \tag{2.5}$$

For interpreting spectroscopic data as being a reproduction of the electronic structure of the sample, the tip DOS must be constant in energy, at least approximately. Deviations should only be a monotonous function within the energy range under consideration. Using a simple 1D tunnelling scheme, the effects of finite bias voltages can be accounted for by multiplying M with a voltage- and energy-dependent barrier transmission factor $T(E, U)$. This issue is looked at more closely in the STS section 2.4.

S-wave tip approximation

The essential term in Eq. 2.4 for describing the unique capability of STM – the atomic resolution imaging of surfaces – is the transfer matrix element M, for which no special assumptions have been made yet. Tersoff and Hamann proposed to model the outermost tip atom with an atomic s-wave function [16]. Later, Chen generalized this approach for orbitals with $l \neq 0$ to explain experimental corrugation amplitudes on close-packed metal surfaces [17, 18]. The treatment is based on Eq. 2.3 and evaluates the wavefunctions on a separating surface in the middle of the tunnelling barrier, where the Schrödinger equation can be reduced to the Helmholtz equation:

$$[\Delta - \kappa^2]\psi(\vec{r}) = 0 \qquad \text{with} \qquad \kappa^2 = \frac{2m}{\hbar^2}|E|. \tag{2.6}$$

The appropriate tip wavefunction for the s-wave is proportional to the zeroth-order Bessel-function of the second kind,

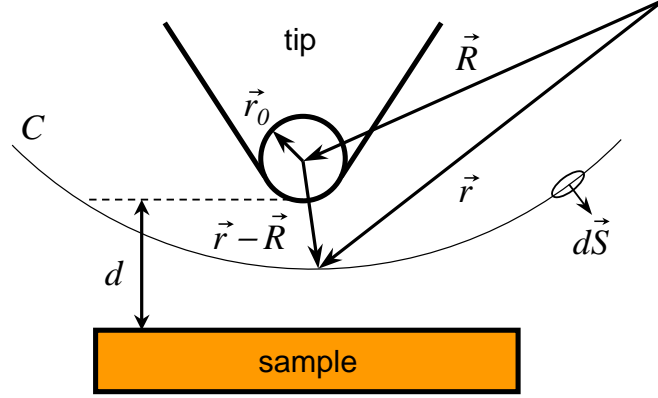$$\psi_\nu(\vec{r} - \vec{R}) = A \frac{e^{-\kappa|\vec{r} - \vec{R}|}}{\kappa|\vec{r} - \vec{R}|} \tag{2.7}$$

Figure 2.2: *Illustration of the tunnelling gap and the definition of the vectors $\vec{R}$, $\vec{r}$, $\vec{r_0}$, the distance d and a separating surface C with the surface element $d\vec{S}$.*

where $\vec{R}$ stands for the position of the outermost tip atom and $\vec{r}$ for an arbitrary position in the tunnelling gap. This function, up to a factor of $\kappa/4\pi$, is the Green's function of the vacuum Schrödinger-equation in the tunnelling barrier. As Tersoff and Hamann have originally shown, the transfer matrix element can then be written as

$$M_{\mu,l=0}(\vec{R}) = -A\frac{2\pi\hbar^2}{\kappa m}\psi_\mu(\vec{R}). \qquad (2.8)$$

Comparing with Eq. 2.4, the tunnelling current depends on the probability amplitude $|\psi(\vec{R})_\mu|^2$ to detect a sample electron at the tip position $\vec{R}$. This matrix element, when inserted into Eq. 2.2, shows that the tunnelling current is proportional to the local-density-of-states ($LDOS$) of the sample as a function of position and energy

$$LDOS(\vec{R}, E_F^S + eU) = \sum_\mu |\psi_\mu(\vec{R})|^2 \cdot \delta(E_\nu - E_\mu). \qquad (2.9)$$

If the tip density-of-states ρ^T is set constant, we see from Eq. 2.5 that the differential conductance dI/dU is proportional to the $LDOS$ of the sample. This result shows us that we have a rather simple rule to interpret experimental data in terms of sample properties, provided that the assumptions for ρ^T which were made above are met.

2.3 Constant-current imaging

The basic mode of STM operation is the constant-current mode, which often is also called *topography mode*. The conductivity of the tunnelling gap is set by two parameters, the bias voltage U_B and the current set-point I_T of the feedback loop circuit. First, the tip is moved towards the surface, until a tunnelling contact is established. Then the feedback
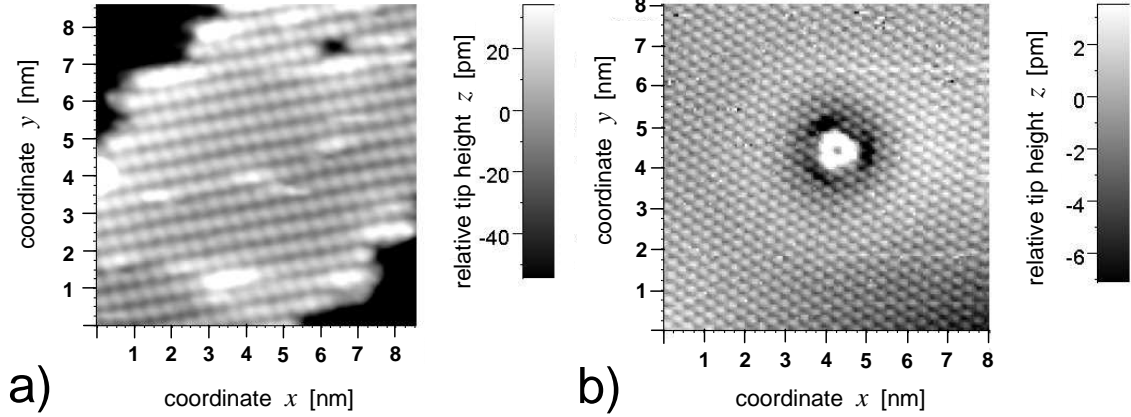
Figure 2.3: *Atomic resolution constant-current images of a) Si-doped n-GaAs(110) and b) Ag(111). a) Filled state image of the dangling bonds associated with the As atoms at $U_{bias} = -2.5$ V and $I_T = 0.3$ nA. A vacancy-donor complex is visible to the upper right as a localized depression [20], while numerous protrusions of the As-lattice indicate negatively charged defects, presumably due to cation vacancies. b) A Co defect atom produces an electronic contrast superposed on the atomic corrugation at $U_{bias} = 0.2$ V and $I_T = 1.0$ nA. On perfect surface areas far from the defect, atomic resolution allows the recognition of the surface lattice structure from the image periodicity. In the vicinity of the defect, Friedel-type screening effects strongly modify the tunnelling current.*

loop is activated to stabilize the tunnelling current at the set-point value. At very low bias voltages, which are commonly used on metallic surfaces, the constant-current z-track of the tip can be interpreted as following a plane of constant $LDOS$ (local-density-of-states) at the Fermi energy:

$$I = const. \;\; \text{and} \;\; U \simeq 0 \quad \Rightarrow \quad \rho^S(\vec{R}, E_F^S) = const. \tag{2.10}$$

However, the tip-height data is not automatically showing the spatial structure of the local *total* charge distribution, which would define the *topography* of the sample [19]. Yet, atomic structures such as surface steps, adsorbed adatoms and vacancies are resolved as local tip-height changes, which obviously deliver data looking like a topographic image of the surface. In this sense, tip-height data seems to indicate the positions of the ionic cores at a surface, but this view is not justified according to the theoretical considerations outlined above. Local variations of the tunnelling current clearly have their origin in the local *electronic* properties and do not reflect the position of the ionic cores of the surface atoms. A proper interpretation of STM data must always be in terms of $LDOS$ variations of the electronic states at the surface, while the tip-height profile might or might not coincide with ionic core positions. Two examples for atomic resolution imaging are shown in Fig. 2.3 recorded on the Si:n-GaAs(110) and the Ag(111) surfaces. Image 2.3 a) has been taken at room temperature and negative sample bias, showing the well-known

voltage-dependent distribution of the As dangling bonds of a compound semiconductor [21], while image 2.3 b) shows the atomic corrugation of an Ag host lattice plus the *LDOS* variation due to a subsurface Co defect atom, which are mixed in a constant-current image.

2.3.1 Multi-bias mode

A variation of the constant-current mode is the *multi-bias mode*. In this mode, a scan line is not only scanned forth and back at a fixed bias voltage. Instead, the bias is switched at the end of a line, and thus, two different constant-current images are acquired at the same time (*dual-bias*). Extending this principle to n multiple setpoint voltages, every scan line is traced n times before moving to the next line, while each trace is recorded at a different voltage. This mode is a very effective tool to quickly get first information if the voltage dependence of surface features shall be investigated. However, the interpretation of these images is not as straightforward as that of dI/dU differential conductance maps.

2.4 Spectroscopic mode (STS)

The theory of the tunnelling current that is summarized above gives a simple result if the bias voltage is close to zero. In practice, this is often not the case, as it is not for the measurements presented in this work. A widely used, simple 1D model for finite-bias tunnelling is summarized here, that also illuminates the general behaviour of experimental dI/dU curves [2]. A one-dimensional approximation of the tip-sample system with distance z is shown in Fig. 2.4. It neglects any realistic modifications of the tunnelling barrier, but gives a qualitative picture in terms of the work functions of the tip and sample materials. The potential diagram in Fig. 2.4 also shows a curve assumed for the sample density-of-states, while the barrier transmission coefficient that depends on energy and on the bias-voltage U, is indicated as horizontal arrows in the gap. The differential tunnelling conductance of this model is given by (see [2])

$$
\begin{aligned}
\frac{dI}{dU} &= \rho^S(z, E_F - eU)\rho^T(E_F) \cdot T(z, E_F - eU, E_F - eU) + \\
&\int_0^{eU} \rho^S(z, E)\rho^T(z, E - eU) \cdot \frac{dT(z, E, E_F - eU)}{dU}dE,
\end{aligned}
\tag{2.11}
$$

and the bias-dependent barrier transmission factor is approximated by that of an effective barrier using

$$
T(z, E, E_F - eU) = exp(-2z\sqrt{\frac{2m}{\hbar}}\sqrt{\frac{\Phi^S + \Phi^T}{2} + \frac{E_F + eU}{2} - E}).
\tag{2.12}
$$

The transmission is highest for electrons at the Fermi-level of the negative electrode and is increasing with U. To a first approximation, the dI/dU signal thus increases quadratically with $|U|$, assuming a structureless tip and sample DOS. In case of both a structured tip *and* sample DOS, the sample features dominate dI/dU at higher negative sample bias, while the tip electronic structure does dominate at larger positive values. The integral remaining in Eq. 2.12 contributes a monotonous voltage-dependent background, so that a constant or monotonous function for the tip DOS is the necessary condition for attributing a local maximum in dI/dU to the properties of the sample.

An example for such finite-bias dI/dU spectra is shown in Fig. 2.5. The data was recorded at room-temperature on a 18 nm thick, LT-grown Co film on a GaAs(110) substrate. The spatially resolved spectroscopy data contain three typical conductivity curves, depicted in a): symmetric, asymmetric and mirror-like asymmetric with a peak at about -0.2 V. Besides the details, the spectra have a U-shaped, approximately quadratic voltage dependence. The tip electronic structure can be assumed to be flat, which is supported by the observation of symmetric curves, that obviously mark ideal metallic behaviour in certain regions on the film. Thus, the details of the spectra, such as the slight asymmetry or the distinct peak seen in other regions, can safely be attributed to sample properties. In the conductivity map shown in b), they consistently appear in compact regions of the sample, therefore evidently not reflecting the properties of the tip. Thus, conductivity maps help to distinguish real features from artefacts in the tunnelling spectra.
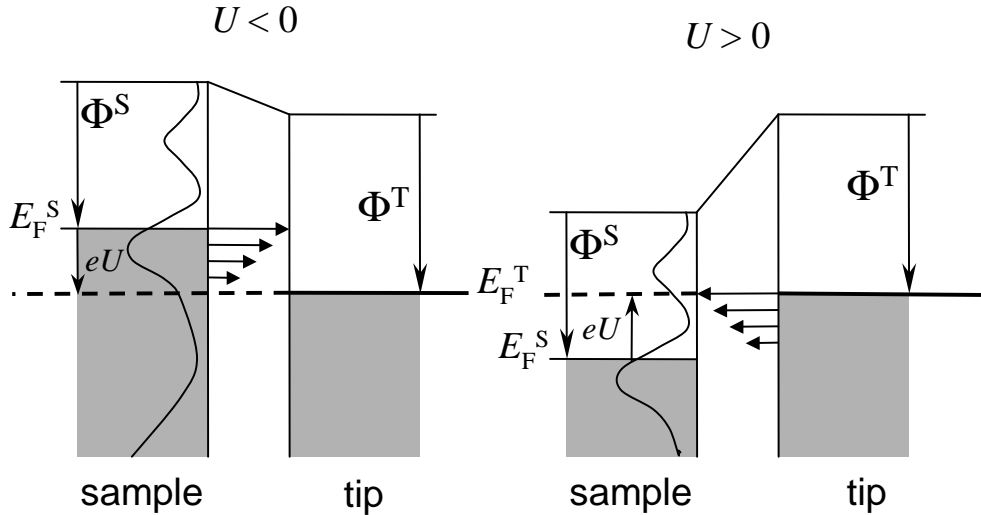

Figure 2.4: *A simple model for STS at finite bias voltages. The barrier is defined by the vacuum work functions Φ_S ans Φ_T of the two electrodes. The arrows in the gap region symbolize the energy-dependence of the barrier transmission factor $T(z, E, E_F - eU)$.*
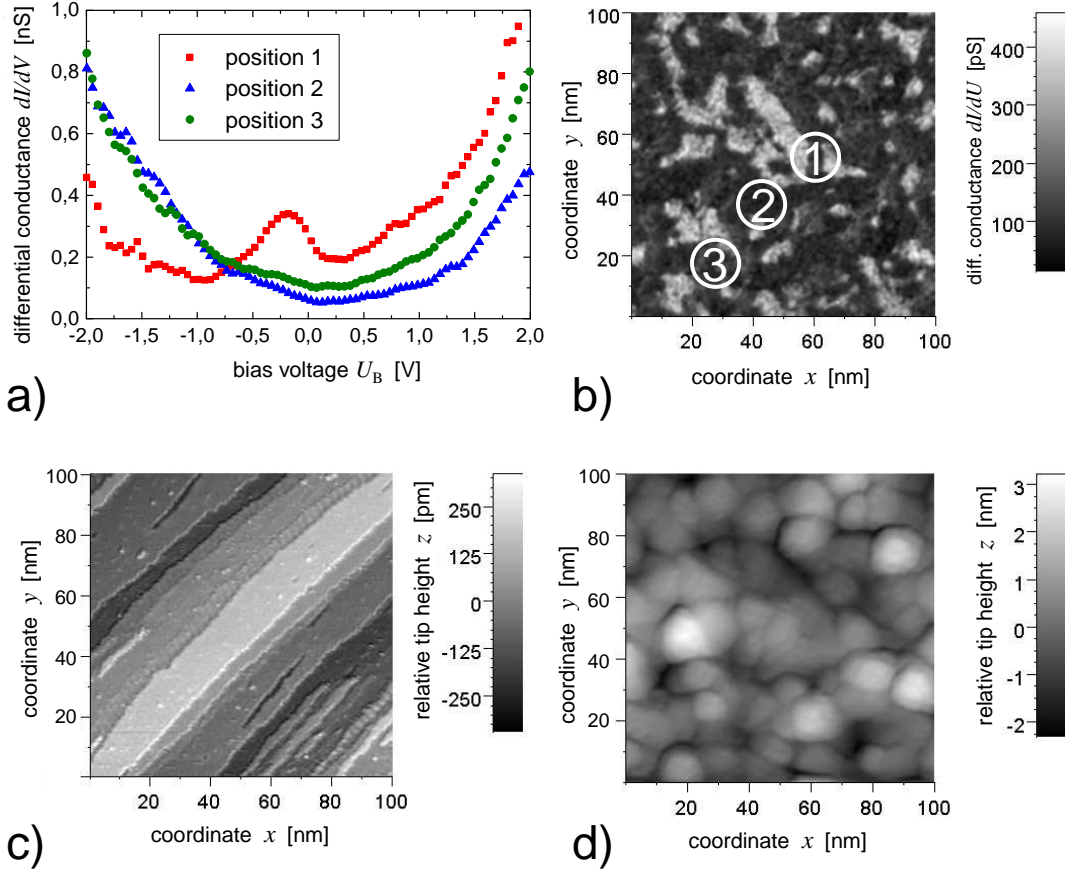
Figure 2.5: *Spatially resolved STS performed on a Co film grown on a GaAs(110) substrate. a) area-averaged dI/dU spectrum at three diferent positions; b) differential conductance map of the sample surface at $U_B = -0.22\ eV$ – light areas correspond to the peak seen in a); constant current images of c) the GaAs substrate and d) the Co film.*

2.4.1 Data acquisition and processing

The dynamic range of the current-voltage converter used in this work comprises four orders of magnitude, with a saturation threshold at 10 nA and the noise of the tunnelling-junction below 5 pA. The bandwidth of the amplifier lies above 10 kHz, which is tunable by the amplifier feedback capacitance [22]. A characterization of the linearity of the current ADC and bias voltage DAC modules has been performed and can be found in [23]. The procedure for spectroscopic data acquisition used here differs from the bias modulation technique with Lock-in detection that is often used on metal surfaces. Instead, a technique was employed that is commonly used on semiconductors, which provides a complete spectroscopic map of the imaged area in a comparably short time. This is of some importance due to the inherent time limitation of low-temperature STM experiments.

The spectroscopic data acquisition is based on the constant-current mode, where current setpoint and bias voltage define the setpoint conductivity. As in the constant-current mode, the image is scanned pixel per pixel, but additionally, a current-voltage curve is taken at every point of the image. For the time that a $I(U)$ spectrum is recorded, having a duration of some ten milliseconds, the feedback loop is deactivated and the tip is held fixed at the distance defined by the setpoint parameters. To give an example, the $I(U)$ data acquisition for a complete 256 by 256 pixel image with a voltage resolution of 100 steps typically takes about 1.5 h. This large data set is to be processed by averaging adjacent spectra to display the mean $I(U)$ curve of a certain surface area. Thus, it is always possible to assign a local spectroscopy curve to a definite position in the simultaneously recorded constant-current image. Since the spectra normally are averaged spatially, the actual resolution shrinks accordingly. The extent of spatial averaging needed for a good quality $I(U)$ curve typically was 7×7 pixels according to 49 single $I(U)$ data sets.

Further processing involves the smoothing of the averaged $I(U)$ curves followed by numerical differentiation to gain the differential conductance dI/dU. This processing is important to get rid of short-period acoustic noise, representing the major noise problem in the spectroscopic measurements. For a smoothing of $I(U)$ curves, two options are available: first, the averaging of n adjacent energy values using a gauss-weighted energy window, and second, the fitting of a simple cubic spline fit to the $I(U)$ data with an error term I_{err} adjusted to the experimental noise level. Mostly, both procedures were applied successively. Adjacent averaging was employed sparingly with $n = 3$ (i.e. the previous and the next data point were accounted for with a weight of 50% each) to largely preserve the original energy resolution. The cubic spline fit was applied in the second stage, using an error term of about $I_{err} \sim 10$ pA to further smooth the experimental curve before the numerical differentiation is performed.

The quality of the smoothing was directly judged from the resulting dI/dU curve. Using this procedure, reliable $LDOS$ information are gained from raw $I(U)$ tunnelling spectra. The information can be displayed in several ways. The local conductance plotted as a function of sample bias is the most common representation of spectroscopic data, and can be seen in Fig. 2.5 a). An extended version of this is the display of adjacent dI/dU spectra in form of a grey-scale plot showing the local conductance as a function of bias and spatial coordinate. The third option to visualize the data is a local conductance map at a fixed bias voltage, which shows the spatial variation of the $LDOS$ as a function of x and y coordinate. An example of this type of representation is shown in Fig. 2.5 b).

Chapter 3

Experimental

This chapter gives a brief report on the development of new experimental equipment for surface preparation and describes the preparation procedures relevant for the following chapters. The goal of the developments was to provide the tools necessary for single crystal preparation and controlled metal film deposition at variable temperature. Some exemplary sample preparation experiments are included in order to demonstrate the instrumental and preparative capabilities. Finally, the low-temperature scanning tunnelling microscope (LT-STM) that was used for most of the experiments is briefly described.

3.1 New sample preparation chamber

The experiments that are presented in the following have been based on the benefits of a newly built UHV sample preparation chamber. The new chamber was designed to allow *in situ* surface preparation of metallic single crystals as well as thin film preparation on top of metal and semiconductor samples. It should match the transfer system of each of the existing UHV microscope chambers for optional use at the room-temperature or the low-temperature STM. In Fig. 3.1, the preparation chamber is shown placed in front of *CRYO1*, the low-temperature STM. The work on this preparation hardware project has been a major part of the laboratory time spent for this thesis, and its results shall be presented in this chapter in some detail.

3.1.1 Concept and UHV system design

The design of the UHV systems that are housing the microscopes originally was tailored for cross-sectional experiments on semiconductor surfaces. A fresh surface is obtained
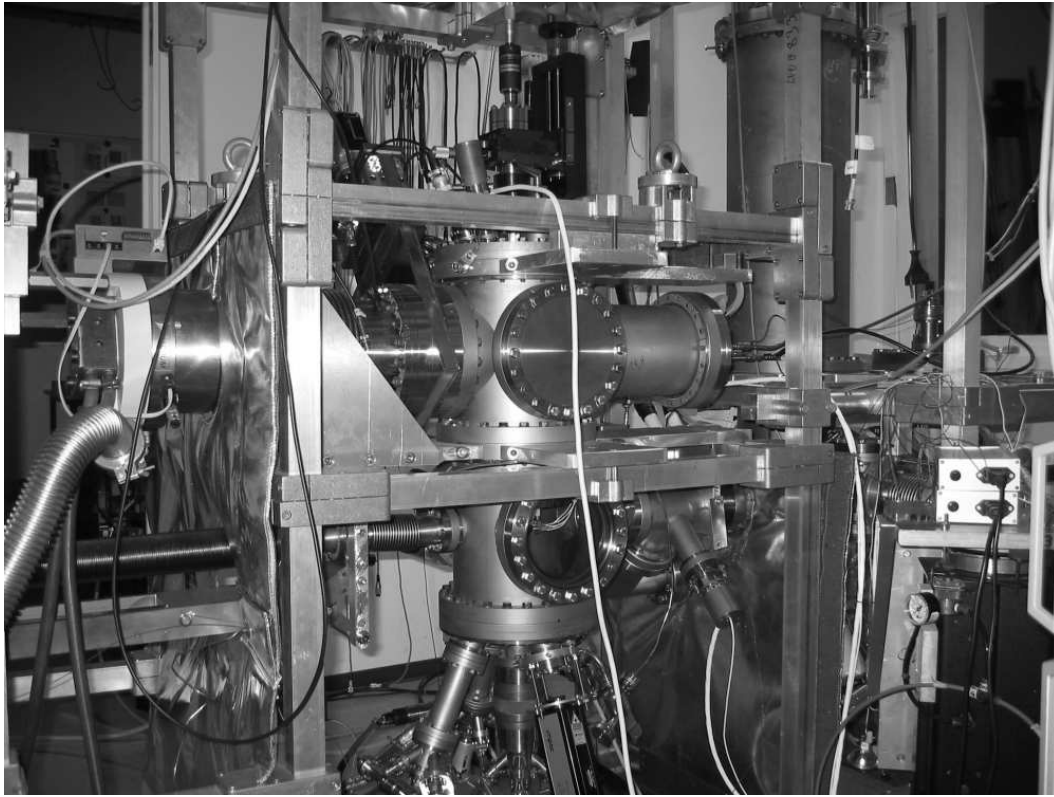
Figure 3.1: *Sample preparation for a low-temperature STM experiment. The cluster flange at the bottom contains evaporators, the ion source and an infrared thermometer for sample temperature control.*

here by *in situ*-cleavage of thin crystal plates that were prepared beforehand under ambient conditions. Further information on these preparation procedures can be found in refs. [24] and [25]. Tips and crystal samples are then transferred into UHV by mounting a second vacuum chamber to a CF 63 vacuum shutter flange of the microscope chamber. A magazine containing eight to twelve items is placed in a bakeable load-lock chamber, which then connects the microscope with the second ion-getter-pumped vacuum chamber, that provides an external tip preparation device. This is all the UHV equipment needed for conventional cross-sectional STM work, since cleavage is carried out directly in the STM chamber. In addition to that, metallic surfaces need several standard preparation tools for achieving clean conditions for proper STM work in UHV. In order to provide these tools and extend our range of experimental skill to single crystal metallic substrates and thin metal films, the new preparation chamber was designed to follow the *connect-on-demand* principle also used for the tip preparation chamber and operate at the CF 63 shutter flange after tip preparation and sample transfer to the microscope chamber is completed. Once baked out, samples can be taken to the preparation facilities one after the other, and put back to the magazine held in the microscope chamber. An overview of

the mechanical design is shown in Fig. 3.2. The transfer is done using a 850 mm linear manipulator, assisted by a second one at right angles with a lift of 100 mm for handling the sample holders in the preparation chamber. Microscope and preparation chamber can be separated and both held at UHV by venting the lock chamber in between. Since the whole preparation chamber is mounted on a rack standing on wheels, it can be rolled back some centimeters, so that the microscope chamber can be lifted up on a pneumatic vibration damping system for tunnelling experiments. Further preparation steps after disconnecting the two systems require a bakeout of only the lock chamber, when the preparation chamber was continuously pumped by the 150-mm-in-diameter turbo-molecular pumping system. Alternatively, to avoid external noise by the mechanical pumping system during the experiments, a LN_2-cooled Ti-pump can be employed to maintain UHV for shorter periods of time. Typical pump-down times from ambient pressure at room temperature (RT) are:

$$\sim \ \ 3 \text{ h at RT} \longrightarrow p_K < 1 \cdot 10^{-6} \text{ mbar}$$
$$\sim 12 \text{ h at RT} \longrightarrow p_K < 1 \cdot 10^{-7} \text{ mbar}$$
$$\sim 72 \text{ h at RT} \longrightarrow p_K < 1 \cdot 10^{-8} \text{ mbar}$$

For bakeout, a custom-made heat-resistent hood is attached to the rack and two regulated 2.5 kW heating fans mounted to the bottom plate ensure an evenly distributed temperature rise to about 150°C. Bakeout time has been varied between 36 h and 72 h, which has been found to have only a small effect on the pressure finally achieved. As a thumb rule, we found that

$$\sim 48 \text{ h at } 150°C \longrightarrow p_K < 1 \cdot 10^{-10} \text{ mbar after cool-down}$$

The base pressure usually reached with a bake-out procedure is $p_K \simeq 5 \cdot 10^{-11}$ mbar about 24 h after terminating the baking. This pressure can be reduced further via LN_2-cooling and Ti-evaporation to $p_K \simeq 2 \cdot 10^{-11}$, which provides a very satisfactory starting point for epitaxy with less reactive samples and compounds.

3.1.2 Preparation equipment

The preparation facilities comprise three independent e-beam evaporators, an ion-beam source (type IQE 11/35 by SPECS) and an infrared non-contact thermometer (type IM 120 by Impac), which are all combined in a five-port CF200 cluster flange at the bottom of the main chamber. The angle of the ion source axis to the crystal surface normal is 25°, for the other components it is 15°, except for the central Cu evaporator, that points in surface normal direction. The top flange carries a x-y-z-manipulator with a heating-cooling-contacting device for sample holders. In the following paragraphs, these components are described starting with the new sample holder.

a)   turbo pump (not shown)
b)   850 mm manipulator
c)   Co evaporator
d)   Cu evaporator
e)   ion sputter source
f)   transfer lock chamber
g)   LN$_2$ shield & Ti pump
h)   sample positioning
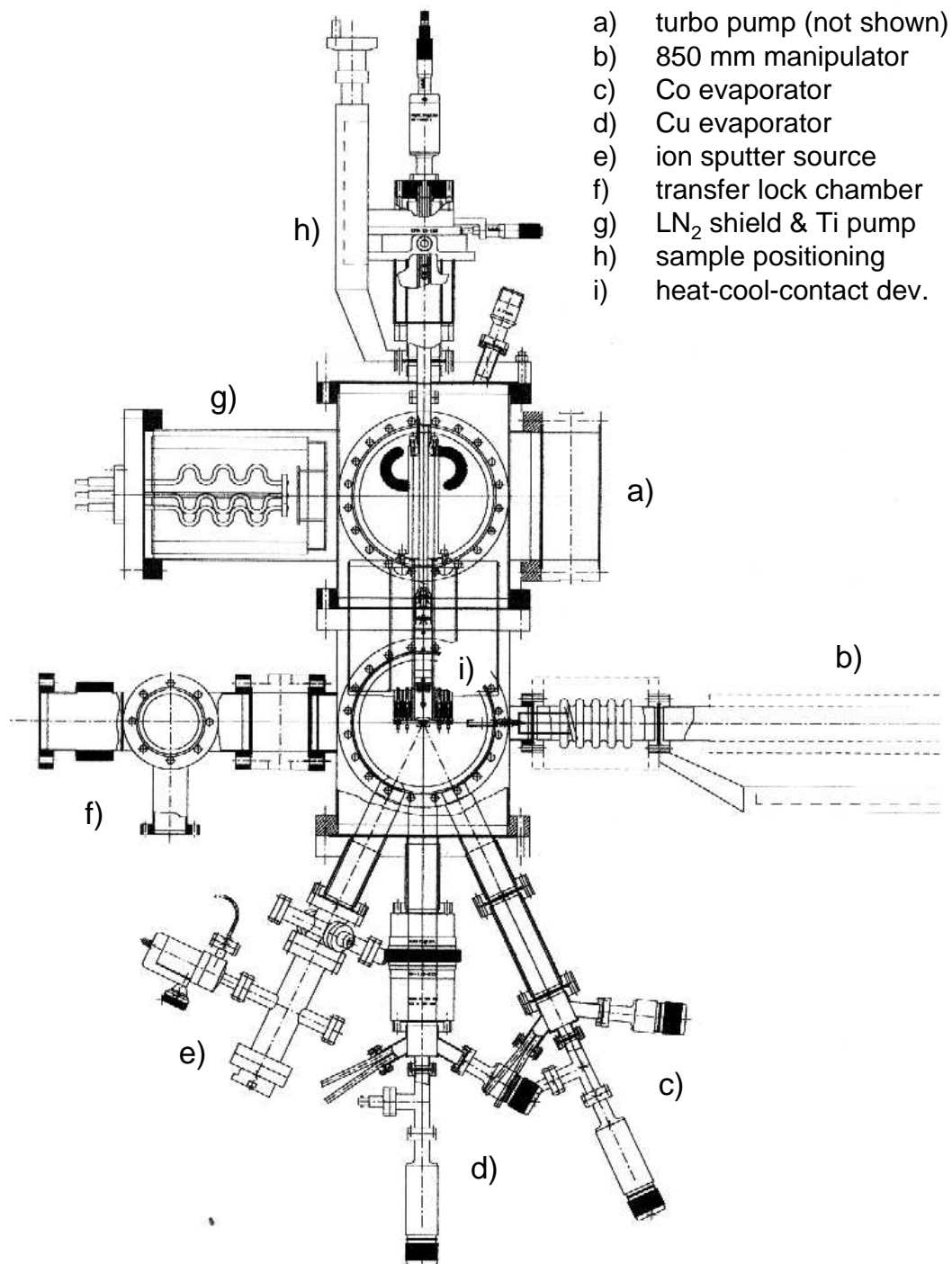i)   heat-cool-contact dev.

Figure 3.2: *Overall view of the preparation chamber. Its rollable rack and the CF150 turbo-molecular pump are not shown. The manipulator on top of the chamber holds the heating-cooling-contacting device for sample holder pick-up.*

Low-temperature sample holder

Single crystals were fixed in a newly developed sample holder that was designed for most efficient heat transport off the sample making it suitable for low-temperature application. The sample holder is schematically shown in Fig. 3.3. The disk-shaped single crystals are also accessible from the backside through a round hole in the 3.5 mm stainless steel base plate, which is necessary for electron beam heating. A 1 mm thick molybdenum top plate tightly presses the rim of the crystal onto a sapphire ring, that combines electrical insulation with good thermal conductivity. It is stacked on top of a replaceable stainless steel ring for easy height adjustment and screwed to the base plate with two 1.6 mm threads using sapphire isolation beads. Silver foil is used to enhance the thermal conductivity at the material junctions. In case of the Ag crystal, the Mo top plate was covered with a thick silver film, to avoid Mo contamination by secondary sputter effects from the plate surface. For the Cu crystal this problem is circumvented by its hat-like shape, which places the crystal surface above the Mo plate, so that straight trajectories from Mo to Cu surface do not exist.
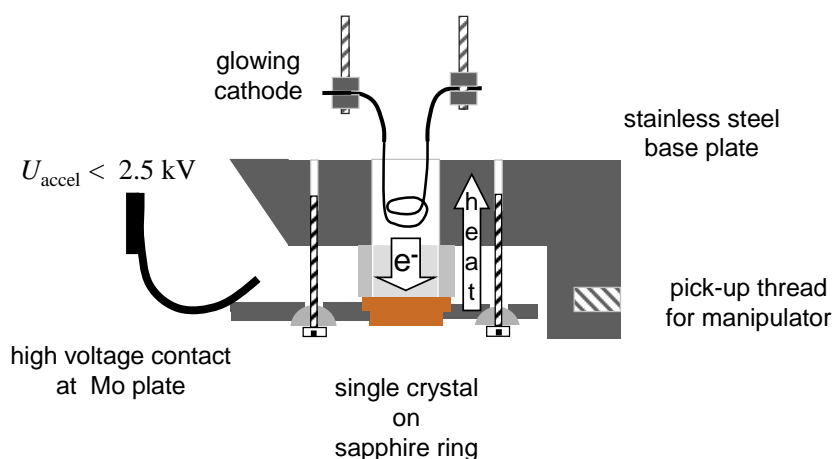
Figure 3.3: *The new single-crystal sampleholder with sapphire isolation providing best thermal properties. HV contact and inserted filament for backside electron beam heating are shown in operation position.*

Heating-cooling-contacting device

For UHV preparation, the crystal holders are placed in a multi-purpose pick-up device that is positionable around the centre of the preparation chamber. It consists of a 5 litre LN_2 tank providing a setup for e-beam heating and additionally grants electrical

contact to the sample holder via six independent contact pins. With a special six-terminal sample holder that is described in [25], six electrodes are available at the sample. This possibility has not been used in the present work, however, one of the electrical pins has been connected to a Mo finger used to contact the crystal during the sputtering and heating procedures. While sputtering, this contact was shorted to ground through a micro-Amperemeter, which avoids charging of the crystal and gives a measure for the ion-beam flux to the sample surface. For the e-beam heating, it delivers the acceleration voltage to the crystal. Through the back hole in the sample holder, a U-shaped thoriated tungsten filament is brought close to the back side of the single crystal. A sketch of this setup is given in Fig. 3.3. Voltages up to 3.5 kV were applied to the crystal, and depending on the filament-crystal distance, currents up to 50 mA have been achieved, and even more is possible. This gives a wide range of possible heating parameters, and it was found that an e-beam with a power of 12.5 W corresponding to 5 mA at 2.5 kV were enough to heat the single crystals to about 800 K. The heating process was conducted manually while making use of a pyrometric temperature control.

Temperature control and calibration

The temperature measurement on the shiny polished crystal surfaces was done optically using an infrared pyrometer. The digital instrument is mounted at the vacuum chamber in front of a CF35 standard viewport and focused on the heated crystal surface at a distance of 25 cm. Its temperature range stretches from $160°$C to $1200°$C. In our setup,
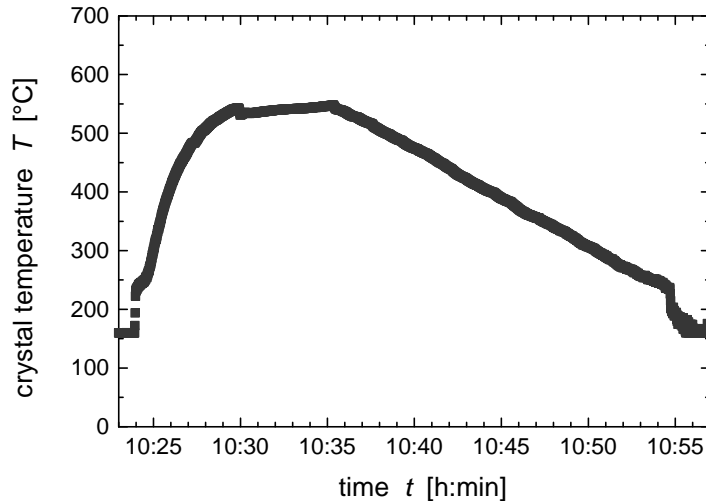

Figure 3.4: *Temperature-time curve showing one annealing step for the Cu crystal. The discontinuities at beginning and end mark the switching of the filament. Cool-down speed here is about 0.3 °C per second.*

we found that indirect thermal radiation of the bright hot tungsten filament, obviously reflected off the chamber walls, produces an offset signal of about 250°C. This signal could not be suppressed by adjusting the focusing unit of the pyrometer, although it had no direct sight of the filament. Temperature readings can therefore considered to be accurate only above 300°C, where this background signal becomes negligible. The calibration of the pyrometer is performed by adjusting a single parameter, the emmissivity ϵ of the surface. Ideally, the emmissivity should be close to 1, which corresponds to the emission characteristics of a black body. A clean metal surface, however, is rather described by an emmissivity close to zero. In order to determine the correct value for the emmissivity parameter, a calibration heating series under UHV conditions was performed using a crystal holder carrying a polished Cu dummy crystal with a thermocouple attached to it. The thermo profiles measured with both methods were adjusted to coincide by variation of the emmissivity parameter in the pyrometer setup. This resulted in an emmissivity $\epsilon_{Cu} = 0.11$ for the Cu crystal, which also is the lowest number that the pyrometer accepts. Using this value also for the Ag crystal at identical heating power resulted in about 150°C lower temperature readings, which shows that the emissivity of clean silver is even lower. Under these circumstances, we relied on choosing identical the e-beam powers, thereby heating the Ag crystal to similar temperatures as the Cu crystal.

Epitaxy instrumentation

The three electron-beam evaporators were acquired commercially, but turned out to have a large number of serious faults that were revealed only time after time. The list of defects starts with forgotten welding seams and sloppy workmanship at electrical components, contains an inoperative water cooling leading to overheating and damage of one head, an unsuitably slow flux regulating unit, and ends with solderings using inadequate material that caused micro-leaks after a bakeout procedure, making the required UHV conditions unreachable. After time-consuming fixation of these defects, we achieved to make a reliable set of instruments out of what was delivered commercially. The evaporators are designed for use with crucibles or rods. The low-melting noble metals require Ta or Mo crucibles, while Cobalt was inserted as a rod. The control over the deposition rate is attained using an electrode placed to the sides of the orifice, which geometrically catches a marginal portion of the vapour beam (see Fig 3.5). A fraction of the emerging atoms is ionized by the electron beam, which results in a tiny positive charge that is brought onto the electrode per time interval. At the same time, the electron cloud produced by the filament greatly overcompensates this charge on the electrode, if not a negative repulsion voltage is applied. A potential of about -20 V is sufficient to measure only the positive charge coming from the ionized vapour with a nano-Amperemeter. This current gives a measure for the deposition rate, which has to be determined by calibration experiments. A new setup for simultaneously measuring and displaying the flux at three evaporators and regulating the power supplies for constant fluxes has been built, and is described in [23]. Additionally, an electronic shutter control has been realized, that enables precisely timed deposition to
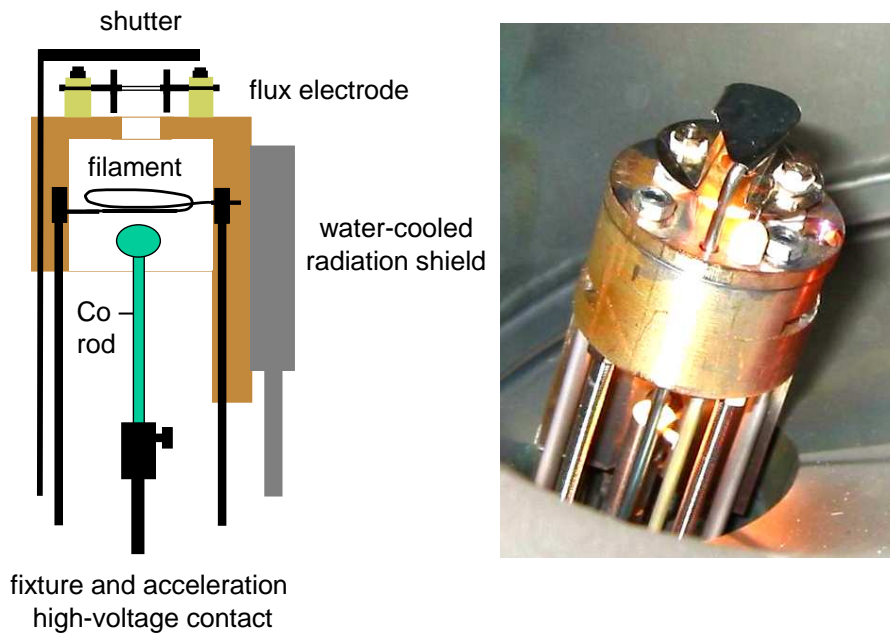
Figure 3.5: *Constructional sketch and view of one evaporator in operation. A linear feedthrough enables positioning of the rod to the filament. In the case of Co, its end is molten down to a stable Co bead after the first heat-ups.*

Figure 3.6: *Preparation chamber pressure vs. measured flux electrode current at the Cu evaporator. The graph suggests an exponential increase of Cu flux and a linear dependence of the chamber background pressure parametrized with the evaporant temperature.*

an accuracy of better than 100 ms [23]. In preliminary deposition experiments, it turned out that the flux calibration strongly depends on the emmission current hitting the target, on whether crucible or rod is used, and on their position and geometry. Therefore, two calibrations were made for 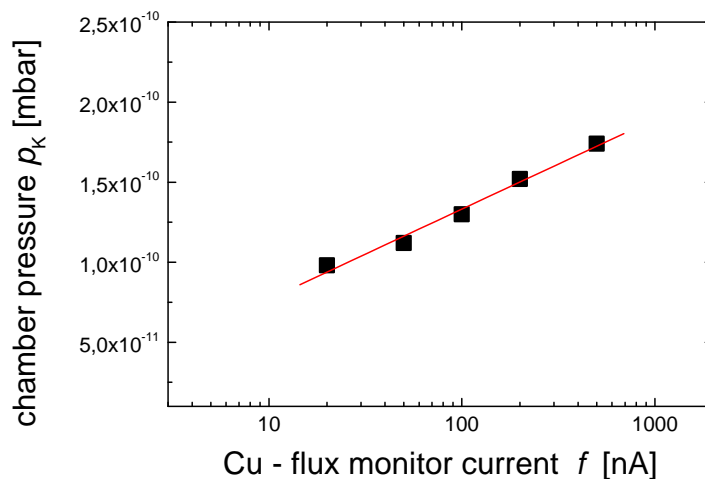the Cu (crucible) and the Co (rod) evaporator. In order to save time, the calibration gained for Cu was assumed to be a good approximation also for the very similar Ag evaporator. The calibration experiments were executed following this scheme:

- Evaporation of four films onto partly covered glass substrates at room-temperature, using different deposition fluxes f at an emmission current of ~ 20 mA. Deposition time Δt is adjusted correspondingly, assuming a linear dependence, to produce identical thicknesses ($d > 10$ nm).

- Measurement of the optical density of the films in a transmission experiment using 632.8 nm wavelength to verify the identical thickness of all four films. Has to be done very quickly under ambient conditions, since in contact with air thin films degrade within only few hours. An *in situ* measurement resolves this problem.

- Absolute measurement of the thickness using a well-calibrated atomic force microscope (AFM) at the sharp lateral transition from film to substrate that was prepared by partly covering the substrate. Metal films show a grain structure on the nanometer scale, which can be averaged to a mean thickness d of the film on the substrate.

Generally, the assumption of anti-proportionality between evaporation time Δt and measured flux f is validated by the transmission experiments. However, a local gradient in the films was observed, which is considered to be a result of non-ideal positioning of the substrates in front of the evaporator orifice. The height measurements of the Cu films via AFM gave us thicknesses between 16 and 20 nm, resulting in $d_{aver} = 18 \pm 2$ nm. We note in passing that under the optical microscope, slowly deposited Cu films seem to oxidize less quickly under ambient conditions than fast-grown ones, since degraded regions visible as blue-green areas increase with reduced deposition time. Finally, we can give the following relations between thickness d, flux f and deposition time Δt for Cu and Co films, respectively:

$$d_{Cu} = 2.8 \cdot 10^{-6} \cdot f_{Cu} \cdot \Delta t \tag{3.1}$$

$$d_{Co} = 4.8 \cdot 10^{-5} \cdot f_{Co} \cdot \Delta t \tag{3.2}$$

The overall error in d from the experimental calibration is estimated to be 10 to 15 percent.

3.1.3   Surface preparation

Single crystals

Noble metal single crystals are widely used as sample and substrate materials in STM work. A major advantage of noble metals is their chemical stability, which ensures a good cleanliness of once prepared surfaces in UHV. We used Ag and Cu single crystals (fcc) in (111) orientation, which expose close-packed surfaces without reconstruction. The procedures for achieving atomically clean surfaces for these materials as well as a large number of other elements are compiled in a comprehensive review article by Musket *et al.* [26]. We used commercially available single crystals, purchased from MaTeck, Jülich. Specifications were: 9 mm in diameter, 1 mm thickness, pre-polished to a roughness below 30 nm, (111)-oriented to an accuracy of 0.1°. In case of the Cu crystal, a heating procedure in a 1:25 ratio hydrogen-argon forming gas at atmospheric pressure was necessary to remove abundant residual impurities, presumably sulphur or carbon, from the crystal surface. Our standard cleaning procedure in UHV were cycles of sputtering with Ar^+ ions followed by short annealing to 800 K. Sputter parameter were 2 μA of 700 eV Ar^+ ion flux hitting the sample holder for about 20 minutes. Heating was performed by e-beam bombardement from the backside resulting in a temperature curve shown in Fig. 3.4. The targeted annealing temperature was reached after some minutes and then held constant for 4 – 6 minutes. This was followed by a slow cool-down extending over 10 to 20 minutes with an approximately linear temperature decrease.
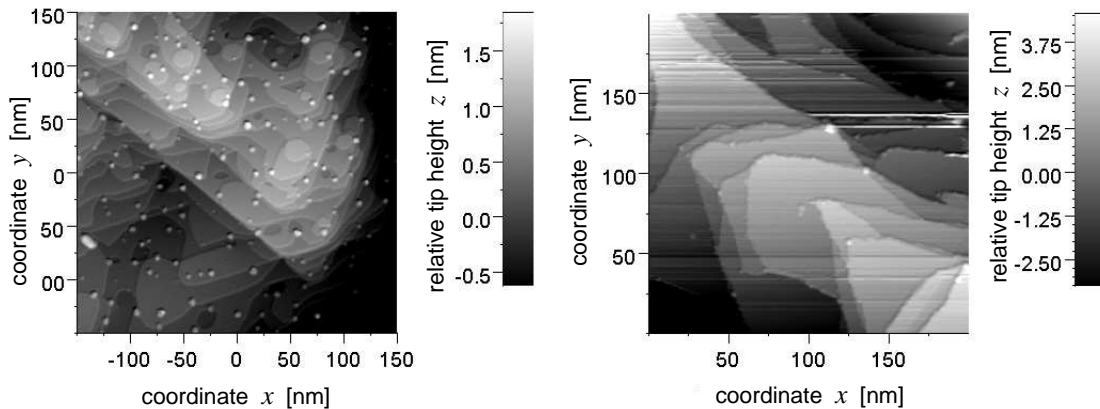

Figure 3.7: *STM topographies of the Cu(111) crystal surface. On the left, bulk impurities have accumulated at the surface by long-time heating. The right part shows the crystal surface after having been cleaned using forming gas and employing UHV preparation with short annealing intervals.*
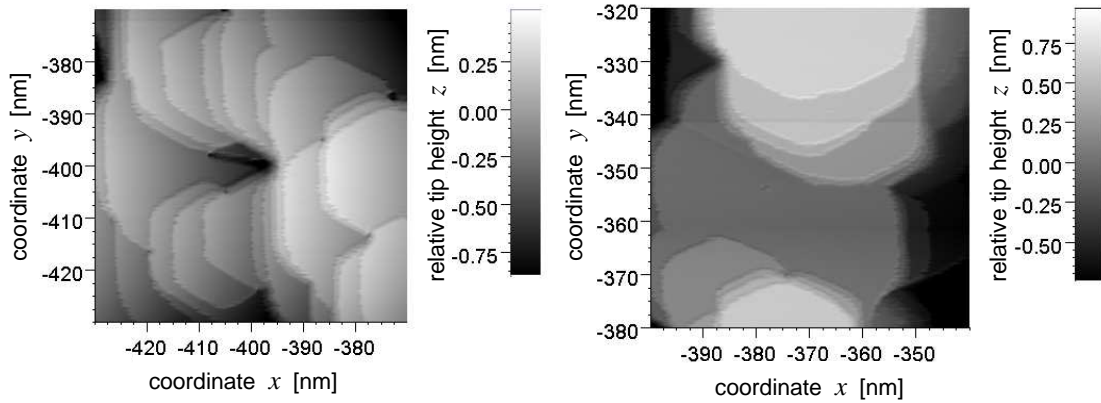
Figure 3.8: *STM topographies of a clean, 18 nm thick Cu film deposited on Cu(111) at a substrate temperature of 80° C and a flux electrode current of 1.8 μA corresponding to 0.025 ML/s. Large stacked hexagonal island structures have developed. On the left, steps converge in the center of the image due to a residual substrate defect.*

Thin films

Deposition of thin metal films was carried out with utmost care for achieving highest film quality and keep contamination as low as possible. The use of purest evaporant materials was combined with a careful outgassing procedure. The procedure starts during cooldown after bakeout with degassing the evaporator heads in the still hot vacuum chamber by heating the filaments up until a temperature of 220°C is reached in the evaporator interior. This temperature is measured using an internal thermocouple attached directly below the crucible. After reaching the base pressure, the evaporators are brought to operation temperatures at a stabilized flux using a stepwise increase in heating power, starting at about 10 W. The flux thereby also is increased stepwise, until it reaches a value lying 30 to 40 percent above the targeted deposition flux. Here, it is held for about 30 minutes and then reduced to the flux intended for deposition. For combined deposition of two materials, this procedure is exercised simultaneously with two sources. The evaporators thus have been in operation and degassed for $4 - 6$ hours before the actual deposition process is started. The Ti-pump has been filled with LN_2 and freshly Ti-coated best during the degas period with highest flux and reduces the pressure to the lower 10^{-10} range at intermediate fluxes. In the case of controlled impurification of a Copper film with less than 1 percent of Cobalt atoms, we face the problem of large spans of flux currents that arise. If one does not want to go to very high deposition rates, there is the possibility of *pulsed* impurity deposition. This makes use of the electronic shutter control, which may be set to open several times for a short interval, at least once before each monolayer of the host metal is completed. This procedure ensures a film with well dispersed impurities inside and was used to prepare the dilute magnetic alloy films analyzed in Chapter 6.

Film growth experiments

The capabilities of the new preparation machine have been tested in a series of experiments using the room-temperature microscope for surface analysis. Mainly, the thin film deposition has been used to prepare metal films of some ML thickness on a semiconductor substrate at LN_2 temperature, followed by a warming-up to room temperature. This approach has been followed mainly with Cu overlayers, but also with Co. These experiments allowed a study of Cu/GaAs(110) but gave only a flashlight view on the Co system, an example of which is shown in Fig. 2.5. The structural characteristics and also the electronic properties of the thin Cu overlayers on GaAs(110) were studied and compared with recent results on such-prepared Ag films [27]. A more detailed description of this study can be found in ref. [28].

3.2   The scanning tunnelling microscopes

Parts of the experiments were performed using a UHV room-temperature(RT) STM, such as the preparatory deposition experiments and the investigations on surface diffusion. The electronic structure measurements on surface states and atomic defects as well as the atomic resolution images were acquired with a ^{4}He-cooled UHV low-temperature(LT) STM. Both microscopes have the doubly-inverse Besocke-type scanning unit in common. This is the design of choice for low-temperature application, since the sample and the scan piezos both are thermally well coupled to the cryostat. The movable helical ramp on top with the z-piezo reaching down to the sample surface is also thermally connected to the LHe tank by some very fine silver wires for a faster cool-down. Our instrument provides a comparably large coarse approach range of 1.5 mm facilitating cross-sectional work on cleaved-edge semiconductor samples. The microscope chambers are ion-getter-pumped with an additional Ti-pump, which ensures a base pressure in the upper 10^{-11} mbar range at room temperature. The internal vibrational damping of the microscopes is solved differently for both systems due to the special needs of cryogenic design. While the RT-STM is placed on a stack of four steel plates decoupled by small Viton rubber rolls as damping elements, the LT-STM sits at the bottom of an about 1m long viton-damped and spring-suspended vertical pendulum containing the liquid Helium tank. The construction of the LT system is shown in Fig. 3.9. Both systems allow *in situ* tip exchange, using an integrated magazine pick-up for sample and tip storage in UHV. The RT-STM is further described in [25], and for the LT-STM, more details are given in refs. [24] and [29]. Here, it should only be noted, that one filling of the 4.7 litre LHe cryostat lasts for a time period of about 20 hours and cools the microsope to a temperature below 8 K. The temperature is measured using a semiconductor diode placed near the sample holder pick-up, where values between 5.9 K and 7.5 K are commonly reached. The microscope design grants direct optical access to the tunnelling contact, so that the tip can be directed to certain regions of the sample by control with the eye from outside the chamber.

spring
suspension

electrical
feedthroughs

bellows with
Viton damping

additional
bellows

coaxial He in/outlet
& radiation shields

LN$_2$ tank

250 mm

LHe tank with
Cu baseplate

Cu STM housing

quarz
windows

tip & sample
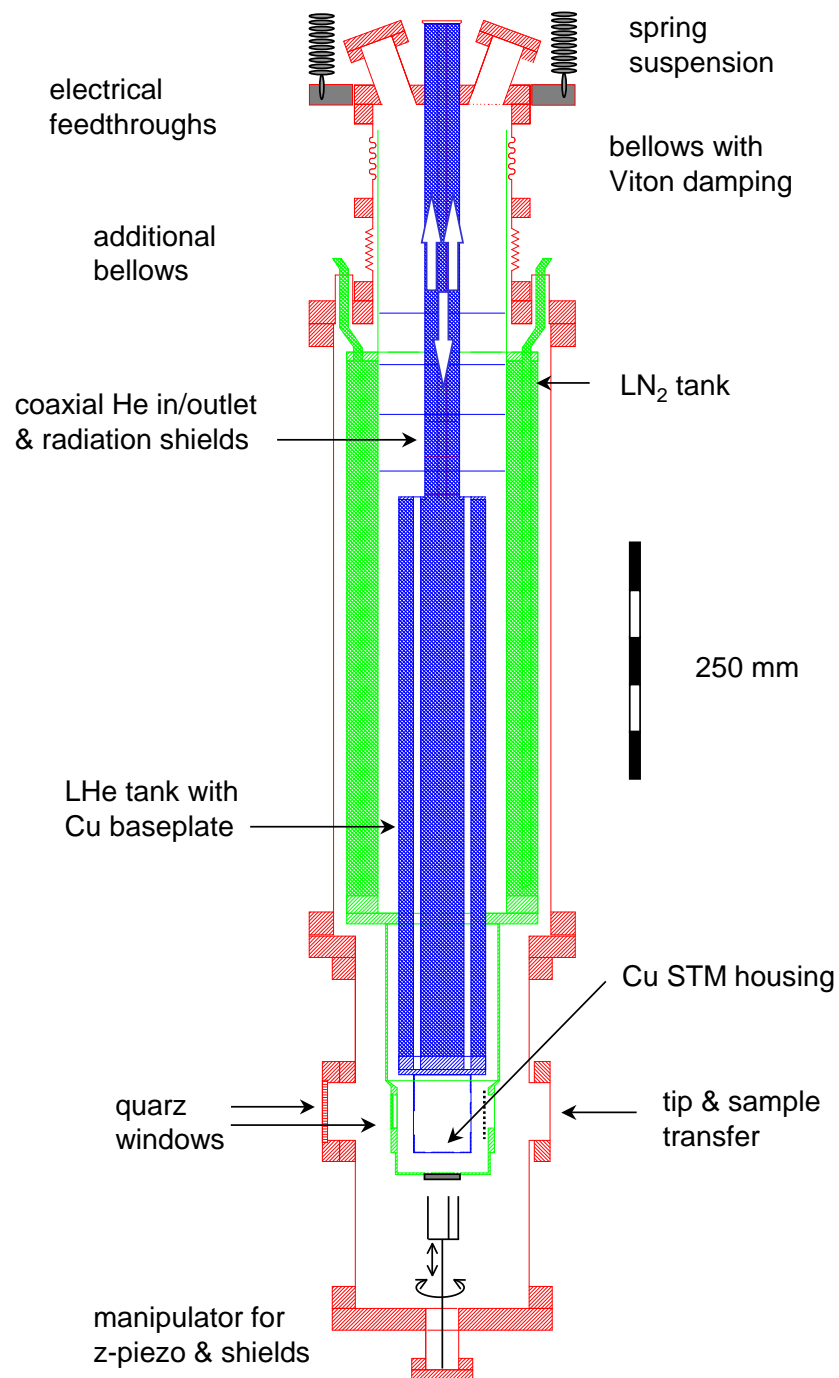transfer

manipulator for
z-piezo & shields

Figure 3.9: *Detailed view of the LT-STM chamber. Optical access for tip positioning is granted by shield openings that are radiation-screened by quartz windows and a Cu shutter that can be handled with the z-piezo manipulator.*

Chapter 4

Self-diffusion on Ag(111) at $T = 295$ K

A study of the temporal evolution of step and island structures on the Ag(111) surface at room temperature is presented in this chapter. An entropy-driven relaxation of a non-equilibrium step edge configuration was observed using time-resolved STM imaging documenting its structural change for ten hours. Using the Gibbs-Thomson relation, the relaxation process is quantitatively described as a diffusive mass transport in terms of a gradient in the chemical potential along the monatomic step edge. The STM data directly prove that mass transport on Ag(111) is dominated by step edge diffusion at 295 K, and allow a determination of the corresponding effective energy barrier [30]. We determine a value of $E_{eff} = 0.49 \pm 0.05$ eV and compare this with recent results on island diffusion studies.

4.1   Studying surface diffusion with the STM

Although STM is employed mostly under stationary conditions for the analysis of structural and electronic properties of surfaces, it is also a suitable method to observe dynamic processes. Since STM imaging inherently is a slow procedure, it is a requirement that the speed of the dynamic processes matches with the slow image acquisition rate. Thermally activated processes like surface diffusion can be slowed down by reducing the temperature. In a microscope operable down to liquid-Helium-temperatures, any diffusive process can be frozen out, which ultimately enables precise manipulation of individual adatoms with the STM tip [31, 32]. Adatoms are easily imaged as atomic scale bumps, when the residence time at a surface site is on the order of the recording time of the image. When the residence time is as short as the line scanning time, there will be timely correlations between successive lines and the image mixes temporal and structural information. In case

of even faster atomic motion, an adatom may jump in or out of the tunnelling contact while the tip is practically at rest over a specific surface location. This results in a sort of noisy imaging of regions with highly active surface diffusion.

The observation of surface diffusion of metal atoms with atomic resolution has been reported first in 1973, long before the STM had been developed [33]. Using Field-Ion-Microscopy, it has been possible to observe elementary jumps of single atoms of variable chemical identity on the crystal facets of a field emmission tip [34]. The diffusion of metal atoms on metal substrates is interesting because of the delocalized bonding character responsible for adatom binding. The elementary diffusion barriers are related to the bonding properties, which might be of a more polar character in the adsorbate case than in the bulk where they make up the metallic cohesion. Since the beginning of the 1990ies, the STM has contributed much information on surface diffusion for very different adsorbate-substrate systems. In the context of surface catalysis and reactions, the diffusion behaviour of molecules chemisorbed on metal surfaces are of fundamental interest and has been a field of intense research [35]. Self-diffusion observed by fluctuation of step and island structures at higher temperatures has been another topic studied in great detail [36]. Elementary diffusion steps of metal adatoms can be observed by STM directly only at low temperatures. Two recent studies analyzed ensembles of metal adatoms on noble metal surfaces at low temperatures (Cu atoms on Cu(111) [37], Co on Cu(111) and Co on Ag(111) [38]). Quasistatic (snapshot) images showed clear evidence for a long-range substrate-mediated interaction between the adsorbates at low coverages around 0.01 ML. Preferably, the adatoms reside in regions of low $LDOS$ of the electronic surface state. This demonstrates the importance of not only the lattice structure but also the electronic structure for surface diffusion at low temperatures. Around room temperature, single elementary steps cannot be resolved anymore due to the high, thermally activated hopping rates. However, the effects resulting from surface diffusion can as well be seen in the equilibrium shape or the temporal change of nanoscale surface structures such as steps or islands.

4.1.1   Energetics and structure

The energetics of elementary surface processes are not only of fundamental interest in chemical and solid state physics, they are of major importance for the growth and stability of self-assembling nanostructures. Due to its ability to locally probe individual surface structures, the Scanning Tunnelling Microscope (STM) has become a preferred tool within the interdisciplinary research field of nanostructure physics [39]. Growth studies have shown that quantitative information can be extracted from STM topography data with the help of kinetic analysis [40]. As well, thermodynamical relations assumed to be a good approximation down to the nanometer scale have been applied to describe the energetics and dynamics of surfaces [41]. The long-time stability of surface structures can be monitored by recording sequences of STM images that reveal the structure's development in time. Such observations generally allow conclusions on the energetics of surface
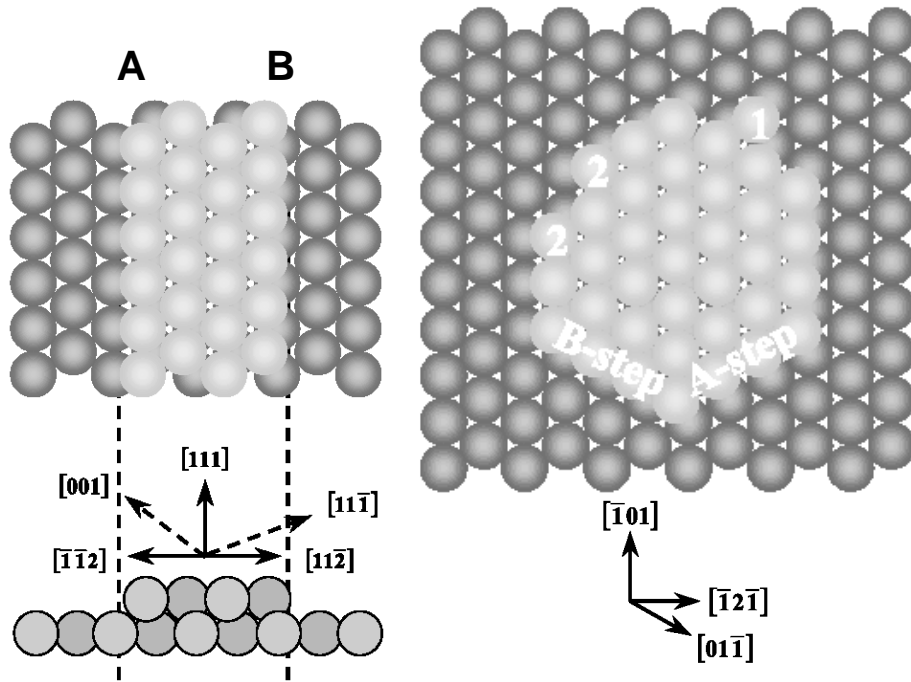
Figure 4.1: *Atomic structure of steps and monatomic islands on fcc(111) surfaces and the corresponding crystallographic orientations. The labels A and B denote the two structurally different types of steps. The numbers mark a step-adatom (1) and kink atoms (2) at the island boundary. Graphics reproduced from ref. [36].*

transport processes. Using this approach, the thermal stability of atomic scale defects on highly oriented noble metal surfaces has extensively been studied in the past [36]. On Cu(111) and Ag(111), substantial changes in surface morphology can be observed at room temperature on a time scale of minutes. Recent studies include thermal equilibrium fluctuations of monatomic surface steps on various Ag and Cu surfaces [42, 43, 44, 45], as well as ripening and relaxation processes of steps and island structures demonstrating the effect of local non-equilibrium on the nanometer scale [46, 47, 48, 49].

On single crystal surfaces, step and island structures constitute two-dimensional interfaces, if the vacuum interface is ignored for the moment. A monatomic step on a terrace thus separates a solid from a gaseous part of the crystal surface coexisting at temperature T. A closed-loop step encircling an island approaches an equilibrium shape by minimizing its interface energy. In two dimensions, this interface energy is called *step line tension* γ. The noble metals Cu, Ag and Au condense in the face-centered-cubic (fcc) structure. This lattice type corresponds to a close-packed volume structure for a hard-sphere model. On the (111)-oriented surfaces of Ag and Cu, islands have an almost regular hexagonal shape with rounded corners at equilibrium around room temperature [50]. However, the fcc-structure of the noble metals only has threefold symmetry [51]. This results in two

different types of monatomic steps being present on these surfaces. Fig. 4.1 illustrates the geometry of A- and B-type steps and the convention of nomenclature. While the A-step forms a (001)-microfacet, the B-step facet has a (111)-orientation. This can also be seen directly from the shape of the first brillouin zone of the fcc-lattice (see Fig. 5.1). A hexagonal, symmetric island shape is the result of nearly identical interface energies at all of the six boundary step segments, and therefore of just equal line tensions of A- and B-type steps. In contrast to Ag and Cu, a length ratio of 1.5 is observed On Pt(111) for vacancy islands, corresponding to a step line tension quotient $\gamma_A/\gamma_B = 1.15$ [52]. Theory also expects that different diffusion energies exist along the two step types. For Ag(111), values of 0.22 and 0.30 eV have been calculated for A- and B-type steps, respectively, [53], supported by computer simulations and experimental results [54]. Yet, direct experimental data on diffusion along step edges is very rare. The advantage of STM is that observations are made at individual structures using time-lapsed images, so that, in principle, conclusions on the specific diffusion path can be drawn.

4.2   Theory of surface diffusion

In a microscopic picture, a rigorous theory describing diffusion leads to a many-particle problem. This makes a simple description impossible. With certain assumptions, however, a simplified theory is applicable describing the isolated particle on a surface potential landscape. This assumes a local model, accounting for nearest-neighbour interactions, where the binding energy at an adsorption site is determined by the number of its number of nearest-neighbour bonds (Solid-On-Solid model). A surface atom that hops to a neighbouring site has to surmount a local diffusion energy barrier that depends on the binding energy of the two sites. The sum of (a positive) energy difference and the diffusion barrier constitutes the energy necessary for an elementary hopping event. These assumptions are summarized in Fig. 4.2 showing a 1D sketch of the potential for an adatom near a step site. An adatom in a minimum can overcome the barrier to a neighboring site by receiving the hopping energy from the phonon bath of the substrate. After jumping, it is thought to relax immediately and lose its excess energy to the substrate again, remaining in the new place until another *independent* jump occurs.

4.2.1   The low-density limit

The theoretical framework summarized in the following is based on the presentation of Gomer [55] and describes surface diffusion in global equilibrium, referring to a single particle picture established by Einstein [56]. A simple interpretation of experimental data is possible, if interaction between diffusing particles can be neglected. In one dimension, a single atom performs a random walk with a jump frequency ν_{eff} and achieves an average displacement of

$$\langle (\Delta r)^2 \rangle = a^2 \nu_{eff} \, t \equiv 2D^* t \tag{4.1}$$
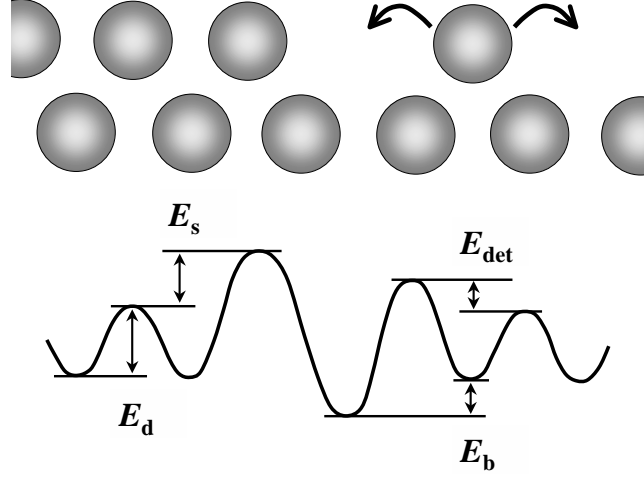
Figure 4.2: *A microscopic model for single atom surface diffusion. The energy barrier for a single hopping event is determined by the local bonding configuration. Assuming diffusion along a step, E_d corresponds to hopping to an equivalent neighbour site. Detachment from a kink needs the activation energy $E_{kl} = E_d + E_b$ while diffusion of a kink atom to the upper segment is most costly with a barrier $E_{ku} = E_d + E_b + E_s$. An additional de-/attachment barrier as shown with E_{det} is not present on Ag(111).*

within a time t, if the single step length is a. The *tracer* diffusion constant D^* is defined as a proportionality factor between the average displacement and time. If ν_{eff} is taken to be thermally activated, the diffusion constant is

$$D^* = \frac{1}{2}a^2\nu_0 exp\left(\frac{-E_d}{k_B T}\right) \tag{4.2}$$

Apart from this microscopic definition of a diffusion constant D^*, deduced merely from kinetics, the *chemical* diffusion constant D which appears in the diffusion equation (Fick's second law)

$$\frac{\partial \rho}{\partial t} = \vec{\nabla}_r \cdot D\vec{\nabla}_r \rho \tag{4.3}$$

is defined in terms of a concentration gradient, explicitly referring to a non-equilibrium state of the system. Here, the continuity equation was applied to the particle current density $J = -D\nabla_r\rho$ (Fick's first law). A more general formulation of J can be given by using the local chemical potential μ, which often is more easily evaluated from experiment:

$$J = -B\vec{\nabla}_r\mu \tag{4.4}$$

Here, B is the corresponding transport coefficient. If the chemical potential gradient is *only* due to a change in particle density, the coefficient B is related to the chemical diffusion

coefficient D via the Einstein relation for the mobility $M = \frac{D}{k_B T}$ by

$$B = D\frac{\rho}{k_B T} \left(\frac{\partial(\mu/k_B T)}{\partial\, ln\rho} \right)^{-1} \tag{4.5}$$

The diffusion constant D is divided here by a *thermodynamic factor* $(\partial(\mu/k_B T)/(\partial\, ln\rho)$ accounting for the interaction between the diffusing particles. Even if nearest-neighbour interactions are assumed to be zero, there will be still a site exclusion at finite particle density ρ due to already occupied sites in the vicinity. According to Reed and Ehrlich, this correction can be included in the jump rate, which becomes density-dependent with $\nu(\rho) = \nu_{eff} \cdot (1 - \rho)$ [57]. The thermodynamic factor is then restricted to explicit particle interactions, and the diffusion coefficient is expressed as

$$D = \frac{1}{2}\nu(\rho)\ a^2 \left(\frac{\partial(\mu/k_B T)}{\partial\, ln\rho} \right) \tag{4.6}$$

This equality assumes the validity of Darken's equation [55, 58, 59], which states that D/D^* is equal to the thermodynamic factor. Then, the quotient of D and $(\partial(\mu/k_B T)/(\partial\, ln\rho)$ in Eq. 4.5 is identical to the tracer diffusion constant D^*. In reality, this can only be assumed under ideal conditions, when the particles are able to move completely independent of each other. More specific, no cross-correlations should exist between the velocities of different particles [55]. This of course is very difficult to grant in the case of 1D-systems, more than in the 2D or 3D case. In general, this condition is approximately fulfilled at very low surface particle densities ρ of an overlayer. For the experimental observations that are presented in the following, this will be assumed to hold (see Appendix B).

4.2.2 Driving forces – the Gibbs-Thomson relation

When it was talked about island 'equilibrium' shapes in the preceeding section, this is only appropriate with respect to a certain time scale. An island at a surface-vacuum interface will slowly decay and finally disappear due to evaporation or slow detachment of atoms onto the surrounding terrace [46, 60]. Therefore, an island actually is a local non-equilibrium structure existing within a state of global equilibrium. The driving force for its decay is the elevated local chemical potential μ at the boundary of the island. A curved surface step encircling an island is distinct from a perfectly straight step of similar dimensions, since on average, it has a larger number of low coordinated sites due to its shape. In a continuum picture, this geometric property is reflected in the dependence of the chemical potential μ on the local curvature of the boundary space curve expressed by d^2x/dy^2 [41, 36]. The chemical potential is defined as the thermodynamic coefficient of the particle number N measuring the free energy δF per δN particles. In terms of the island boundary space curve, the free energy is given by (see Fig. 4.3)

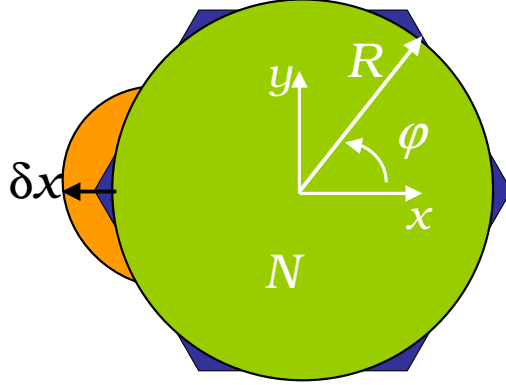$$\delta F = \frac{1}{a_{||}a_\perp} \int (\delta x\ \mu)dy \tag{4.7}$$

Figure 4.3: *Sketch of a hexagonal island approximated by a circular shape. The angle φ defines lateral directions relative to high symmetry orientations of the crystal. The calculation of the island free energy in terms of the boundary space curve is illustrated.*

In the limit of small curvatures, the local chemical potential is then given by the approximate relation [36]

$$\mu = \mu_0 + a_{||}a_\perp \frac{d^2 x}{dy^2}\left(\gamma + \frac{\partial \gamma}{\partial \varphi^2}\right). \tag{4.8}$$

The expression in brackets denotes the *step stiffness*, with the angle φ defined as is shown in Fig. 4.3. If the island is modelled by a circular boundary with identical area, the curvature is given by the inverse of the radius R. On the other hand, the line stiffness is well approximated by the line tension γ, when highly oriented crystal directions dominate the island shape. In this simplified case, the chemical potential of the island boundary differs from that of a straight step by

$$\Delta \mu = a_{||}a_\perp \frac{\gamma}{R}. \tag{4.9}$$

This is the Gibbs-Thomson relation which will be used for the analysis of diffusive transport in the following section.

4.3 Experimental results

In this section, STM data is presented which provide a clear experimental proof that step edge diffusion is the most efficient mass transport process on the Ag(111) surface at room temperature. This is directly observed in the relaxation of a non-equilibrium surface morphology. We recorded an image sequence showing step edge diffusion where source, diffusion path and sink are clearly defined, spatially separated and stable on a time scale of hours. Furthermore, the gradient in the local chemical potential that drives the diffusive
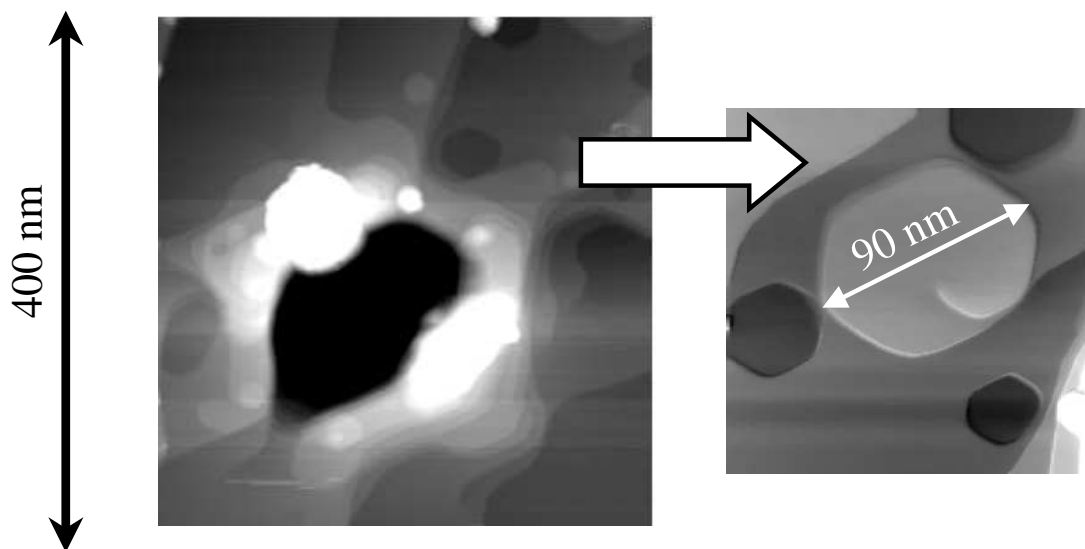
Figure 4.4: *Indentation on the Ag(111) surface with the tunnelling tip. Defects created by this procedure, as shown on the right side, can have unusual geometries that are not achieved by remote treatment like ion bombardement.*

mass transport is well defined, and can be evaluated by the Gibbs-Thomson relation. From the absolute amount of mass transported within a time Δt, the effective transport coefficient B_{eff} is obtained, and a value for the corresponding activation barrier for step edge diffusion on Ag(111) is extracted. The result is compared with those of published temperature dependent studies and theoretical calculations. Finally, the implications for the mechanisms of island diffusion are discussed, which recently was studied in detail on Cu(111) and Ag(111) [61].

4.3.1 Preparation and measurement

The measurements were performed using the room temperature UHV-STM operating at a base pressure better than $1 \cdot 10^{-10}$ mbar. The Ag(111) single crystal was prepared in UHV by sputtering with 700 eV Ar^+ ions and subsequent annealing steps between 670 and 850 K. Tips were electrochemically etched from tungsten wire, sputtered with 4 kV Ar^+ ions and characterized by field emission. After transfer to the STM, a non-equilibrium condition on the surface was created by indenting the clean sample with the tip. This locally produces a morphology of stacked terraces, adatom and vacancy islands as well as a number of screw dislocations in the vicinity, as is shown in Fig. 4.4. The local non-equilibrium created by the indent then relaxes and gives rise to rearrangement of surface structures. The dynamics was captured by continuous imaging of a specific area. The tunnelling parameters were chosen to be non-invasive with respect to surface diffusion using low bias $V_B = 0.05$ V and $I_T = 0.2$ nA, corresponding to 250 MΩ tunnelling

resistance [36]. Spatial resolution was 0.8 nm^2 per pixel. A few impurity defects that occasionally were found on the surface proved to be immobile and provide reference points for kinetic analysis. Their presence in an image sequence enables us to monitor piezo drift and allows the determination of absolute positions for steps and islands, even when adjacent structures are in relative motion.

4.3.2 Observing diffusion at dislocations

In this paragraph it is demonstrated how diffusion is seen in the tunnelling microscope at RT. Specifically, the appearance of dislocations and their properties regarding surface diffusion are briefly discussed. Dislocations are not very well studied by STM, since the largest part of this defect is buried in the subsurface region and therefore is not accessible by tunnelling microscopy [62, 63]. For a dislocation intersecting with the surface, two cases can be distinguished. In the case that the Burger's vector is parallel to the surface normal, its appearance in a constant-current image is that of a step ending on a terrace under a local screw-like distortion of the surface layer. The second case, where surface normal and
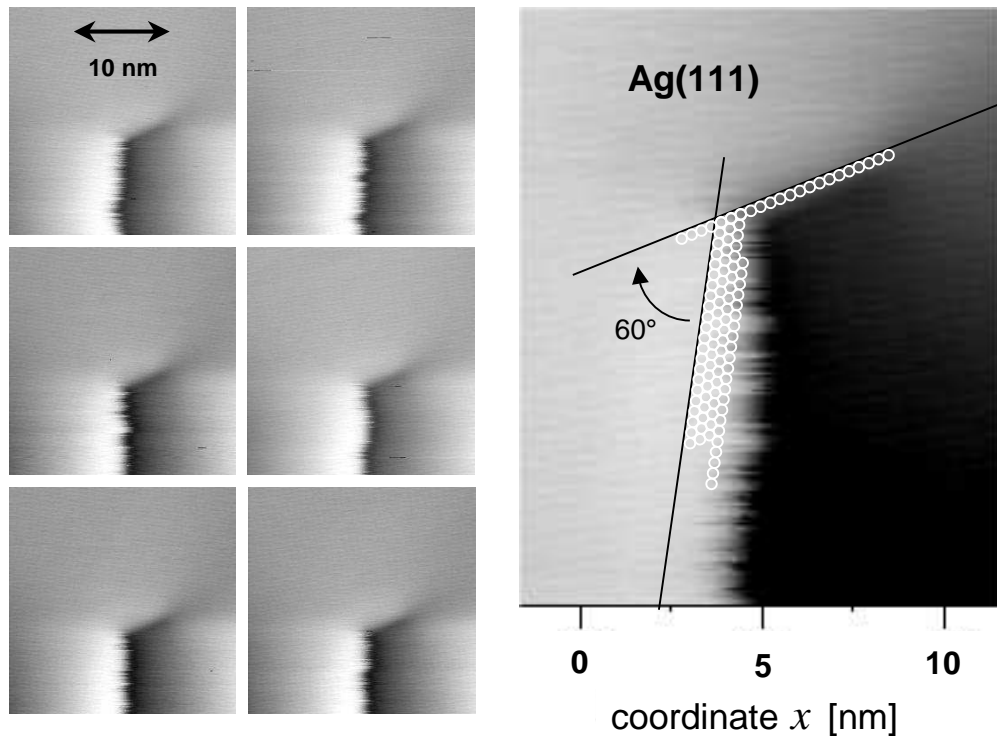

Figure 4.5: *Sequence of step fluctuations near a dislocation core. The dislocation is a highly effective barrier for atoms diffusing along the step edge. $U_B = 0.05$ V and $I_T = 0.2$ nA. Little residual drift shifts the images slightly upwards over the time.*

Burger's vector are orthogonal, shall not be considered here. A series of images showing a dislocation of the first type (taken periodically every 171 seconds) is presented on the left side of Fig. 4.5. The step created by the dislocation is imaged with a frizzy quality, which is the result of fluctuating kinks due to fast diffusion processes at the step while it is scanned. It is clearly seen from this sequence that the shape of the step fluctuates from image to image. Interestingly, the step forms a corner at an angle of 60 degrees before vanishing at the dislocation core. The last portion of the step behind the corner is completely straight and shows no frizzyness at all. This lack of kinks and fluctuations and its temporal stability indicates that step edge diffusion is strongly inhibited beyond the corner point. It is obviously the strain building up in this region that is responsible for a significant change in the local diffusion barriers. Additionally, the atomic structure of the surface has been graphically overlaid on the right side of Fig. 4.5, in order to give an idea about the extent of the step fluctuations. The variation in the average step position is about three atomic diameters. In the following, the strain-induced annihilation of two oppositely strained dislocations will be seen to open up an effective diffusion channel by connecting two initially separate surface steps.

4.3.3   Entropy-driven step edge diffusion

Fluctuations of step patterns on vicinal metal surfaces have revealed that the predominant mass transport mechanism is temperature-dependent. For both Ag(111) and Cu(111), it was concluded that diffusion along step edges dominates at room temperature (RT) [36]. However, contradictory notion of the dominant process had been evoked by an analysis of the random walk behaviour of vacancy islands on Ag(111) at RT [64]. This conclusion relied on a simple interpretation of an inverse power law for the scaling of the diffusion coefficient of island structures with their size. Later it has been argued that the scaling exponent cannot be interpreted in a simple way [65], but the origin of this failure still is subject to discussions. Meanwhile, it is agreed that the step and island boundary fluctuations at RT should arise from step edge diffusion [61], but an unmistakable experimental observation has not been made up to now.

Eight snapshots of the relaxation dynamics analyzed below are shown in Fig. 4.6. The unusual topology is a result of the tip indent that had been produced nearby. The white spot on the lower left of most frames marks an immobile surface defect. The initial situation from which the relaxation develops has been shown on the right hand side of Fig. 4.4, and in 4.6 a) the relaxation has set in. The boundary of a large adatom island, monatomic in height and approximately 90 nm in diameter, is crossed by a surface step which emerges from a dislocation in the centre of the island. That leads to a quick rearrangement of the island boundary to an open, hexagonal spiral structure seen in b). We will call this object the *adatom spiral* in the following. The area comprised by the purely hexagonal part of the spiral will be referred to as the *hexagon*. The outer end of the adatom spiral in the upper right of the image is terminated by a second dislocation. The
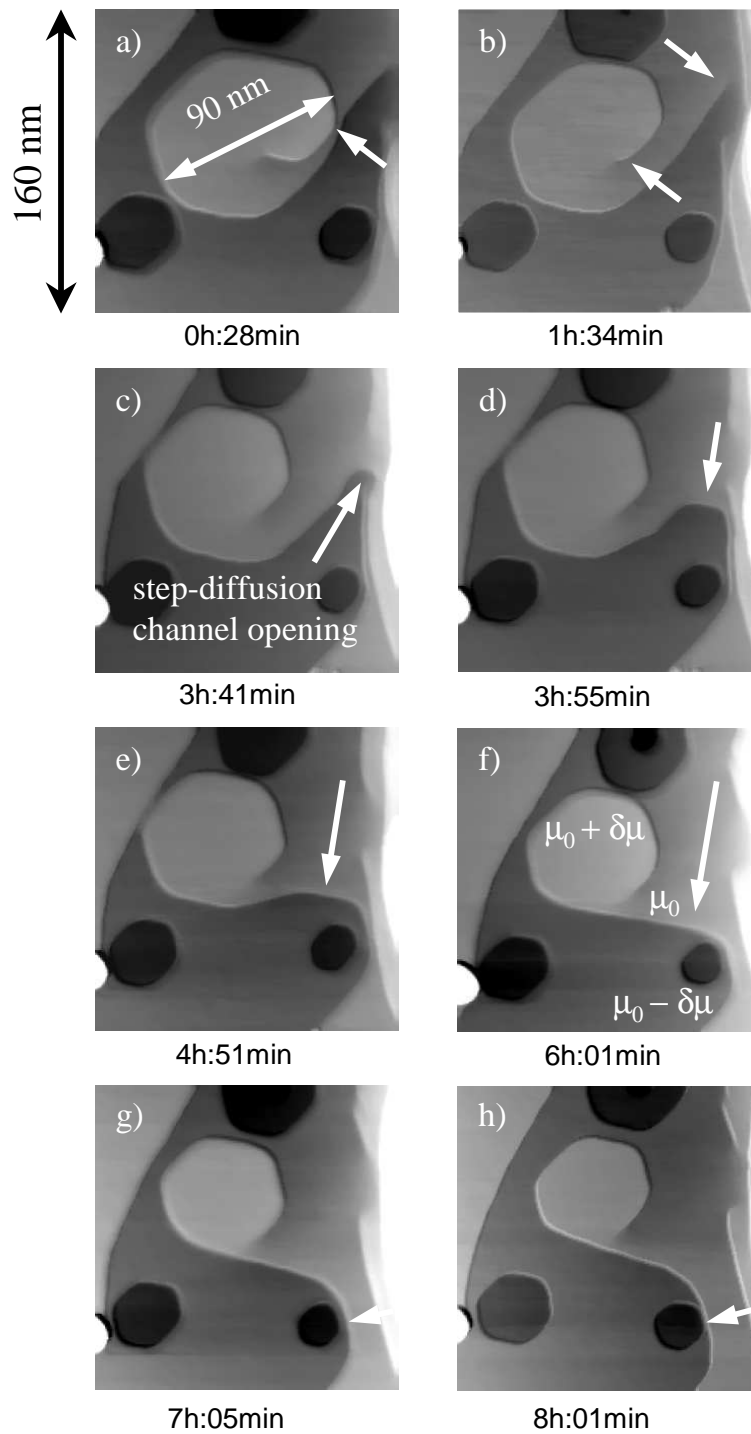
Figure 4.6: *Time evolution of surface structures created by a tip indent on Ag(111). Caused by a step crossing, a large island first relaxes to a spiral step. After attachment to a second surface step by recombination of two neighbouring dislocations between image b) and c), it finally decays by diffusive transport of atoms along the step edge.*

important property of these dislocations is that they inhibit step edge diffusion beyond, so that no quick net mass flux away from or into this structure can occur. As a decay channel, only slow 2-D evaporation of atoms from step sites onto the surrounding terrace is possible [46]. At this stage, we thus observe only rearrangement of the spiral step towards an equilibrium shape and no obvious reduction in its overall size. In c), the second dislocation terminating the spiral to its outer end has just vanished by annihilation with a third dislocation located nearby. This event substantially changes the situation, since the adatom spiral now connects to a surface step with opposite curvature. According to the Gibbs-Thomson relation, the convex adatom spiral represents a high-μ region, while the concavely bent step segments extending to the right constitute a low-μ part. Note that diffusion in this case is possible only in one direction, since at its inner end, the adatom spiral still is terminated by a dislocation.

In analogy to the standard thought experiment in entropy, the dislocation annihilation corresponds to the removal of a constraining barrier, and an entropy-driven flux to the low-density side sets in. Accordingly, a net mass flow along the step is observed, which aims to equilibrate the difference in chemical potential between the two step sections. At first, a quick filling of the highly concave section is seen in d) and e), indicated by the arrows. A long straight step segment has finally developed in f), due to continuous accumulation of atoms in regions of negative curvature. Since a straight step represents its equilibrium state, the next concave step section is now filled, as seen in g) and h), indicated by the arrows. The straightening of the step thus proceeds via successive local growth in the concave parts which is fed by the hexagon serving as a remote source of step-adatoms. These observations clearly show that the quick relaxation process is due to atoms diffusing along the step edge. A different mechanism such as detachment of step atoms and diffusion across the terrace obviously cannot account for such localized growth at distant parts of the same step. It would rather lead to atom attachment and local growth at the adjacent step edge located to the upper left of the adatom spiral, which is seen to be very limited.

In the following, the observed diffusion process will be analysed quantitatively. Since the special arrangement of the step provides a favourable geometry for using the Gibbs-Thomson relation, a determination of an effective energy barrier for step edge transport is possible due to the local non-equilibrium. As was also pointed out by Giesen *et al.* [48], no difference in the nature of the underlying elementary diffusion processes is expected between equilibrium and non-equilibrium configurations in the limit of low particle density. As a simple model to describe the observation, the two oppositely curved sections of the step are treated as atomic reservoirs with differing chemical potentials. These are connected by a one-dimensional diffusion channel represented by the straight step edge segment in between. Then, the assumption is made that the chemical potentials $\Delta\mu_1$, $\Delta\mu_2$ of the reservoirs are given by the Gibbs-Thomson relation for a spherical structure. This geometrical approximation also determines the length of the corresponding step segment Δs, as is illustrated in Fig. 4.7. A measure for the particle flux along Δs is given by the decay rate of the adatom spiral. The development of the hexagon area $A_H(t)$ over time is
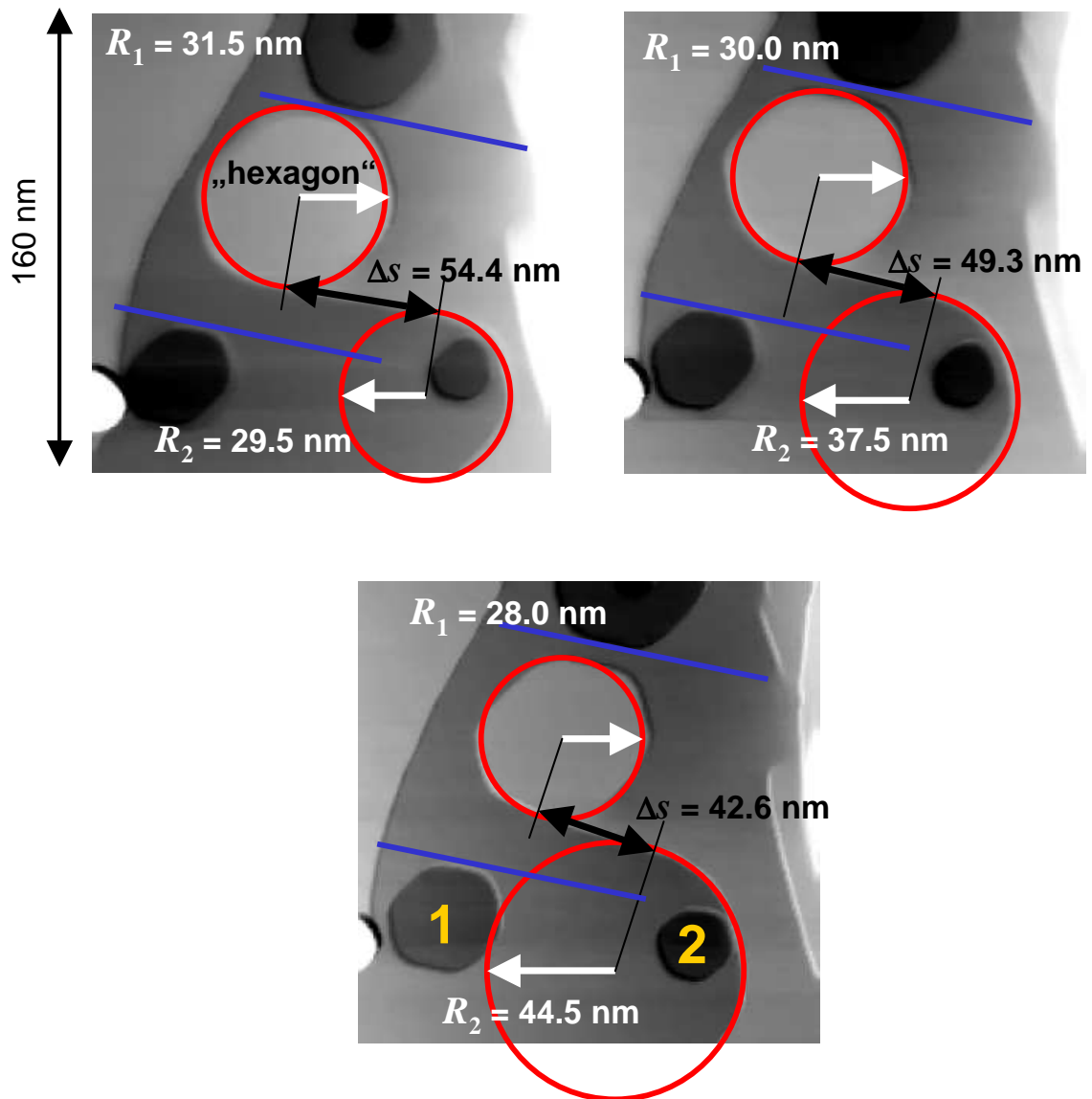
Figure 4.7: *Geometrical construction to parametrize the observations and determine the local chemical potential along the step edge. To quantify the transport coefficient, the radii equivalent to the local step curvature and the corresponding transport lengths Δs are extracted from experiment as shown. The two additional lines indicate the low-indexed crystal orientation along the Δs-direction. Two vacancy islands, the decay of which is also analyzed in Fig. 4.8, are numbered with 1 and 2.*

plotted in Fig. 4.8, together with those of two neighbouring vacancy islands *1* and *2*, for comparison. The slope of the $A_{1,2}(t)$ curves of the slowly decaying vacancy islands is in very good agreement with values reported earlier for the Ag(111) surface [66]. The fast part of the hexagon decay curve on the right quantifies the number of atoms transported along the step edge per time interval and shows an approximately linear decay for all times later than $t = 4{:}00$ h. This circumstance allows to pick such geometries out of the sequence which are most suitable for interpreting the energetics. From the $A_H(t)$ curve, we can directly evaluate the diffusion flux j along Δs to be 1.6 atoms/s. Although a linear decay curve should generally indicate a detachment-limited process, the island size is much too large for a reliable assignment based on experiment. In the present case, it can rather be assumed that the decay proceeds in the diffusion-limited regime, since the diffusive process for a step-adatom to either leave the hexagon or to move along the step segment Δs is not of a different quality.

For a regular and compact island, the difference in chemical potential for the curved step edge compared to that of a perfectly straight step is given by Eq. 4.9 in terms of the step line tension γ, the average island radius R and the area corresponding to one surface atom. With the help of experimentally known values for $a_\perp = 2.35$ Å, $a_\parallel = 2.89$ Å[67] and $\gamma = 0.25 \pm 0.03$ eV/ $a_\parallel$ gained from island equilibrium shape analysis [50], the local chemical potentials $\Delta\mu_1$ and $\Delta\mu_2$ for subsequent images are obtained from the average
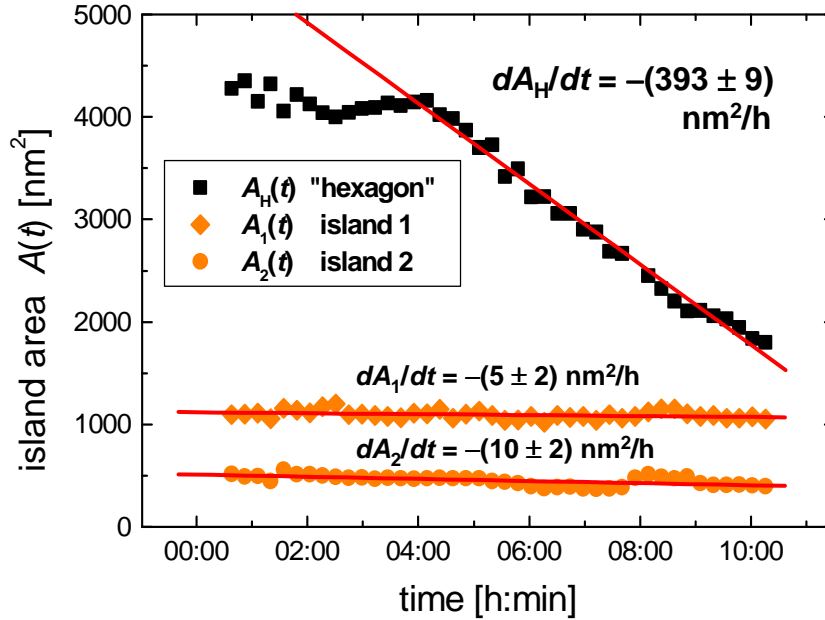

Figure 4.8: *Development of the island areas $A(t)$ of the hexagon and that of two vacancy islands denoted 1 and 2 (see Fig. 4.7). Around $t = 4$ h, a quick reduction of the hexagon's area sets in, which is due to the diffusive transport of atoms along the step edge.*

Table 4.1: *Local chemical potentials, resulting transport coefficients and effective activation energies for step edge diffusion determined at different times t.*

t [h:m]	$\Delta\mu_1$ [meV]	$\Delta\mu_2$ [meV]	Δs [nm]	B_{eff} 10^{-5}[eV·m/s]	E_{eff} [eV]
$6:01$	1.9 ± 0.3	-2.0 ± 0.3	54.4 ± 1.0	2.2 ± 0.3	0.49 ± 0.05
$7:05$	2.0 ± 0.3	-1.6 ± 0.2	49.3 ± 1.0	2.2 ± 0.3	0.49 ± 0.05
$8:01$	2.1 ± 0.4	-1.3 ± 0.2	42.6 ± 1.0	2.0 ± 0.3	0.49 ± 0.05

radii R_1 and R_2 measured in the STM topographies as shown in Fig. 4.7. The values in three cases are listed in Tab. 4.1. The overall difference in chemical potential from convex to concave part is thus $\Delta\mu_2 - \Delta\mu_1$, where it is assumed to drop off under steady state conditions over the distance Δs. The resulting diffusion current j is then given by the generalized transport equation

$$j = -B_{eff}\frac{\Delta\mu_2 - \Delta\mu_1}{\Delta s} \tag{4.10}$$

It defines the effective transport coefficient B_{eff} for diffusive mass transport along step edges. According to diffusion theory in the limit of low particle density, the coefficient can be expressed as in Eq. 4.5. In the case of a step, this seems to be a crude simplification, since in reality interaction will play a role due to the one-dimensional geometry. However, a comparison of event probabilities using calculated elementary energies on Ag(111) [61] shows that the low-density condition is justified even in the case of step edge diffusion at room temperature (see Appendix B). In this picture, the density ρ is equal to the step-adatom density at temperature T, which can be accounted for by a Boltzmann-factor containing the free energy E_ρ for step-adatoms in the enumerator of Eq. 4.5. The rest in the enumerator is the intrinsic diffusion constant D^* corresponding to the random walk of a single atom moving in one dimension along the step edge, so that

$$B_{eff} = \frac{1}{2}a_{\parallel}^2\nu_0\frac{exp(-E_\rho/k_BT) \cdot exp(-E_d/k_BT)]}{k_BT} \tag{4.11}$$

The sum of the energies E_ρ and E_d is the effective activation energy E_{eff} corresponding to the transport coefficient B_{eff}. In this definition, E_d is supposed to be the energy barrier for a single elementary process responsible for diffusive hopping. In the case of step-edge diffusion at RT, we do not have this simple case, and E_d would rather stand for an average activation energy for diffusion at a thermally rough, i.e. with $exp(\epsilon_k/k_BT)$ kinked step edge. We will use these relations to determine the effective activation energy E_{eff} from our experimental data, while we come back to E_d in the above expression only for comparing with calculated elementary energies.

Using the transport rate extracted from the $A_H(t)$ curve of the hexagon in Eq. 4.10, the effective transport coefficient B_{eff} along step edges at room temperature can be determined. With a reasonable estimate of the exponential prefactor, we can also calculate

an effective energy barrier E_{eff} for step edge transport. Giesen *et al.* extracted a trial frequency of $\nu_0 = 3 \cdot 10^{11 \pm 1}$ s^{-1} for step fluctuations on a non-vicinal Ag(111) surface [36], while $\nu_0 = 1 \cdot 10^{12 \pm 0.6}$ s^{-1} was found by Morgenstern *et al.* for step edge detachment in decay studies of isolated islands [68]. Here, the latter value of $\nu_0 = 1 \cdot 10^{12}$ s^{-1} will be used for the evaluation of the transport barrier, which is covered by both of the uncertainties and corresponds to typical vibrational frequencies expected for surface atoms. Thus, an effective energy barrier $E_{eff} = 0.49 \pm 0.05$ eV is found for atom transport along a highly oriented surface step edge on Ag(111).

The error of the transport coefficient B_{eff} due to the accuracy limit of the geometrical approximation of the step shape is only $1 \cdot 10^{-6}$ m/s·eV. The additional experimental uncertainty contained in the step line tension γ then leads to the values given in Tab. 4.1. Therefore, it is possible that the relative decrease of B_{eff} at $t = 8{:}01$ h is real, which could be attributed to a factor of three larger kink density due to the deviation of Δs from the ideal, highly oriented crystal direction indicated in Fig. 4.7. However, the table also shows that such changes in geometry have no significant influence on the effective energy barrier.

4.3.4   Discussion

We cannot say from the present experiments whether an A-type or a B-type step has been investigated, unfortunately. Depending on the step type, different diffusion barriers are expected theoretically. Yet, we can compare our number with step transport barriers found in the literature. In the case of copper, Giesen *et al.* determined an effective step diffusion energy $E_{eff} = 0.62 \pm 0.06$ eV by analyzing equilibrium step fluctuations on vicinal Cu(111) [48]. Our value measured on Ag(111) is smaller, which also is consistent with trends in the kink energies found on these surfaces [50]. Making use of a simple broken-bond model, and assuming that kink sites are the only source of step-adatoms, their creation is determined by $E_\rho = E_b = 2\epsilon_k$. This is justified as long as a "break-up event", where atoms hop out of a straight section of the step, is far more unlikely to contribute to the step-adatom density. Inserting $\epsilon_k = 0.101$ eV measured for island boundaries on Ag(111) [50, 69], we obtain from our experiment an average activation energy of $E_d = 0.29 \pm 0.05$ eV. For comparison, Stoltze and coworkers calculated E_d for perfectly straight steps without kinks on Ag(111) using effective medium theory (EMT) and predicted values of $E_d = 0.22$ eV (A-step) and $E_d = 0.30$ eV (B-step) [53, 54].

Independent from these estimates made for comparison with theory, it is instructive to discuss our value for E_{eff} together with the result of another experimental study on Ag(111). Following a different approach, Schlößer *et al.* investigated the Brownian motion of vacancy islands in a temperature-dependent study on Ag(111) to determine island diffusion coefficients as a function of size. They found that the effective activation barrier for island diffusion is independent of island size. Linear fits to size-selected Arrhenius-plots yielded values of $E_{eff} = 0.51 \pm 0.04$ eV and $E_{eff} = 0.53 \pm 0.05$ eV for vacancy and adatom

islands, respectively [61]. This result agrees well with the barrier we find for step edge transport in our entropy-driven transport experiment.

This agreement suggests a further conclusion regarding island diffusion. A general exponential scaling law of the form

$$D_{isl} \propto exp(-\frac{E_{eff}}{k_B T}) \cdot R_{isl}^{-\beta} \tag{4.12}$$

should describe the island diffusion coefficient D_{isl} as a function of the average island radius R_{isl} [70]. According to an analysis based on continuum theory as well as basic dimensional considerations, the exponent β is expected to indicate the dominant mass transport process. The values 2 and 3 are predicted in case of terrace or step edge diffusion, respectively [44, 71]. The interpretation of exponents extracted from experimental data however, has turned out not to be straightforward. The exponential relation was confirmed by experiment, but integer values for β are almost never met and systematically found too low [72, 61]. Simulations of island diffusion which considered step edge transport to be dominant have shown that such behavoiur can be reproduced by model calculations [70, 73]. Its origin thus lies in the microscopic details of diffusive mass transport along step edges. The present experimental observation together with the result of the energetic analysis does strongly support this view, and it shows that other channels have only negligible effects around RT. In fact, the activation barrier for step edge detachment as measured by Morgenstern *et al.* is very high with $E_{det} = 0.71$ eV and will hardly be effective at 300 K [68].

Furthermore, it is interesting to note that geometry and size of the system under investigation appearantly has no significant influence on E_{eff}. The results on islands studied in [61] (radius R_{isl} between 2 and 10 nm) and the step edge transport (length Δs about 50 nm) investigated in our experiment suggest that effective diffusive transport is not influenced much by finite size effects or geometrical shape. Such effects could be responsible for a dependence of D_{isl} on R_{isl}. It has been proposed that island diffusion is controlled by core breakup events, which occur at corner sites of small compact island structures [74, 73]. The energy barrier for this process is dominating the effective activation energy for island diffusion in these calculations. In case of an elongated step, no corner sites are present, but the corresponding process is diffusion around kink sites [70], which is crucial for a net transport of atoms as seen in our experiment. Comparison with theoretical elementary energies calculated using EMT-theory supports that this is the rate-limiting process for step edge diffusive transport. With a barrier of $E_{ku} = 0.49$ eV, kink-upward diffusion is the slowest process in step edge transport [61, 53], and its activation energy does fit perfectly with our experimental value for E_{eff}. We finally note that the identification of E_{eff} with a single diffusion process is also compatible with Eq. 4.10, since hopping of a kink-site atom to the upper step segment both is a diffusion and an adatom creation event, thus corresponding to $E_\rho + E_d$. This process can proceed independently at every kink site, and is not dependent on the step-adatom density ρ. That also explains our observation that the change in step orientation hardly affects the transport coefficient. At least in

the case of larger islands, it is plausible to expect that this diffusion process becomes the decisive one and determines the temperature dependence of D_{isl}.

4.4   Conclusion

Using time-resolved STM we have observed the relaxation of an island caused by a unique crossing-step geometry prepared on Ag(111). We could directly identify step edge diffusion as the most efficient mass transport channel at room temperature. The Gibbs-Thomson relation was used to evaluate the corresponding transport coefficient, which enables us to determine the effective activation energy for step edge diffusion. We find $E_{eff} = 0.49 \pm 0.05$ eV, which within the error limits is identical with barriers reported for island diffusion. This confirms experimentally that the mechanisms of step edge diffusion are governing the fluctuations of island boundaries at room temperature, and proposes that kink upward hopping is the rate-limiting elementary process. Reversely, the result shows that the Gibbs-Thomson relation, as it was used here, in fact provides a good measure of the local chemical potential of a curved step segment on the nanometer scale.

Chapter 5

Surface states on Ag(111) and Cu(111) at $T < 8$ K

Using Scanning Tunnelling Spectroscopy (STS) at $T < 8$ K, the *LDOS* of the L-gap surface states on Ag(111) and Cu(111) have been spatially resolved under the condition of lateral confinement in hexagonal island structures. Of each case, an individual analysis is made, and the results are briefly discussed in conjunction with previously published studies. In perfect agreement with calculations, a *complete* sequence starting from the lowest confined single-particle state could be resolved on an Ag(111) island. The chapter starts with summarizing the electronic properties of the noble metals and their close-packed surfaces, which are central to the present experiments.

5.1 Bulk properties and band structure

Although the noble metals do not belong to the simple metallic elements, their electronic structure is simple enough that they can be considered as prototype systems for a metallically bonded crystal. In the atomic configuration, they are characterized by a completely filled *d*-level subshell and one single *s*-type valence electron. In the solid state, the *s*-electrons are strongly delocalized to form an *sp*-derived band. Close to the Fermi-level, the electronic properties are found to be in very good agreement with that of a free-electron model [76]. However, the special properties of the noble metals, their clear bright colours, go back to the existence of the typical *d*-bands. The red colour of copper results from interband transitions between the filled states of the *d*-band and the empty states above the Fermi-level [51]. Solid surfaces of copper and silver show reflectances near 100 percent in the energy range below 2.0 eV and 3.9 eV, respectively, which decrease rapidly when interband transitions set in. In the case of silver, the *d*-band absorption around 4 eV overlaps with the collective plasma resonance frequency calculated from the free electron
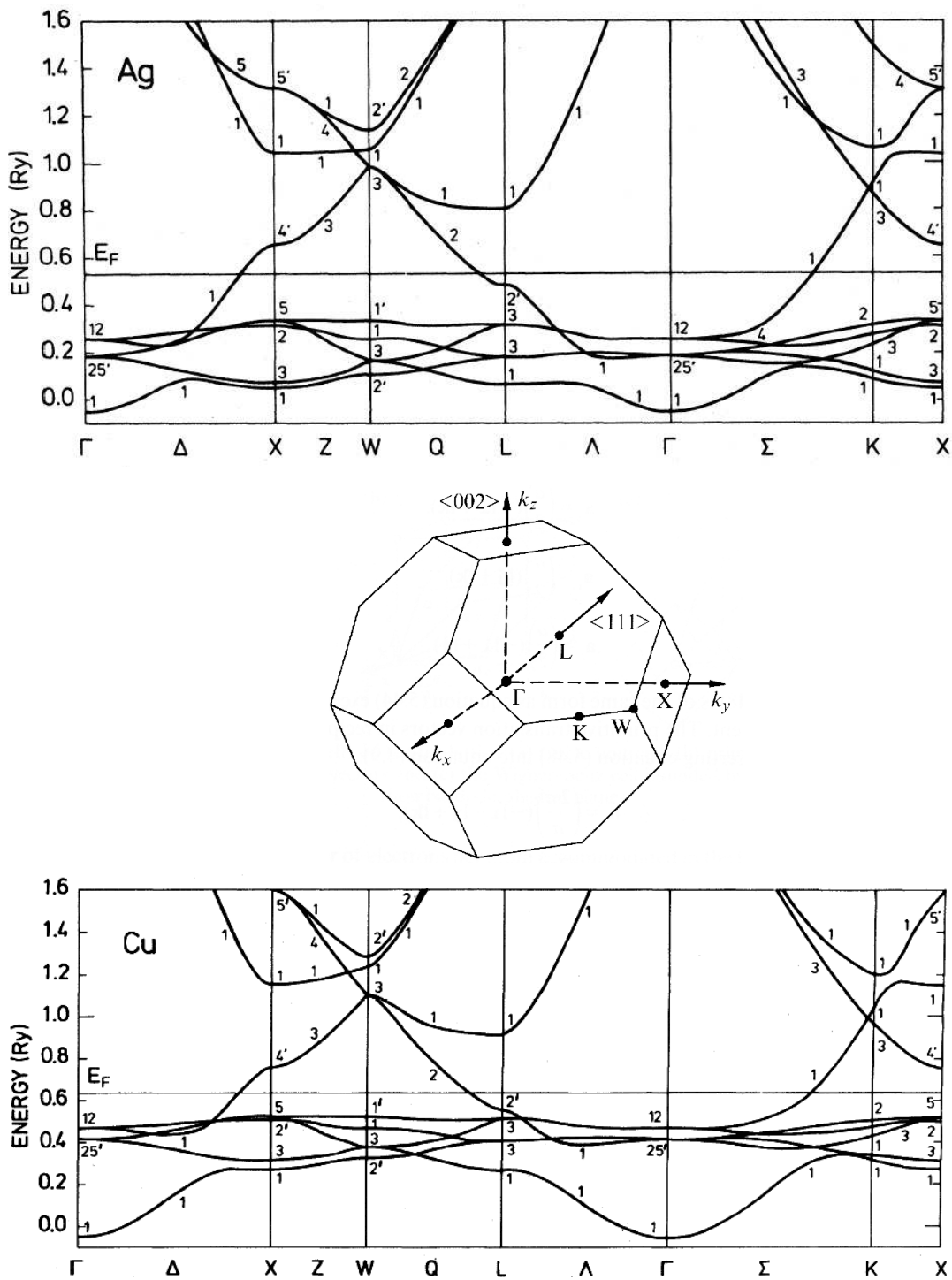
Figure 5.1: *Calculated band structures by Jepsen et al. using the LAPW-method including relativistic band shifts and neglecting spin-orbit coupling [75]. Apart from the narrow region of the d-bands, the Ag and Cu band structures strongly resemble the lowest fcc free electron band. Also shown is the corresponding brillouin zone and their high-symmetry directions. Graphics reproduced from refs. [75] and [51], respectively.*
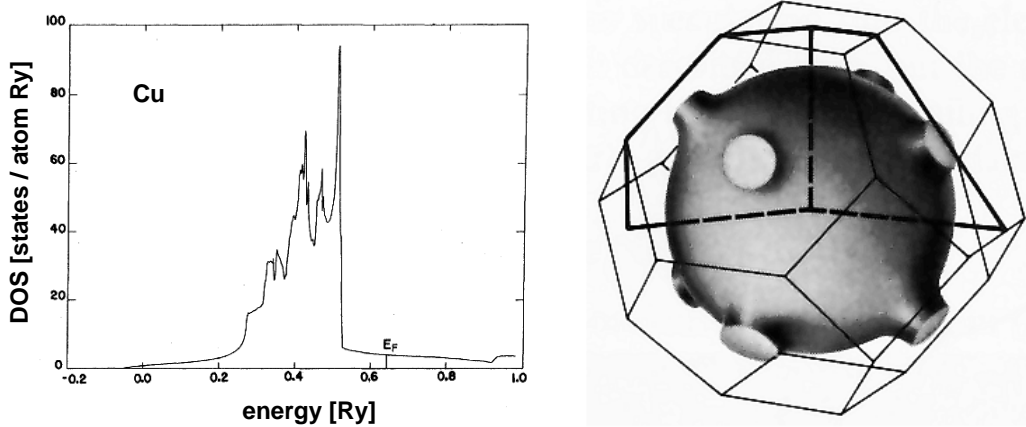
Figure 5.2: *Left: the DOS of copper corresponding to the band structure calculation shown in Fig. 5.1 [75]. Right: the Fermi-surface of a noble metal with eight characteristic necks touching the boundary of the first Brillouin zone close to the [111] directions. Graphics reproduced from refs. [75] and [51], respectively.*

model [67]. Interestingly, a strong absorption at this energy has been found even for very small aggregates of silver atoms. Already clusters as tiny as Ag_8, that were grown using a helium droplet beam [77], show a very narrow absorption line in resonant-two-photon-ionization spectra at 3.96 eV [78]. In Fig. 5.1, calculated band structures for crystalline Cu and Ag show low-dispersed bands derived from the atomic d-states below E_F [75]. The first brillouin zone of the fcc-lattice is also shown in the figure. The largest contributions to the bulk density-of-states (DOS) come from the high symmetry points of the first brillouin zone. The resulting DOS for Cu deduced from the band structure in Fig. 5.1 can be seen in Fig. 5.2. The graph indicates that the highest density of states comes from the ten-fold occupied d-derived bands that are confined to a rather narrow energy interval, while the half-filled sp-hybridized bands give a low but energetically broad contribution. A special feature of the noble metal's band structures is also visualized in Fig. 5.2. The bands crossing the Fermi-energy at E_F result in a Fermi-surface that for the most part is a slightly deformed sphere in reciprocal space. Strong deviations from the nearly-free electron behaviour is only found around the L-points corresponding to the fcc-[111] orientations. Around E_F, no propagating bulk state wave vectors $\vec{k_F}$ can exist in these directions. The so-called neck-width represents the minimum deviation of $\vec{k_F}$ from the [111] directions that allows for a bulk state Fermi-wave vector within the first brillouin zone [79].

5.2   Surface states on the [111] surfaces

The special shape of the Fermi-surface illustrates that there is an energy pseudo-gap of
the bulk electronic states in the vicinity of the [111] directions. The non-existence of bulk
states around the Fermi-energy gives rise to the presence of surface states on the (111)
crystal plane. These states are extended parallel to the surface, while they are confined
to the last few atomic layers in direction of the surface normal. This is due to the abrupt
ending of the crystal core potentials at the surface, which breaks the symmetry in the
normal direction. A basic understanding of surface electronic structure is gained from a
one-dimensional model of a semi-infinite chain of atoms [82]. The unique solutions to this
model in the nearly-free electron approximation are those with a complex wave vector
along the chain, located in the energy gap of the bulk states. These solutions growing
exponentially can be normalized when matched to an exponentially decaying vacuum
wavefunction tail, and therefore do exist only near the surface layer of the crystal. Finally,
the matching conditions define the energetic position of the surface state to a distinct
energy in the gap.

Since surface states and bulk states are orthogonal, the surface state electrons are trapped
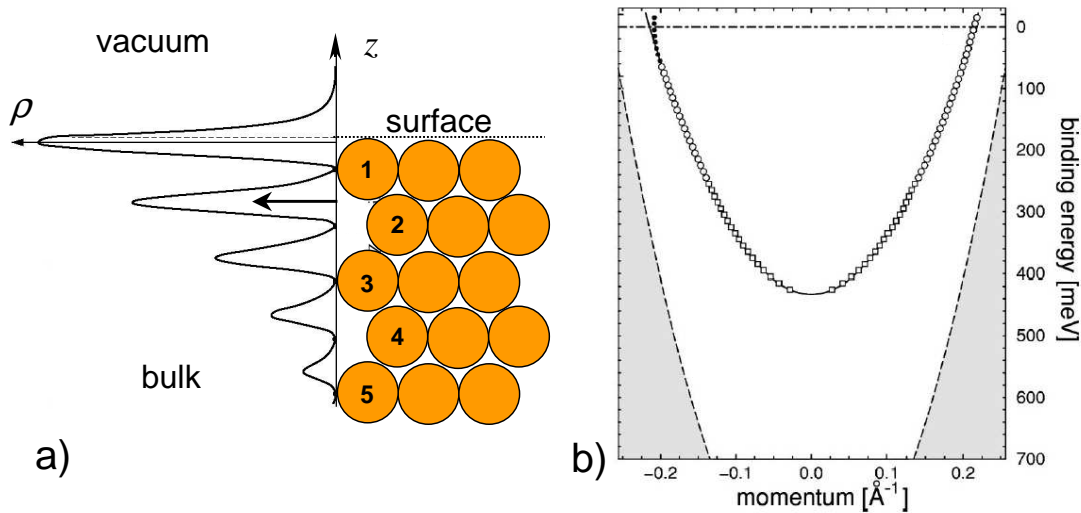

Figure 5.3: *Left: the average charge density for the L-gap surface state of copper as
calculated by Verges and Louis [80]. Nodes occur at the positions of the atomic layers, and
the maximum density lies slightly before the jump of the potential to the vacuum level. The
arrow marks the average $< z >$ of the distribution between first and second layer. Right:
experimentally determined dispersion of the Cu(111) surface state parallel to the surface
by state-of-the-art ARPES [81]. The onset is located at $E_0 = -0.435$ meV and the band
crosses the Fermi-level at $k_F = 0.215$ $\mathring{A}^{-1}$. The curvature determines the effective mass
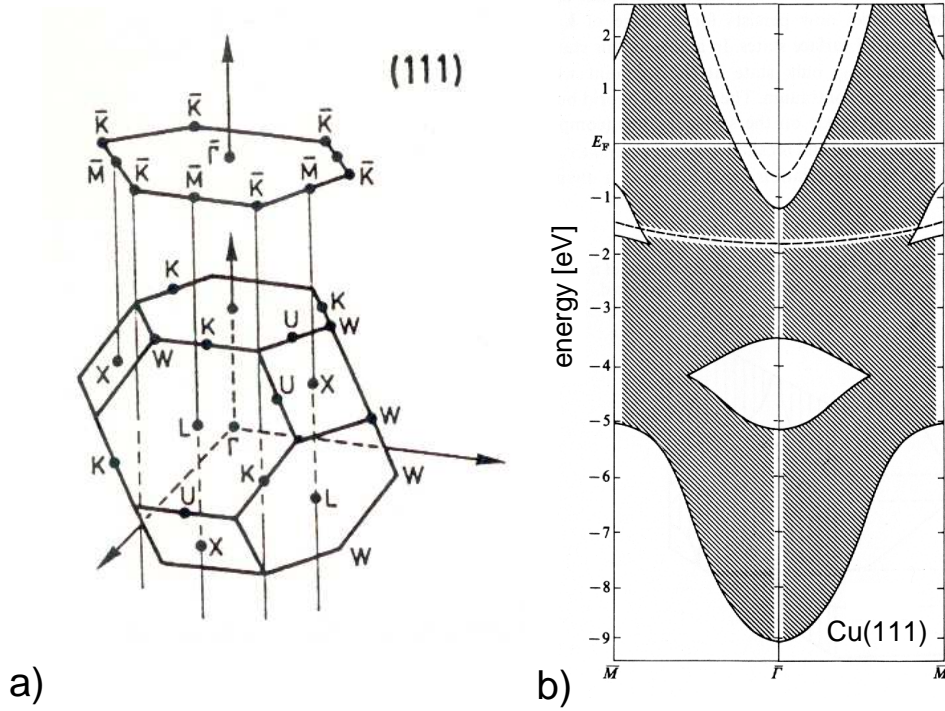to $m^*/m_e = 0.412$. Graphics reproduced from refs. [80] and [81].*

Figure 5.4: *a) The surface brillouin zone in the (111) direction of the fcc crystal structure. Its boundaries are projected from the midpoints of the adjacent planes of the volume brillouin zone and form a regular hexagon. b) Surface band structure of copper in (111) orientation. The hatched areas correspond to bulk states that exist at the given energy and wave vector component $k_\parallel$. Surface states are indicated around Γ in the L-gap and in a gap near the zone boundary above the d-derived bands [83]. This state emerges from the more localized bulk bands due to the strong perturbation of the crystal potential at the surface. Graphics reproduced from refs. [82] and [7], respectively.*

between vacuum and crystal potential in the first atomic layers, as shown in Fig. 5.3. In principle, a propagation within the surface plane is possible, which in case of the noble metals leads to a two-dimensional free-electron surface band structure. These states are not only readily accessible with the STM, but also with other surface sensitive techniques such as angle-resolved photoemission spectroscopy (ARPES) at low photon energies. The surface state band structure can be precisely measured with these methods [81]; recent ARPES results are shown in Fig. 5.3. The dispersion relation of the wave vector $k_\parallel$ parallel to the Cu(111) surface has the parabolic form of a free 2D electron gas described by

$$E = E_\Gamma + \frac{\hbar^2}{2m^*} \cdot k_\parallel^2 \tag{5.1}$$

with the effective mass m^* and the onset of the band edge at a specific energy E_Γ. This surface band located in the L-gap is the classical example for a description of surface states that was given by Shockley in 1939 [84].
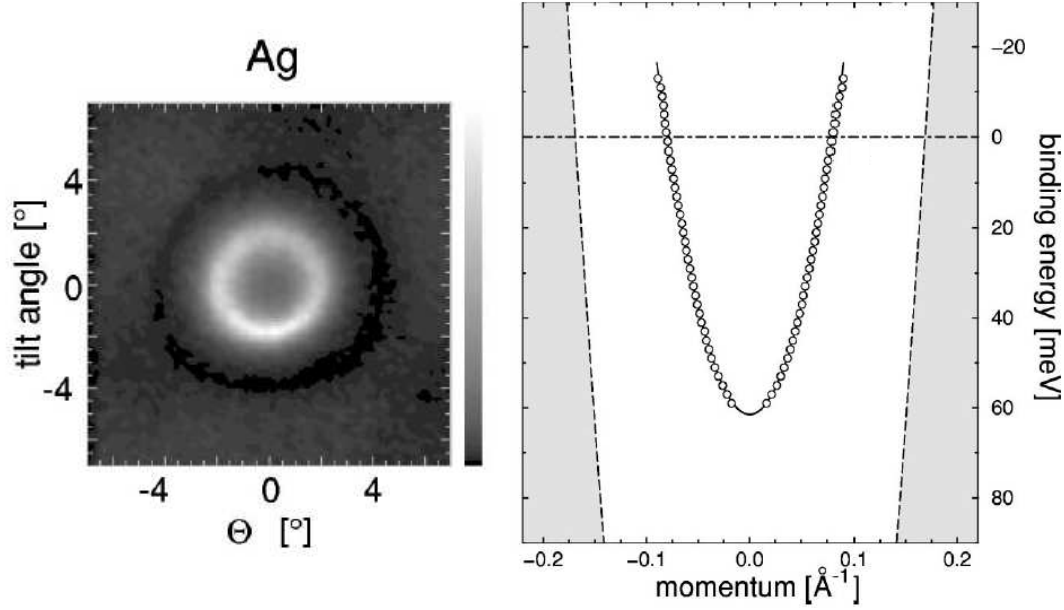
Figure 5.5: *Left: Fermi-surface map (FSM) of the Ag(111) L-gap surface state by ARPES. The measurement demonstrates the perfect isotropy of the surface state dispersion at the Fermi-level. Right: experimental dispersion curve of the Ag(111) surface state by state-of-the-art ARPES [81]. The onset lies at $E_0 = -0.063$ meV and the band crosses the Fermi-level at $k_F = 0.080$ Å^{-1}. The effective mass is determined to $m^*/m_e = 0.397$. Graphics reproduced from ref. [81].*

The shaded area seen in Fig. 5.3 b) corresponds to the Cu bulk-states extending to the (111) surface. The $E(k)$ diagram here refers only to $k_\parallel$, which is the natural quantum number to denote surface state band structures. In general, the properties of solid surfaces are described with the help of a two-dimensional *surface* brillouin zone reflecting the periodicity at the surface. Fig. 5.4 shows how the surface brillouin zone is derived from the bulk zone. Also shown is the result of a six-layer slab calculation for the Cu(111) surface [83], which for a large energy interval visualizes the bulk band structure *projected* on the (111) direction by decomposing the bulk wave vector k into $k_\parallel$ and $k_\perp$, the component in surface normal direction. The Shockley-type states are indicated by the upper parabola, while an additional surface state band is split off right above the bulk d-bands. In a historical classification, this is a Tamm-type state [7], since 1932, Tamm first proposed the existence of surface states by a tight-binding analysis of surface electronic structure [85], which is reminiscent of the d-bands with their rather localized character.

The isotropy of the surface states in the $\vec{k}_\parallel$ directions at the Fermi-energy can be shown in PES using the Fermi-surface mapping technique. An example for Ag(111) is shown in Fig. 5.5, where the detector *tilt angle* parametrizes the surface state wave vector $k_\parallel$. Deviations from the free-electron parabola occur at larger energies of the unoccupied

states, which inherently are not measurable by PES. Using LT-STS, which can probe these states, this has been shown for Ag and Cu in the energy range $[E_F, E_F + 3eV]$ [86]. An energy of 3 eV above E_F corresponds to a $k_\parallel$ about half-way to the first surface-Brillouin zone edge. At even higher energies, calculations show that anisotropy should also arise distinguishing between the $\bar{\mathbf{K}}$ and the $\bar{\mathbf{M}}$ directions (see Fig. 5.4) [86].

5.3 Experimental results

5.3.1 Sample preparation

The following experiments have been conducted on Ag and Cu films that were grown homoepitaxially on single crystal substrates. For more details on the sample preparation see Chapters 3 and 6. A small amount of cobalt impurity atoms has been added intentionally with concentrations below 1 %. These impurities are resolved individually by the STM and can be seen to scatter the surface state electrons, but they are so few in number that the general properties of the sample surface is hardly different from that of a pure homoepitaxially-grown film surface. While in this chapter, we focus on the electronic properties far away from the atomic defects, Chapter 6 is concerned with the investigation of the defects itself, and with the properties of their direct vicinity.

5.3.2 Surface states resolved with the STM

The L-gap surface states have not only been characterized by photoemission very accurately, but also by low-temperature STM, which will be summarized briefly. It was already pointed out that the spectroscopic capabilities of the STM allow to probe occupied as well as empty states of the surface state band by local dI/dU measurements. Scattering of these states at arbitrary surface defects generates standing wave patterns in the $LDOS$ which are resolved in dI/dU mappings as a function of energy. In the vicinity of preferably straight, monatomic step edges, this enables the determination of the surface state dispersion relation directly from real space spectroscopic data. First studies were done on the reconstructed Au(111) surface [87, 88], whereas on unreconstructed Ag(111), the experimental procedure of taking dI/dU data by STM was carefully analyzed regarding the effect of constant current tip height modulations [89]. The starting point of this analysis is the fact that spectroscopic data which is taken at low stabilization bias voltage is strongly influenced by the non-constant tip height oscillations with the Fermi-wavelength leading to a variable tunnelling barrier. In another study on Ag(111) it was demonstrated that such a convolution between dI/dU data and spatial tip height modulations can be mostly avoided by chosing an appropriate stabilization bias voltage [90, 91]. An appropriate choice for U_B in this context is a positive voltage of some hundred meV, that has the effect of largely averaging out the oscillations in the constant current tip height due to
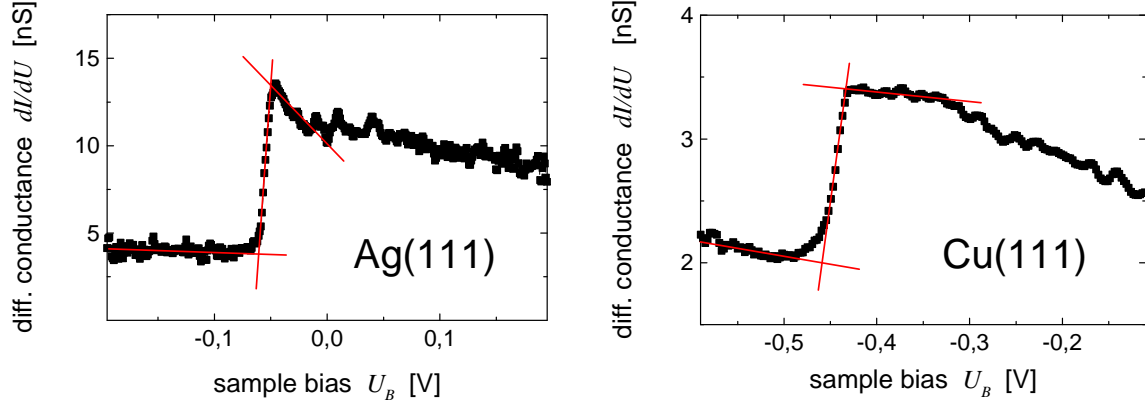
Figure 5.6: *The onsets of the surface states of Ag and Cu show a rapid increase of the differential conductance at E_Γ. The steepest slope of the curve is related to the lifetime of the state with $k_\parallel = 0$, and is clearly different for Ag and Cu. In the case of Ag, judged by the guiding lines, a step in conductivity broadened to 11 ± 1 meV is observed, while Cu shows a broadening of 28 ± 2 meV.*

integration of the tunnelling current over a sufficiently large range of wave vectors. This approach has been followed in all of the STS data acquisitions performed in this work, which on the other hand is necessary for achieving a sufficient voltage range in the $I(U)$ spectroscopic mode.

The dispersion relation of the 2D surface state given by Eq. 5.1 corresponds to a constant density-of-states which is added to an energy-dependent DOS of the bulk state electrons:

$$\rho_s = \rho_b(E) + \frac{m^*}{\pi \hbar^2} \Theta(E - E_\Gamma) \tag{5.2}$$

This correspondence is directly seen in the dI/dU spectra measured on the clean Cu(111) or Ag(111) surfaces as a step-like increase of the differential conductance at the onset energy E_Γ. In principle, this energy can be determined from the spectrum at a single, ideal surface location. Additionally, a measure of the lifetime of electron holes can be gained at the bottom of the surface state band that are left behind by the electrons tunnelling to the tip [92]. Two examples of well resolved measurements on Cu and Ag are shown in Fig. 5.6. They have been measured at $T < 8$ K on room-temperature grown homoepitaxial thin films on (111)-oriented single crystal substrates. The Ag spectrum is an average of several hundred single spectra on a narrow terrace of some nanometers in width, which leads to a notable up-shift of the surface state band with $E_\Gamma = 0.055$ eV. This shift is due to confinement of the surface state electrons by the terrace boundaries, but should not be analyzed quantitatively at this point. The Cu spectrum represents the spectra on a comparably large, 28nm in diameter hexagonal island averaged over an area of about $(5 \text{ nm})^2$ and interestingly shows no up-shift of $E_\Gamma = 0.442$ eV.

The Ag spectrum is a bit of a touchstone measurement for testing the spectral resolution in the STS mode, since apart from the superconducting density-of-states of a Nb crystal at very low temperatures or the Kondo-resonance of a magnetic adsorbate atom, the onset of the Ag surface state is a rather sharp feature to be resolved in a STS measurement. The slopes measured in our lab (see caption of Fig. 5.6) are very close to those reported by Kliewer *et al.*, who published onsets rising within 9 meV. The lifetime connected to this width has been found to be dominated by a surface state intraband transition from occupied states on the surface state parabola to the electron hole at E_Γ, and not by interband transitions from the bulk states [93]. It is interesting to point out that the present measurement on Ag shows that the lifetime obviously is not affected, or only very little, by a confinement in one dimension in this case. We will see in the following that 2D confinement leads to quantized levels that exhibit increasing broadening with level energy. Regarding the performance of our experimental setup and the subsequent data processing, this demonstrates that highest quality data can be acquired using the tunnelling spectroscopy method described in Section 2.4.1.

5.3.3 Quantum confinement of surface state electrons

Confinement of surface state electrons occurs between extended surface defects such as monatomic steps or rows of adatoms. This is not a trivial fact, since it becomes clear from Fig. 5.3 that the charge density of the Cu(111) surface state is not restricted to the surface layer of the crystal alone. Although the surface state extends several layers down into the crystal, the effective potential created by a monatomically high island on a Ag(111) surface can be described by a 2D particle-in-a-box model. The study of 1D confinement between adjacent step edges with STS by Bürgi *et al.* has revealed that monatomic steps on Ag(111) are accurately described by a finite reflection coefficient $r(E) < 1$ and a constant scattering phase shift $\phi \sim -\pi$ [94]. However, the most widely known experiments demonstrating surface state confinement are the *LDOS* measurements in artificially assembled, so-called *quantum corrals* of adatoms that were geometrically arranged with the STM tip on noble-metal surfaces [95]. Much work has been devoted to theoretically describe the effects that spherically symmetric structures have on the surface state *LDOS* [96, 97, 98]. Yet, island structures on RT-grown metal films show equivalent effects that will be examined in the following paragraphs.

Ag(111)

During film growth on (111) noble metal surfaces, nanoscale islands of different sizes with hexagonal symmetry are developed, which create a 2D confinement for the surface state electrons. Such island structures on Ag(111) have already been shown to display quantum confinement effects by Li and coworkers, who recorded dI/dU spectra and maps of such objects [99]. In addition, they calculated the eigenstates of a particle in a hexagonal box
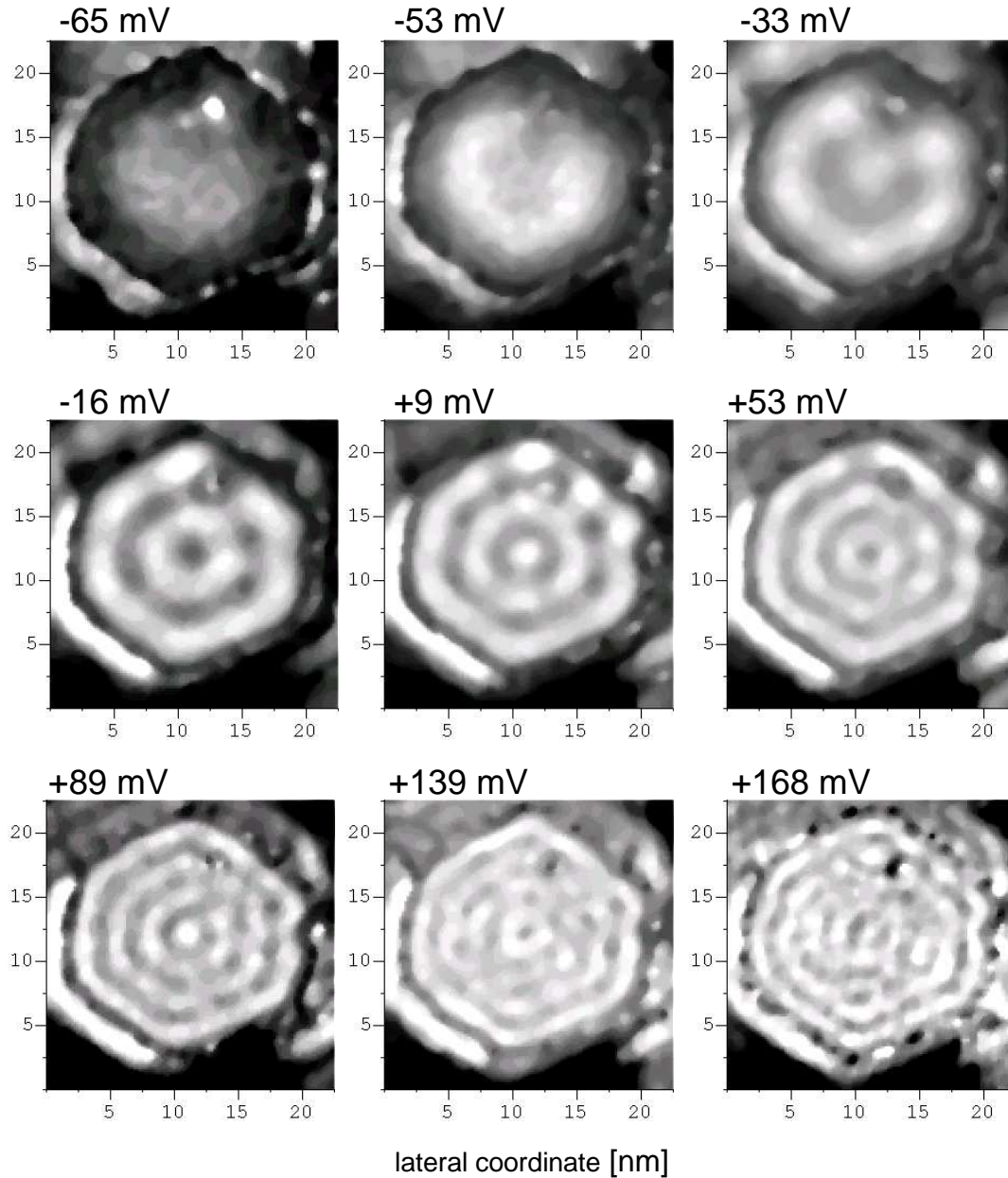
Figure 5.7: *Local conductivity maps of an Ag island at characteristic sample bias voltages (setpoint $U_B = 0.6$ V, $I_T = 0.8$ nA). Light areas indicate regions of LDOS maxima, while the image contrast is chosen for best visibility. The size of the island is $\Omega = 255 \pm 10$ nm^2 corresponding to an average inner diameter of $d_{av} = 16.0 \pm 0.3$ nm of a perfect hexagon. The defect clearly seen at -65 meV has a strong impact only locally, and only on low-energy states that are displayed in the first five images.*
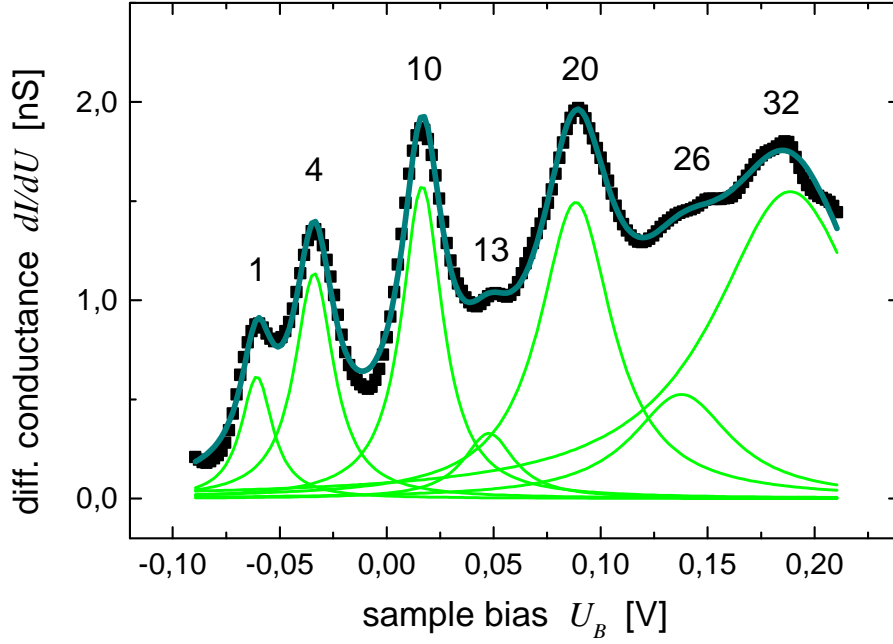
Figure 5.8: *Differential conductance (dI/dU) spectrum taken at the island centre. The curve is an average of 36 single spectra from an area of $\sim 1.2 \times 1.2$ nm. The experimental spectrum can be fitted very well by seven Lorentzians that are attributed to distinct single-particle states (see text), which are indicated here by their quantum number n.*

for comparison. Good agreement was found if the model potential with walls infinitely high coincides with the lateral position of half the step between island and terrace levels in a constant current image. Since the eigenenergies of the states confined to the island do simply scale inversely with the island area Ω, their theoretical results can readily be used for the analysis of the data gained in this work.

Fig. 5.7 displays the results of a spectroscopic scan of an $\Omega = 255 \pm 10$ nm^2 Ag island as local differential conductance maps. As a function of sample voltage, characteristic patterns of sixfold symmetry evolve from a broad, single central peak to increasingly complex structures that represent the $LDOS$ of the confined surface state electrons at the given energy. Note the development from maximum to minimum in the centre of the island with increasing bias voltage. These $LDOS$ patterns do not represent independent eigenstates of a hexagonal box but they rather are the sum of several overlapping elementary modes [100] (see also Appendix A). A direct comparison of the modes calculated by Li *et al.* with the $LDOS$ maps therefore is problematic. Instead, the authors proposed to analyze the dI/dU spectrum acquired in the centre of the island. Here, only those elementary modes contribute to the $LDOS$ which transform according to the A_1 representation of the C_6(6mm) symmetry group of the hexagon, which helps to separate the multitude of states.
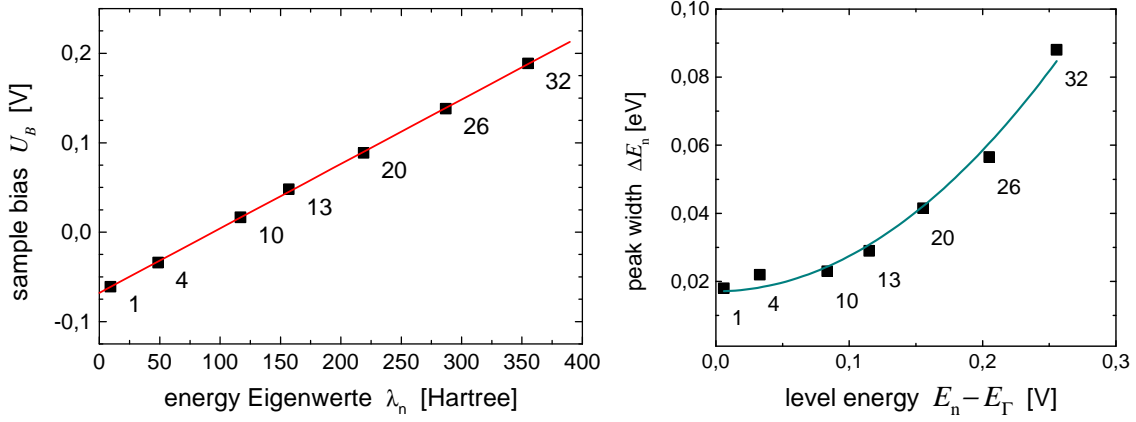
Figure 5.9: *(left) The energetic positions of the experimental peaks gained from the spectrum fit in Fig. 5.8 plotted against the eigenenergies of the relevant states calculated by Li and coworkers [100] (1 Hartree = 27.21 eV); (right) The width of the Lorentzians starts at a finite value near E_Γ and grows smoothly with energy, approximated by a quadratic function.*

Fig. 5.8 shows the central spectrum of the island, which due to its relatively large size exhibits a relatively narrow spacing of levels. The dI/dU curve is strongly structured, unlike the spectrum on a terrace that is shown in Fig. 5.6. A fit with multiple Lorentzians determines the energetic positions and the widths with very good accuracy (most error bars below 1 meV - not shown in the graphs). It should be mentioned that the levels which corresponds to $n = 13, 26$ and 32 have not been resolved in experiment before, but they can be seen clearly in the spectrum presented here. For $n = 13, 26$, the small weight of the states produce only shoulderlike features, while the observation of $n = 32$ is mainly owed to the large size of the island investigated. Less accurately, states with even higher quantum numbers were resolved. Our experimental results are compared to the theoretical values of the hexagonal box (see Appendix A) reported in [100]. As plotted in Fig. 5.9, the experimental and theoretical values are linked by a perfectly linear relation. This requires an accurate calculation of levels as well as the appropriate linear scaling with island size. The scaling is given by

$$E_n = E_\Gamma + \frac{\lambda_n}{m^*\Omega} \qquad n = 1, 2, 3..$$ (5.3)

which provides a way to determine the effective mass and the onset of the surface state band from the present experiments. The band edge energy E_Γ is given by the constant term of the linear fit, and m^* by its gradient, which are found to be $E_\Gamma = -68 \pm 1$ meV and $m^* = 0.41 \pm 0.02$. The accuracy of Ω was validated by calibrating the microscope's output with the atomic resolution image of Ag(111) shown in Fig. 2.3. Of a second, smaller island, an identical analysis was made, the values of which show very good agreement with the above numbers [23]. This emphasizes the feasibility of a determination via the scaling

relation Eq. 5.3, since our values agree well with most of the other experimental data. A compilation can be found in Ref. [91].

The second quantity plotted in Fig. 5.9 is the width of the Lorentzians fitted in Fig. 5.8. A smooth increase of the experimental level broadening with their energy is evident. The plot suggest a quadratic dependence, which was fitted to the data, as seen in the figure. The finite width of the peaks, indicating a finite lifetime of the confined states, and the characteristic envelope of the spectrum have theoretically been traced back to defect scattering at the confining surface defects. This provides the coupling between surface states and extended bulk states of the crystal [96, 97]. Introduction of a self-energy of the form

$$\Sigma(E) = \alpha(k_B T) + \beta(E - E_F)^2 \tag{5.4}$$

which considers quasi-particle interactions according to Fermi-liquid theory also reproduces the finite width of the lowest-lying level that is lacking simpler theories [98]. Experimentally, Li and coworkers have reported an approximately linear increase of the level width with energy. At the cost of a less convincing agreement, our data could also be described linearly around E_F. However, the large width of the $n = 32$ state is clearly off the line. A source of uncertainty for the widths is that the island spectrum was cut off above the $n = 32$ state and contributions due to the overlap with broadened higher levels are not accounted for in the fit. Therefore, the parameters of the higher states are subject to some corrections, but we expect that this is the case for the relative weight much more than for the width of the single peaks.

Cu(111)

The *quantum corral* experiments of Crommie *et al.* have been performed on the Cu(111) surface, using Fe adatoms as confining scatterers [95]. In the present experiments, the Cu surface state is confined to hexagonal islands as in the case of Ag in the preceding paragraph. From STM experiments on Cu it is evident that strong scattering of the surface state occurs at step edges [87, 90]. PES experiments on regularly stepped surfaces vicinal to (111) have also indicated electron confinement in 1D for the Cu surface state [101], which has already been concluded previously in a combined STM and PES study [102]. Thereafter, monatomic steps represent relatively transparent barriers, reflecting about 60 % of the Cu(111) surface state electrons, which also allows for a coherent 2D dispersion on a vicinal surface.

Tunnelling spectra that were acquired on a large Cu island (inner diameter ~ 27.5 nm) are shown in Fig. 5.10. Every point of this spectra section image, which resolves the electronic properties along the line spatially, is averaged from 7 single spectra probing a 15 Å wide area with a resolution of 2 Å. Single quantum states at the bottom of the surface state band, as they were observed in the measurements on the Ag islands, were not resolved on this large Cu island. However, the *LDOS* oscillations seen in Fig. 5.10 suggest that in the

vicinity of the step, we may try to analyze the energy dependence of the standing wave pattern by disregarding the other five island borders, and use the description for simple step edge scattering. The *LDOS* of 2D electrons scattered at an ideal, straight step edge is essentially given by [103, 104]

$$\rho(k_\parallel, x) \propto 1 - J_0(2k_\parallel x), \tag{5.5}$$

J_0 being the zeroth-order Bessel function of the first kind. It can be evaluated as a function of $k_\parallel$ at a fixed distance x_d from the step. This has the advantage that we can make use of the good energy resolution of the experimental data, and we omit the complications that arise from tip height variations in the spatial regime. Thus, we simply use the extrema of Eq. 5.5 instead of fitting spatial profiles to the data.

As indicated in Fig. 5.10, a dI/dU spectrum was extracted at a distance $x_d = 7.6 \pm 0.2$ nm from the step. This spectrum, which is plotted in Fig 5.11 a), exhibits a series of local maxima and minima, shown by the arrows, whose energetic positions can be determined easily. Each extremum corresponds to a certain $k_\parallel^i x_d$ that defines the respective wave

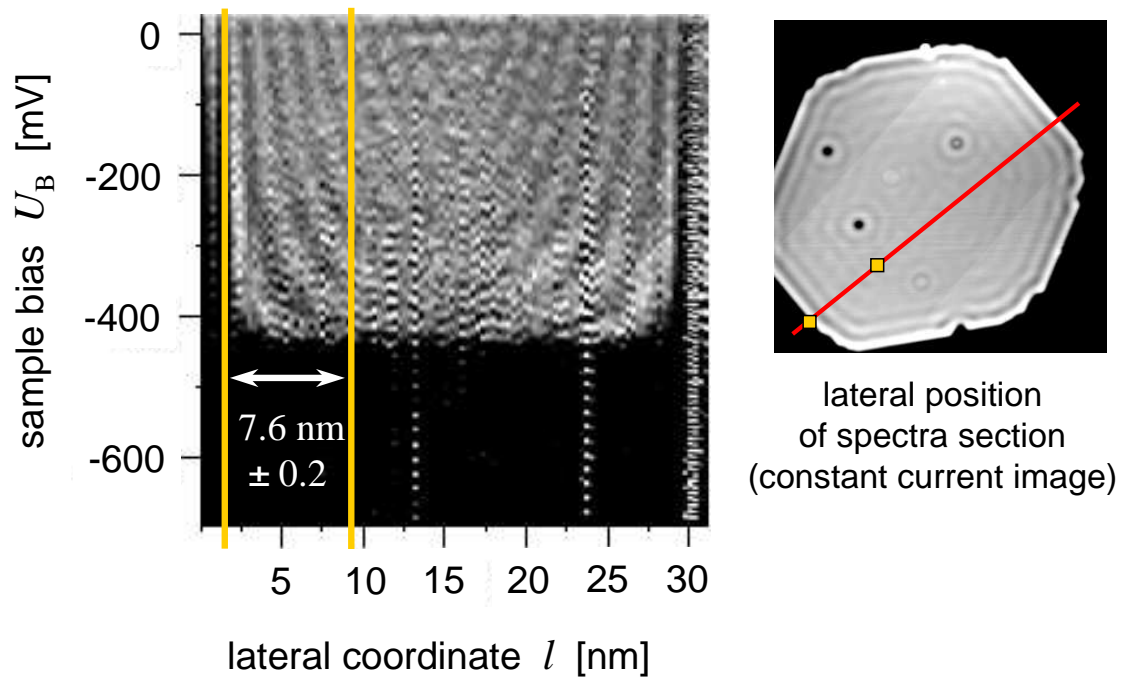lateral position
of spectra section
(constant current image)

Figure 5.10: *Left: Grey-scale representation of the dI/dU tunnelling spectra across a large Cu island resolved along the section indicated in the topography image (spectra section; $U_B = 0.6\,V$, $I_T = 0.8\ nA$). The spatial dependence of the spectra shows the energy-resolved standing wave LDOS due to surface state scattering at the island boundaries. The atomic defects visible in the island are analyzed in detail in the following chapter (see Fig. 6.8).*
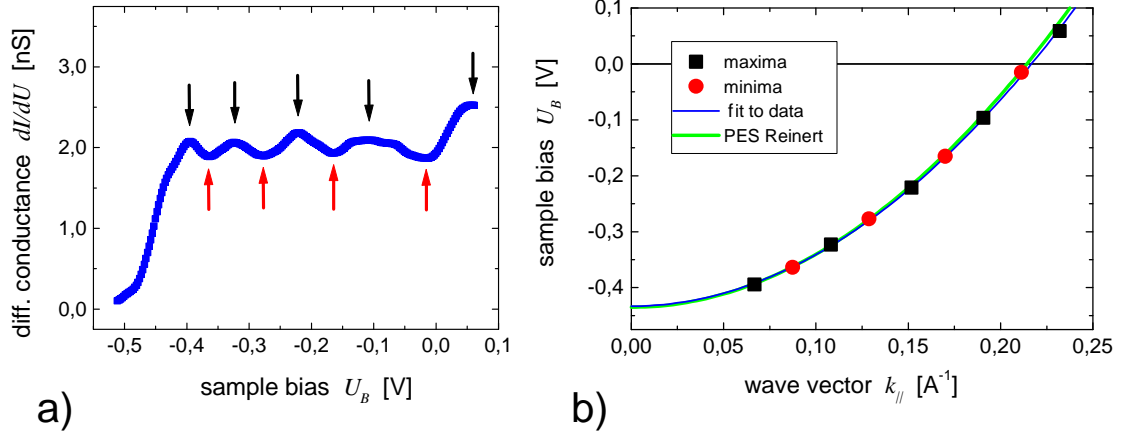
Figure 5.11: *a) dI/dU spectrum 76 Å from the island edge which is marked by a vertical line in Fig. 5.10. b) The energies of the maxima and minima in the spectrum, assigned to the corresponding wave vectors (see text), can be plotted to reproduce the dispersion of the Cu surface state. The PES result from Fig. 5.3 is also shown for comparison.*

vector, delivering a number of points on the dispersion curve of the Cu(111) surface state. The distance $x_d = 7.6$ nm was chosen to have a sufficient number of well defined extrema in the region of occupied states. As before, the accuracy of the determination of x_d was calibrated using the atomic resolution image of Ag(111) from Fig. 2.3. The resulting data set is displayed in Fig 5.11 b). The errors in determining wave vectors and energies are within the symbol sizes. The most critical quantity is the distance x_d that defines the hard-wall boundary condition for the wave function in Eq. 5.5. A parabola fitted to the data points returns the parameters E_Γ and m^* of the Cu(111) surface state dispersion curve. The onset of the band is found at $E_\Gamma = -433 \pm 2$ meV, and the effective mass is determined to $m^* = 0.40 \pm 0.02$ meV. The error in m^* is dominated by the uncertainty of x_d, that amounts to 2 Å due to the spatial resolution of the data. Apart from that, the right choice in defining the boundary position from the data is not just clear. In our case (see Fig. 5.10), it was placed in the middle of the dark vertical strip of low conductance, an energy-independent minimum indicating the island edge. Nevertheless, compared to the second dispersion curve drawn in Fig. 5.11, which is based on the values found by Reinert *et al.* (Fig. 5.3), our STS data demonstrates a high degree of agreement with photoemission results.

5.4 Conclusion

Spatially resolved STS was used to characterize the L-gap surface state electron bands of Ag(111) and Cu(111). Area-averaged differential conductance spectra show the well-

known sharp, steplike increase in the *LDOS* that is typical for a 2D electron system. Hexagonal islands, prepared by homoepitaxial film growth, represent a confinement for the surface state. Islands on Ag(111) exhibit characteristic, energy-dependent *LDOS* patterns as a result of electron confinement. Local *dI/dU* spectra show a progression of the seven lowest states with non-zero weight at the island centre, which corresponds to *all of* the theoretically predicted confined single particle states. This is more than the four strong peaks resolved previously by Li *et al.* [99]. Their theoretical analysis was used to determine the onset energy $E_\Gamma = -68 \pm 1$ meV, and the effective mass $m^* = 0.41 \pm 0.02$ meV for the Ag(111) surface state. On Cu(111), the surface state confined to a large island was analyzed in terms of the 1D description of step edge scattering. This treatment yields a dispersion curve with parameters $E_\Gamma = -433 \pm 2$ meV and $m^* = 0.40 \pm 0.02$ meV. In both cases, the numbers extracted from the experiments are in very good agreement with previous results gained by STM and PES. This confirms the quality of the present measurement and data processing methods. On Ag(111), the width of the levels has been found to increase with level energy, suggesting a quadratic dependence of electron lifetimes with energy, which is understood in theory, but in contrast to the findings from previous experiments.

Chapter 6

Kondo effect of Co atoms in Cu(111) at $T < 8$ K

The first tunnelling spectroscopy experiments of *embedded* Kondo-impurities in a dilute magnetic alloy surface are presented in this chapter. Kondo-alloys were prepared by homo-epitaxial growth of Cu(111) films containing small amounts of Co atoms. This system was probed using spatially resolved STS performed at low temperatures below 8 K. Single Co atoms lying in the surface layer of the Cu matrix show a characteristic, symmetric dip in the differential conductance at zero bias, indicating the presence of the many-body Kondo-resonance [105]. The Kondo-temperature of these *embedded* Co impurities is found to be $T_K = 405 \pm 35$ K and thus is much higher than the T_K-values that were previously reported for Co *adsorbate* atoms [106, 107].

6.1   Probing single Kondo-impurities

The properties of magnetic transition metal atoms within nonmagnetic host metals have been subject to intense research dating back to the 1930ies [108]. In certain cases, the physical properties of such dilute magnetic alloys show an unusual asymptotic behaviour in the low temperature limit, which first has been observed in the bulk resistivity of noble metals [109]. Here, the typical anomaly consists of an unexpected increase in the resistivity towards low temperatures, for which a first theoretical explanation was given by Kondo in 1964. He showed that the resistivity increase is connected to a low-temperature divergence of spin-dependent scattering of the conduction electrons at residual magnetic moments localized at transition metal impurities [110]. The consequences of this behaviour which nowadays is summed up in the term *Kondo-effect* were characterized with macroscopic methods during the past decades, while most extensive data was gained for dilute 3d transition elements in Au and Cu host metals [111]. These systems have now gained new

scientific attention since recently isolated impurities could be investigated on the atomic scale [112, 113]. Magnetic impurity atoms at the surface of noble metals are accessible with the STM tip, which makes it possible to reach ultimate experimental resolution for single surface Kondo-systems.

Using the capabilities of scanning tunnelling spectroscopy (STS) at low temperatures, recent work has been focused on isolated 3d- and 4f-impurity atoms *adsorbed* on noble metal surfaces. Several material combinations have been examined comprising Ce on Ag(111) [112], Co on Au(111) [113], Ti, V, Cr, Mn, Fe, Ni on Au(111) [114], Co on Cu(111) [106, 107] and Co on Ag(111) [115]. Only some of these adsorbed impurities, namely those with small magnetic moments in the atomic configuration and a high T_K as a bulk system [111], have shown a characteristic behaviour in tunnelling spectroscopy measurements. The characteristic fingerprint found in the dI/dU spectra recorded with the tip on top of the impurity atom is a sharp dip in the differential conductance at zero bias. In the case of a Co adsorbate on the Cu(111) surface, a slightly asymmetric dip was observed in two independent STS studies [106, 107]. The width of this spectral feature corresponds to the Kondo-temperature T_K of the system and is found to be very small for adsorbates, within the range of 10 mV at L^{4}He-temperatures. The Kondo-temperature T_K is a system-specific parameter denoting the temperature around which the system undergoes a gradual phase transition to the Kondo-state.

Theoretical work based on Kondo's spin-scattering Hamiltonian [116] predicts a scaling of T_K with the local electron density ρ_0 which can be written

$$T_K = T_0 \cdot exp\left(-\frac{1}{J_{eff} \cdot \rho_0(r)}\right) \tag{6.1}$$

J_{eff} denotes the effective exchange constant between two spins in the Kondo-state and $\rho_0(r)$ the *DOS* at the Fermi-energy which is position dependent at the surface ($LDOS(E_F, r)$). Therefore, a difference should be expected in experiment if either the Co atom is adsorbed on the surface of the host metal or it is embedded in the host's first surface layer. Geometrically seen, the coordination number of such embedded Co impurities in or below the surface is considerably enhanced compared to the adsorbate case. Moreover, it is clear that the embedded Co atom has not only more overlap with the bulk states of the host metal, it is also located within the maximum of the charge density due to the Shockley surface state on (111)-oriented noble metal surfaces (see also Fig. 5.3). It is still not clear, which role surface states play in the formation of the Kondo-resonance. Manoharan and coworkers could show that an elliptical electron resonator constructively reflects the spectroscopic signature of a single Co atom placed in its one focus via the surface state electrons to the other focal point of the ellipse [106]. However, the signal is very weak, possibly indicating a negligible amount of the surface state's contribution.

In the present work, single *embedded* Kondo-atoms were studied for the first time with the high spatial resolution offered by STM. As dilute magnetic impurities, small amounts of Co atoms were added via co-evaporation to a thin Cu film grown epitaxially at room
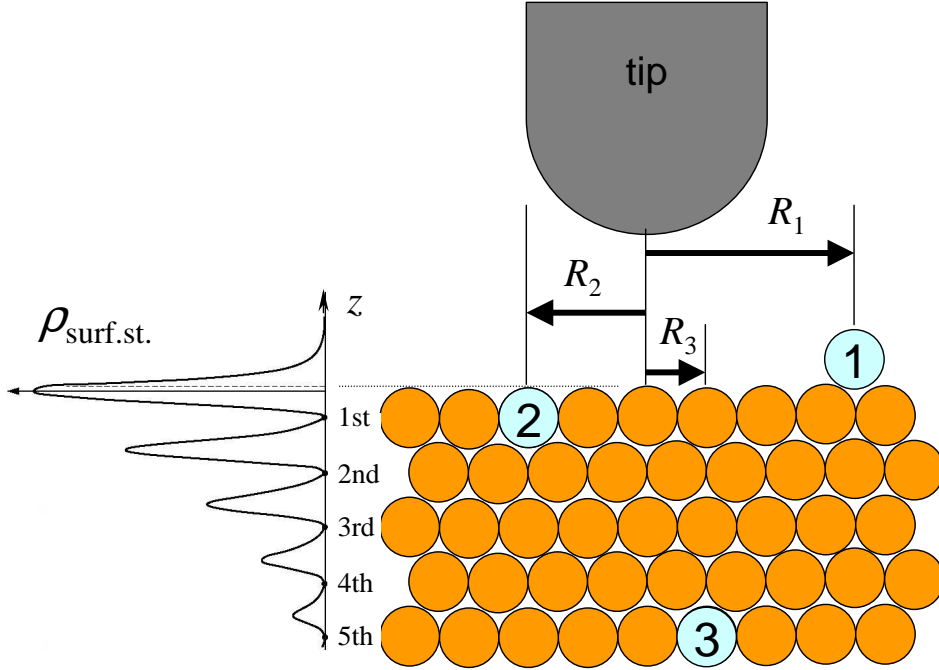
Figure 6.1: *Sketch of an STS experiment probing impurity atoms. On top of adsorbates (1), the tip is retracted from the surface layer, while above an embedded atom (2) it roughly stays at a constant height. Buried impurities (3) may also modify the electron density at the surface in a characteristic way.*

temperature on a Cu(111) single crystal substrate. This sample preparation provides the closest approximation of a bulk Kondo-system which still is accessible with a surface-sensitive technique like STM. After all, *bulk* Kondo-temperatures are known only very inaccurately, while the determination of T_K for *adsorbates* using STS has been possible with only limited errors. The experimental values available for dilute Co in bulk Cu vary in a wide range. Depending on the method, and presumably also on the specimen that was employed, T_K were determined between 240 K and 1000 K [111, 117]. A study by Tournier and Blandin probably gives the most accurate result for the bulk-value of T_K. Being aware of the influence of pair interaction and clustering, they studied relatively high as well as low concentrations of Co in a Cu matrix [118]. From their susceptibility measurements, they extracted an *s-d* interaction spin fluctuation temperature for single impurities of $T_{sf} = 530K$, which is a different way of expressing the transition temperature T_K as separating between the limits of strong and weak *s-d* interaction.

Cobalt atoms adsorbed on Cu surfaces have recently been investigated by Knorr and coworkers using low-temperature STS [107]. In their study, the substrate orientation was varied in order to characterize the dependence of T_K from ρ_0. As a result, the Kondo-
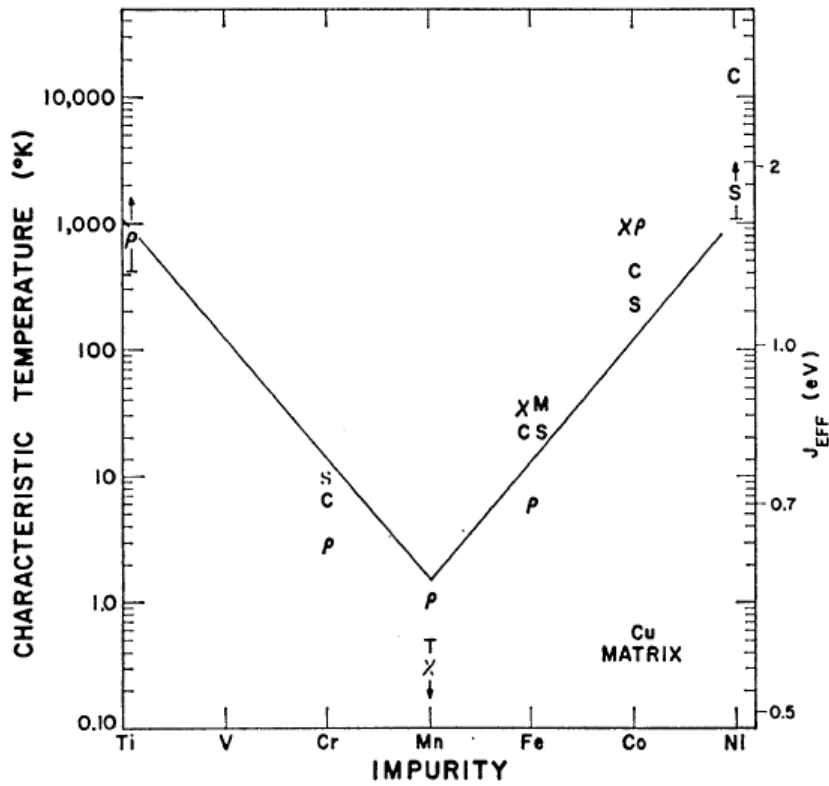
Figure 6.2: *Kondo-temperatures of the 3d transition elements in bulk copper. The value of* $ln\ T_K$ *varies systematically with the number of unpaired atomic 3d electrons. The symbols stand for different macroscopic methods to determine* T_K: χ *susceptibility,* ρ *resistivity, c specific heat, s thermopower. Graphics reproduced from ref. [111].*

temperature seems to scale with the number of nearest-neighbour substrate atoms of the Co impurity. This suggestion was based on the dI/dU spectra of Co atoms on (111)- and (100)-oriented Cu surfaces, corresponding to 3 and 4 nearest-neighbour atoms. A simple model was proposed by the authors that assumes a proportionality between the product $J \cdot \rho_0$ and n, the number of nearest-neighbour atoms. Since the bulk value of T_K is not very accurately known, it is desirable to measure the Kondo-temperature of embedded Co in the Cu surface locally by STS. A problem not yet addressed in current work is the influence of the topography profile in adsorbate studies. Especially when measuring the spatial dependence of the spectra, the tip is substantially changing its height over the substrate, while it is approximately keeping a constant distance to the adsorbate. This should strongly influence the experimental spectra and complicates the comparison with theoretical results, which simply assume a constant tip height. The present experiments go beyond the adsorbate case and examine surface and subsurface impurities. It will be shown that studying embedded impurities reduces the tip-heigth problem and provides new information that agrees better with present theoretical predictions.

6.2 The Kondo-Effect

6.2.1 Phenomenology

The special properties of dilute magnetic alloys as they were measured with various macro-scopic methods have been summarized in several review articles [119, 111, 117]. Since the original literature on this topic is abundant, a brief summary of general results on Kondo-systems is presented here on the basis of ref. [117]. This picture has emerged from numerous studies on various systems, and there is hardly one system showing all the typical properties together in the clearness suggested by Fig. 6.3.

The *magnetism* of magnetic ions in hosts like Au and Cu is the quantity that is most directly related to the nature of the Kondo-effect and can be examined by susceptibility measurements. The typical behaviour at high temperatures is that the ions appear as free magnetic moments which show a paramagnetism according to the Curie-Weiss law in addition to the Pauli-paramagnetism of the host metal. If the temperature drops below the specific T_K of the system (see Fig. 6.2), the ions appearantly lose their magnetic moment as displayed in Fig. 6.3 and contribute no longer to the temperature dependence of the susceptibility curve. As mentioned before, this is a gradual process under which also other physical quantities show an anomaly or a transition to a distinct low-temperature behaviour.
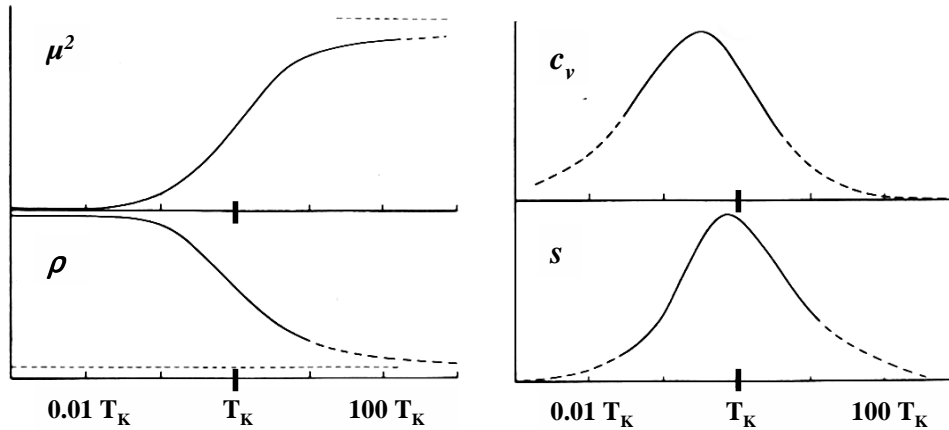

Figure 6.3: *Low-temperature Kondo-anomalies extracted from the temperature dependence of the properties of various dilute magnetic alloys. The symbols stand for different macro-scopic quantities: μ magnetic moment, ρ resistivity, c specific heat, s thermopower. The curves represent only the Kondo-contribution and must be thought as addition to the normal temperature dependence of the host properties. Graphics reproduced from ref. [117].*

The residual *resistivity* due to the impurities increases below T_K up to a saturation value towards $T = 0$ (see Fig. 6.3). If the Kondo-temperature is not too low, this saturation follows a resistivity minimum, that is formed by the increasing electron-phonon scattering rate to higher temperatures. If T_K is high, experimental data may only comprise a broad transition region to the saturation regime without a distinct resistivity minimum. The experimental data above T_K can be fit well using the *s-d* model introduced in the next section only when assuming an impurity spin of $\frac{1}{2}$ instead of the total spin of the free transition metal atom.

Furthermore, the *specific heat* as well as the *thermopower* show broad peaks around T_K, as is also shown in Fig. 6.3. These anomalies extend over a range of about two orders of magnitude in temperature T, which stresses the gradual character of the phase transition connected with the Kondo-effect. The extrema of the different experimental curves do not fall on the same temperature, and a deeper analysis is necessary to understand the relation to T_K [117].

6.2.2   Theoretical models

The first theoretical explanation of the low-temperature behaviour of dilute magnetic alloys by Kondo has been based on the *s-d* interaction model [110]. This model explicitly assumes that the alloy is in a magnetic state and the impurity atoms immersed in the host metal actually form local magnetic moments. From a more general viewpoint, it is not clear that this shall be the case for such an alloy. In Kondo's model, it is completely left out due to which mechanism the moments are formed. Using a different model, Anderson described the conditions necessary for the presence of localized magnetic moments in the limit of a single impurity and non-degenerate as well as degenerate *d*-states. This single impurity Anderson model (SIAM) is the widest-used model for Kondo-systems today, and although it does not account for any interactions between the magnetic moments as they will be expected in a real alloy, it was found to explain the experimental observations rather well in many cases [12]. Some years later, Schrieffer and Wolff used a canonical transformation to relate the SIAM Hamiltonian to the *s-d* interaction model of Kondo. They showed that both approaches are equivalent in the limit of single occupation and small *s-d* mixing, which according to Anderson are the conditions for a magnetic state of the system. The low-temperature behaviour of Kondo's model therefore is also contained in the Anderson-model, which only implicitly regards spin interaction via a Coulomb term for doubly occupied *d*-orbitals. The following paragraphs should give a short overview over the properties and results of these two important models for dilute magnetic alloys.

The *s-d* exchange model

This model was examined by Kondo due to the fact that experimental evidence suggests a connection between the formation of localized moments in an alloy and the anomal low-
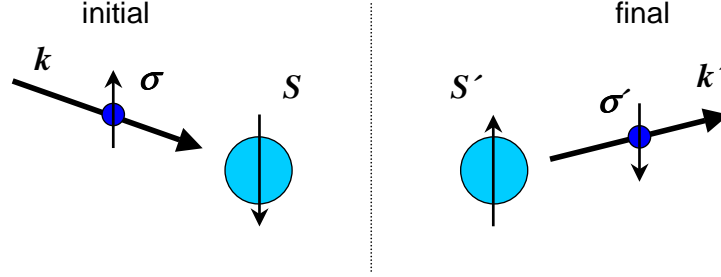
Figure 6.4: *Schematic diagramm of the spin-flip scattering in the s-d exchange model. Shown is the process corresponding to the S_+ term in Eq. 6.4.*

temperature increase in its resistivity [120]. The *s-d* exchange model was first introduced by Zener [121] and does neither make specific assumptions about the individual properties of the metals involved, nor does it consider correlations between localized spins of the alloy. It only uses a spin-spin exchange term as it is known from the Heisenberg model defining the exchange constant J between the local impurity spin $\vec{S}$ positioned at $\vec{R}_0$ and those of the delocalized band electrons $\vec{\sigma}$:

$$H_{sd} = -J\,\vec{S}\cdot\vec{\sigma}(\vec{R}_0) + V. \tag{6.2}$$

The term V corresponds to ordinary potential scattering at the embedded ion. That the nature of the localized states is not explicitly considered in the model can be justified since the special low-temperature properties are a phenomenon shared by various host-impurity compositions. In the notation of the second quantization, the model has the following ingredients: An unperturbed Hamiltonian describes the conduction electrons with wave number k and energy ϵ_k

$$H_0 = \sum_{\vec{k},\sigma} \epsilon_k c^*_{k\sigma} c_{k\sigma} \tag{6.3}$$

where $c^*_{k\sigma}$ and $c_{k\sigma}$ are the creation and annihilation operators, respectively, of the band states with quantum number k and σ. The interaction of their spins with one localized moment S originating from the impurity atoms is given by

$$H' = -J\sum_{k,k'} exp[i(k-k')\cdot R_0]\cdot[(c^*_{k'\uparrow}c_{k\uparrow} - c^*_{k'\downarrow}c_{k\downarrow})\,S_z + (c^*_{k'\uparrow}c_{k\downarrow})\,S_- + (c^*_{k'\downarrow}c_{k\uparrow})\,S_+]. \tag{6.4}$$

The possible processes that are allowed in the conduction electron - impurity scattering can directly be seen from this form. The operators in the brackets before S_z stand for the transitions where initial and final electron spin are identical and the spin of the impurity S_z is conserved. This is the case in normal potential scattering where the scatterer has no internal degree of freedom. In the treatment of Kondo, also intermediate states at the impurity are considered, and the change of spin orientation during the scattering process is allowed. That possibility is expressed by the last two terms in Eq. 6.4 containing the

impurity spin raising and lowering operators $S_\pm$. Kondo calculated transition probabilities for such single spin flip scattering as well as for double flip processes with conserved S_z corresponding to the first mentioned term, but with a spin flip from initial to an intermediate state at the impurity and a back-flip from intermediate to final state. Their values are identical up to a factor of two, and increase when the energy of the initial state approaches the Fermi energy ϵ_F. Calculating the resistivity due to these scattering channels results in a term

$$\rho_{spin} = c\rho_M[1 + (3zJ/\epsilon_F)logT] \tag{6.5}$$

with a logarithmic dependence on the temperature T that diverges when T goes to zero and the exchange constant J is negative. c is the impurity concentration, ρ_M a function of $S(S-1)$ and z the number of conduction electrons per host atom. This is the result of Kondo connecting the resistivity anomaly with the dynamical character of the spin-flip scattering.

Further theoretical analysis of the *s-d*-interaction model by Suhl and others [116, 122, 123] revealed that below a temperature T_K, a transition occurs from the high temperature state that was described by a localized moment and a separate conduction electron system to a *quasi bound state* with a lower ground state energy at $T = 0$. In the Kondo-state below T_K, the *s-d*-interaction thereafter leads to a resonant scattering of the conduction electron states at the Fermi-energy, which are crucial for the current transport at low temperatures. The conduction electrons near the impurity become spin-polarized and effectively screen its magnetic moment, so that the impurity moments appear to have vanished in the limit $T \to 0$. The temperature T_K is called the Kondo- or Abrikosov-Suhl-temperature and depends exponentially on the inverse of the exchange constant J and the electron density ρ at ϵ_F at the position of the local spin (see Eq. 6.1).

The Anderson model

Originally, this model was intended to investigate the conditions under which dilute transition metal impurities can form a magnetic state in the alloy. The most basic version of the single impurity Anderson model (SIAM) from 1961 considers only one impurity, and initially also disregards orbital degeneracy [124]. The fundamental idea is that a localized *d*-level exists on an impurity, which can be singly occupied with either spin orientation, and is in that sense degenerate. A double occupation of the *d*-state gives rise to a high Coulomb repulsion energy U between the spin-up and the spin-down electron in the same orbital. The Hamiltonian of the model in second quantization is given by

$$H = \sum_{k\sigma} \epsilon_k c_{k\sigma}^* c_{k\sigma} + \epsilon_d d_{d\sigma}^* d_{d\sigma} + U d_{d\downarrow}^* d_{d\uparrow}^* d_{d\downarrow} d_{d\uparrow} + \sum_{k\sigma} (V_{kd} c_{k\sigma}^* d_{d\sigma} + V_{kd}^* d_{d\sigma}^* c_{k\sigma}) \tag{6.6}$$

The first two terms stand for the undisturbed conduction band electrons and the *d*-impurity state, the third term introduces the correlation energy U. Fig. 6.5 shows the

density-of-states (DOS) of the two decoupled systems, i.e for $V_{kd} = 0$. The figure shows the magnetic, symmetric case, where the singly occupied state on the spin-up side is located below the Fermi-energy at ϵ_d, while a double occupation with an opposite-spin electron costs an additional energy $\epsilon_d + U$, which lies above the Fermi-level. Generally, the position of ϵ_d relative to the Fermi-level ϵ_F as well as the Coulomb energy U are free parameters of the model. The interaction between the two subsystems is then introduced by a non-vanishing V_{kd} in the last term of Eq. 6.6, which allows transitions between conduction band states and the d-state. This sort of s-d-interaction is, however, not of the exchange-type that was described in the Kondo-model, it is rather determined simply by the overlap of the different types of wave functions. The original calculation by Anderson was made in the Hartree-Fock approximation, which has turned out an inadequate approach later. As Anderson pointed out, an essential prerequisite for a local moment is that the impurity state wave function is sufficiently different from the Bloch-states of the conduction band, so that a localization can arise. This means the magnetic state of an immersed impurity with single occupation of the localized state requires a small hybridization parameter V_{kd}. In the absence of the Coulomb interaction, the hybridization causes a broadening Δ of the localized level

$$\Delta(\epsilon) = \pi \sum_k |V_{kd}|^2 \delta(\epsilon - \epsilon_k) \quad \approx \quad \pi\rho_0 |V|^2 \tag{6.7}$$

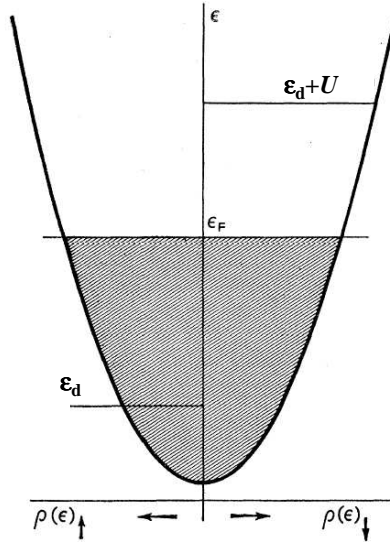

Figure 6.5: *Energy diagram corresponding to the symmetric Anderson model displaying the unperturbed DOS of the non-interacting subsystems: an s-band filled to ϵ_F and a localized d-state with the singly occupied level below and the doubly occupied above the Fermi-energy. Graphics reproduced from ref. [124].*

determined by the hybridisation energy V_{kd}. It also defines different parameter regimes of the model [12]. In the magnetic case discussed above, the ratios of the energetic distance from localized level to Fermi-energy and the level broadening indicate the different regimes. If the conditions $\frac{\epsilon_d + U - \epsilon_F}{\Delta} \sim 1$ and $\frac{\epsilon_F - \epsilon_d}{\Delta} \sim 1$ apply, charge fluctuations can occur at the impurity level, which then has non-integer occupation numbers between 0 and 2. This case is called the mixed-valence regime. Another regime is determined by $\frac{\epsilon_d + U - \epsilon_F}{\Delta} \gg 1$ and $\frac{\epsilon_F - \epsilon_d}{\Delta} \gg 1$, where charge fluctuations are suppressed. Thus, the occupation number of the localized level is very close to 1, but spin fluctuations still exist. This limit is called the Kondo-regime, where the SIAM can be shown to be equivalent to the *s-d* exchange model of Kondo [125]. It is then possible to express the effective exchange coupling parameter $J_{kk'}$ in terms of the parameters of the Anderson model:

$$J_{kk'} = V_{kd}^* V_{k'd} \left[\frac{1}{(U + \epsilon_d - \epsilon_{k'})} + \frac{1}{(\epsilon_k - \epsilon_d)} \right] \quad \approx \quad \frac{|V|^2 U}{(U + \epsilon_d - \epsilon_F)(\epsilon_d - \epsilon_F)} \qquad (6.8)$$

Near the Fermi-energy, the k-dependence is small, and the approximate, k-independent expression on the right hand side is often used in calculations. Therefore, the Anderson model is an adequate description of a Kondo-impurity system, that consists of a local moment and an antiferromagnetic exchange interaction with the conduction electrons of the host metal.

Spectral function of Kondo systems

In order to build a bridge between the theoretical models on the one hand, and the data gained with modern experimental methods on the other hand, single-particle spectral functions may be calculated representing the properties of the system as probed by the measurement process. In photoemission spectroscopy (PES) as well as in tunnelling spectroscopy (STS), an electron is removed from the system and provides information on the state left behind with $n - 1$ electrons. Such PES experiments have mainly been carried out investigating rare-earth compound materials, preferably containing Cerium [126]. In valence band photoemission experiments, the cross section of the N_f-fold degenerate $3d$ or $4f$ impurity levels dominate the photoelectron signal, and therefore, theory has to calculate the spectral function for electron removal from the localized level. Gunnarsson and Schönhammer have developed a variational approach for the ground state of the N-fold degenerate Anderson model that allowed extensive comparison with experiment [127]. Further theoretical work has become necessary after the first experiments on single impurity spectroscopy with the STM showed results that were qualitatively different. While in the PES signal, the Kondo-resonance is seen as a *peak* at the Fermi-energy, in STS spectra it appears as a *dip* in the differential conductance. The STS results suggest that the electron removal via tunnelling to the tip does not proceed mainly from the localized *f*- or *d*-state as in a PES experiment, but from the *s-p*-derived delocalized states of the host electrons. It follows that the spectral function of electron removal from the *host matrix electrons* is the adequate quantity to be compared with the STS results. The modification
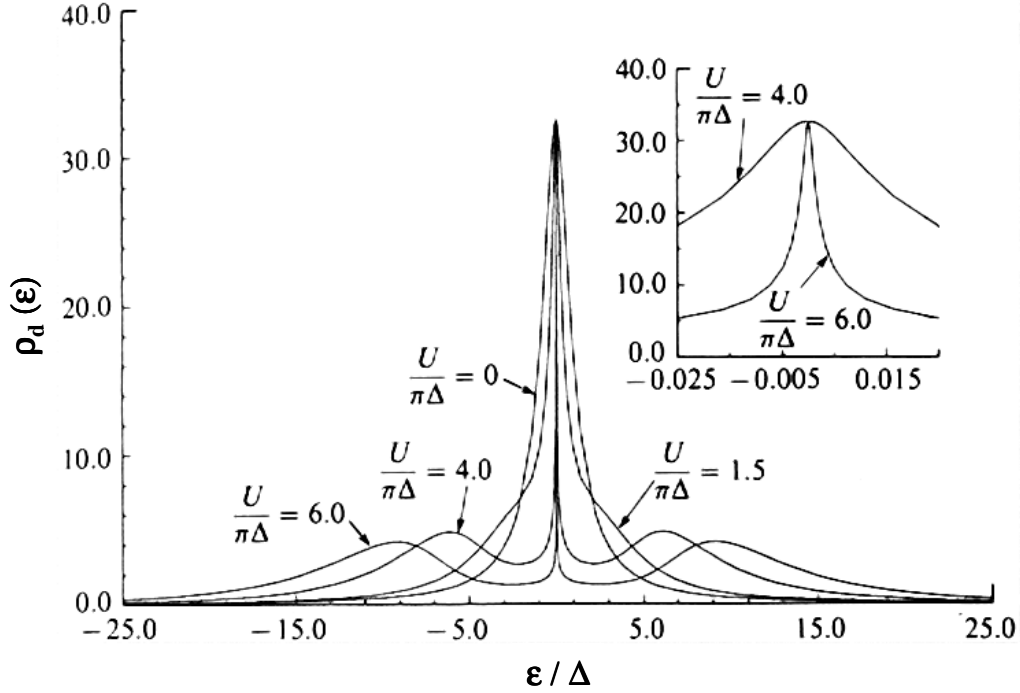
Figure 6.6: *Calculated impurity level single-particle spectral function $\rho_d(\epsilon)$ for different hybridization strenghts. The energy axis is renormalized with the broadening Δ and indicates the sharp many body resonance at the Fermi-energy $\epsilon = 0$. Graphics reproduced from ref. [12].*

in the *DOS* of the host electrons with all the many-body effects induced by the impurity is then calculated with the help of the localized-level Green's function [128, 129, 130]. In a reasonable limit for a real tunnelling experiment, the direct tunnelling into the localized state is neglected. The anti-resonance in the differential conductance then is the result of interference between electrons tunnelling directly into band states and those that additionally scatter resonantly at the magnetic impurity. The interference gives rise to spectral line shapes more complicated than simple Lorentzians. The zero bias feature observed in STS is the result of a Fano-type resonance [131] that is described by Eq. 6.10 in the limit $T \ll T_K$ [128], which we will use in the following section to interpret our results.

6.3 Experimental results

6.3.1 Preparation and measurement

The experiments were performed using the liquid ^{4}He-cooled low-temperature UHV-STM operating at a temperature below 8 K. The base pressure of the UHV-system was better

than $1 \cdot 10^{-10}$ mbar with the cryostat at room temperature. The very good UHV conditions allow to keep the prepared films in the chamber at RT for several days without much contamination. To keep the surface clean after the sample has been cooled down, though, it was necessary to leave the crystal in the microscope while the whole cryo system slowly warmed up. Removing the cold crystal from the cryostat did strongly contaminate the surface, so that further investigation was not possible. Tunnelling tips were electrochemically etched from tungsten wire and, after transfer to UHV, annealed and sputter-cleaned with 4 keV Ar^+ ions. While executing the experiments, the performance of the tip was tuned by controlled tip-sample contact and voltage pulses.

The thin film sample preparation was preceeded by sputtering and annealing cycles of the Cu(111) single crystal substrate in the preparation chamber at a base pressure of $5 \cdot 10^{-11}$ mbar. To avoid contamination, the clean crystal was *in situ* removed and locked away in the microscope chamber while in the preparation chamber the Co and Cu e-beam evaporators were carefully outgassed for several hours. Then the Cu(111) substrate was put back in and kept at room temperature, while a 5 nm thick Cu film was deposited at a rate of 0.04 ML/s. Depending on the Co concentration desired, the second evaporator simultaneously added a percentage of 0.1 to 0.4 of Co atoms to the growing film. This preparation procedure was identical for every film that was grown, only the amount and the distribution of the Co impurities was varied from sample to sample. One film was alloyed homogeneously with 0.1 atomic percent of Co (2002-054), while two others only received 0.4 and 0.3 percent Co at the end of the growth process into the topmost Cu layers (2002-067 and 2003-003). In very few cases, defects also might be due to non-Cobalt residual impurities that cannot be completely omitted in thin film preparation, but the purity of the base materials (Cu: 99.999 %; Co: 99.99 %) indicates that the percentage of non-Co defects is determined by the purity of the Cu and thus should lie at about 1% at the given Co concentrations. After the preparation procedure, the sample was transferred to the STM chamber and then cooled to low temperatures in the cryogenic STM.

All measurements were done with the tip stabilized in constant current mode. The spectroscopic data were acquired according to the following scheme: while recording a constant current topography image, an $I(U)$ curve was additionaly taken at every point with interrupted feedback loop. Further data processing as described in Section 2.4.1 generates a complete set of dI/dU spectra as a function of the lateral coordinates with a spatial resolution of atomic dimension.

6.3.2   Classification of defect patterns

A typical constant current image of the dilute Co-Cu films is shown in Fig. 6.7. Terrasses and islands of sixfold symmetry with rounded corners are seen as a result of the RT deposition process. On the flat areas, standing wave patterns of the 2D surface state electrons at the (111) surface are visible as pm-scale modulations in tip height. Strong scattering is observed at steps or island edges, but also at several atomic defects in the
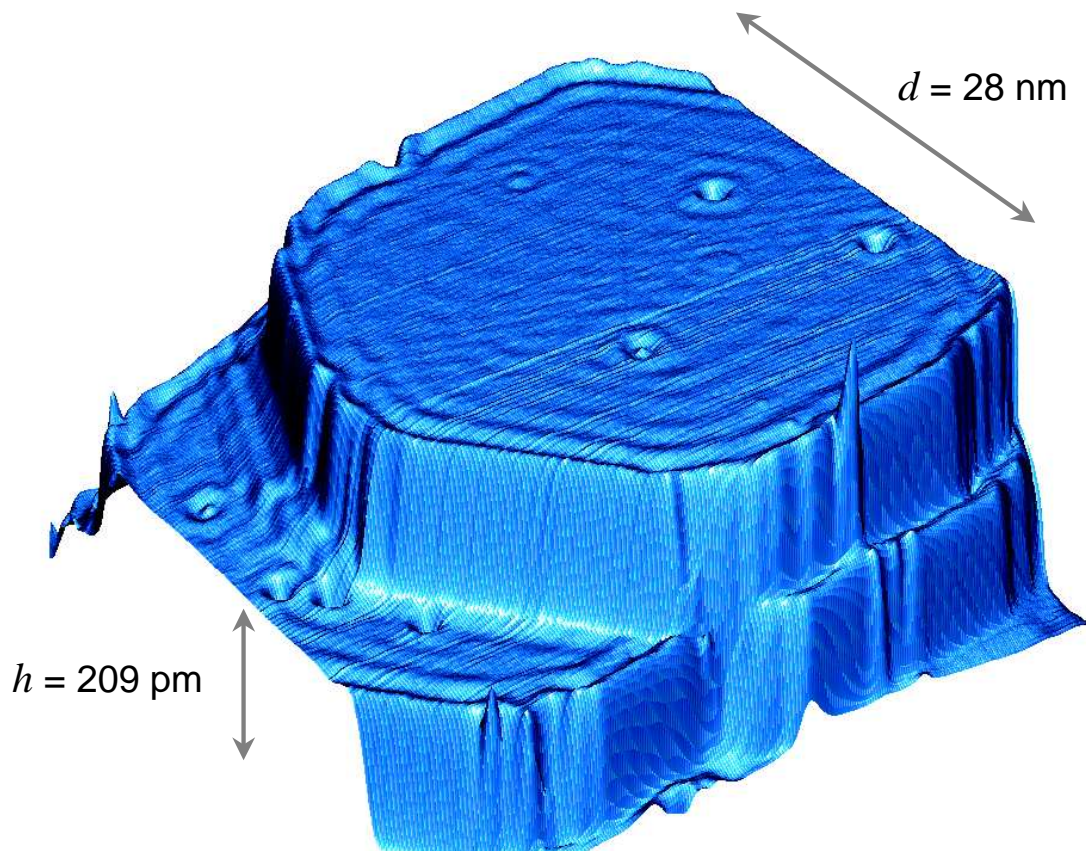
Figure 6.7: *Constant current image of a RT-grown Cu film with Co-alloyed surface in a 3D view (raw data from the microscope at $U_B = 0.3$ V, $I_T = 0.6$ nA). On the terraces and islands, standing wave patterns of the surface state electrons are visible together with a number of atomic defects located in the surface and subsurface crystal layers.*

terraces. From the height scale it is clear that there are no Co adsorbates present on the surface, which would show up as 80 pm high bumps in constant current mode [107]. Thus, the atomic scatterers seen here must be located *in* or *below* the crystal surface, not on top of it. These spherical wave patterns thus indicate the positions of the Co impurities within the Cu matrix.

Near-surface Co impurities

Fig. 6.7 does also show that there is more than only one single type of defect pattern present on the surface. In Fig. 6.8, four characteristic patterns of Co defects are extracted, that are found on these surfaces. Cross sections of the constant current images are shown
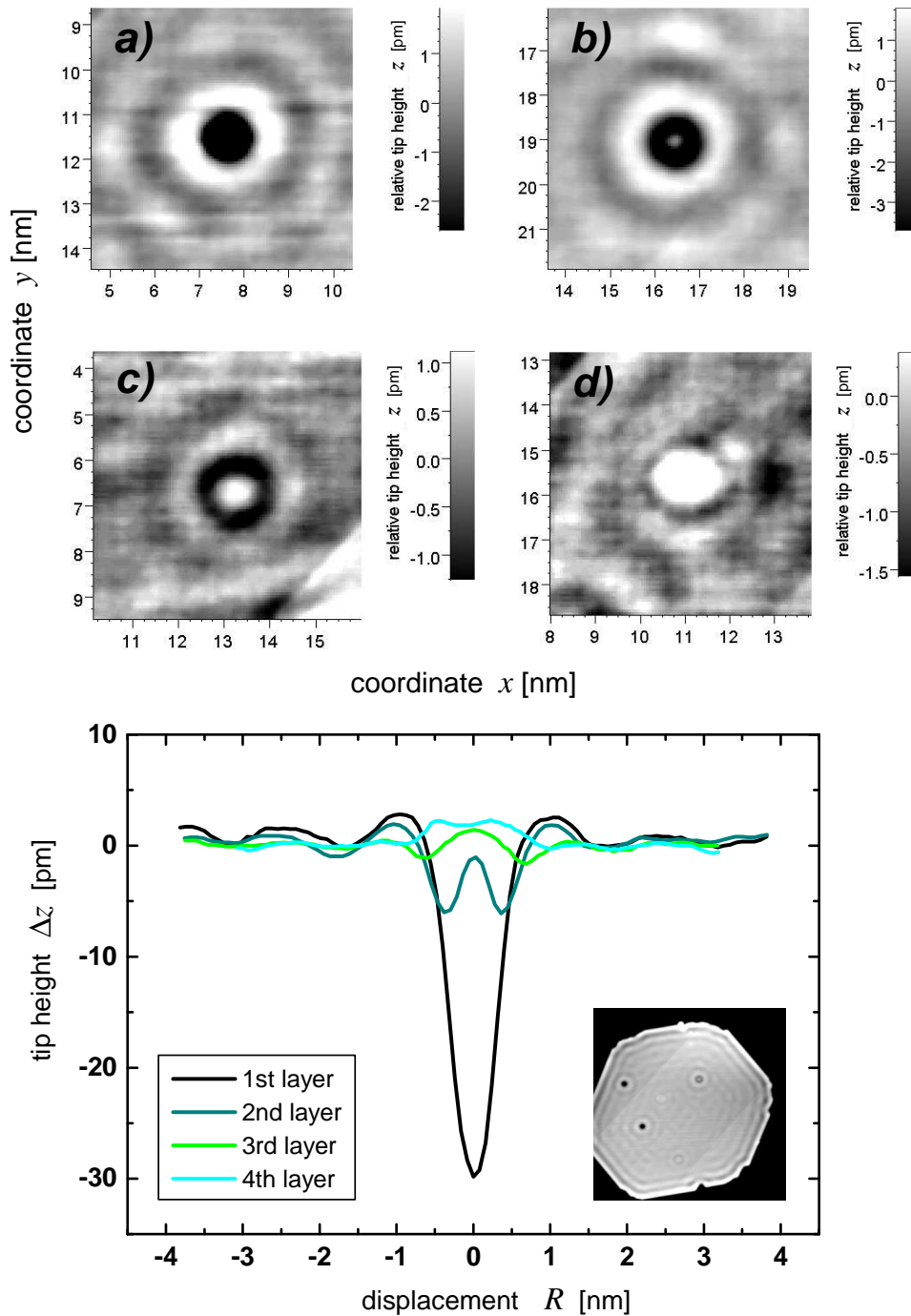
Figure 6.8: *Four typical defect patterns in constant current mode ($U_B = 0.3$ V, $I_T = 0.6$ nA) of near-surface Co impurities in Cu(111). Corresponding cross sections are shown below. The vertical positions of the impurities are assigned as follows: a) surface layer; b) 2nd layer; c) 3rd layer; d) 4th or 5th layer. The defects exemplary displayed here are from the Cu island investigated in Chapter 5.*

below. From the sample preparation, it is expected to find the Co atoms only in the topmost layers of the film. The cross sections clearly indicate a certain tendency of the tip height at the centre of the defect atom from one defect pattern to the other. The black line stands for defect *a)* that produces a relatively deep depression in constant current mode with an amplitude of $\Delta z(0) = -30$ pm. This is understood as the suppression of the surface state $LDOS$ at the location of the impurity atom (see Discussion), and therefore must correspond to Co atoms embedded in the surface layer of Cu(111). The spectroscopic results discussed in the following sections corroborate this assignment. In contrast to that, the other three constant current section plots in Fig. 6.8 show defect patterns that have local maxima at the centre. The pattern *b)* that still has the shape of an overall slight depression is also seen to strongly produce Friedel-oscillations in the surface state electron density similar to that of the top layer impurity. In case *c)*, the relative tip height at the defect centre $\Delta z(0)$ is already a global maximum while the surface state Friedel-oscillations in the vicinity are less intense than in pattern *b)*. From this comparison, pattern *b)* is assigned to a Co in the second crystal layer and pattern *c)* to one in layer three. The remaining case *d)* is only clearly distinct from case *c)* around the centre, and it also represents a frequently found contrast on these alloy surfaces. It should therefore be sufficient to suspect *d)* to be a Co atom in the fourth or fifth layer. The impact of this scatterer on the surface state obviously is close to zero, and compared with the vertical surface state electron density in Fig. 6.1, this should also be expected for a scatterer located in this depth. Finally, we must recognize that the the scattering of the surface state at these surface and subsurface defect atoms produces a much stronger amplitude in constant current imaging than was predicted by a theoretical treatment of surface state scattering at buried impurities [132].

Deep Co impurities buried in the bulk

Apart from these typical surface defects, there were also a number of other contrasts present in constant current images when the Co atoms were not only deposited surface-near but homogeneously added to all of the Cu film layers. In this case, additional ring-like structures were observed, which obviously stem from atomic defects that are buried deep below the surface layer in the bulk. The presence of such bulk defects can create clearly visible patterns at the surface, as is shown in Fig. 6.9. Unlike in the case of near-surface impurities, the surface state electrons can propagate freely and remain unaffected by any atomic scatterer. The buried atoms responsible for the differently sized ring-like oscillation patterns that are seen in Fig. 6.9 must therefore lie well below the vertical extension of the surface state. The different radii of the rings indicate different depths of the individual scatterers, where the relative intensities of the ring patterns favor the assumption of a larger depth d with increasing radius R of the pattern. The wavelength component detected at the surface which dominates these ring patterns corresponds to $k_{\parallel} \simeq 0.6$ Å^{-1}. This is about a factor of three larger than the Fermi-wave vector of the surface state electrons.
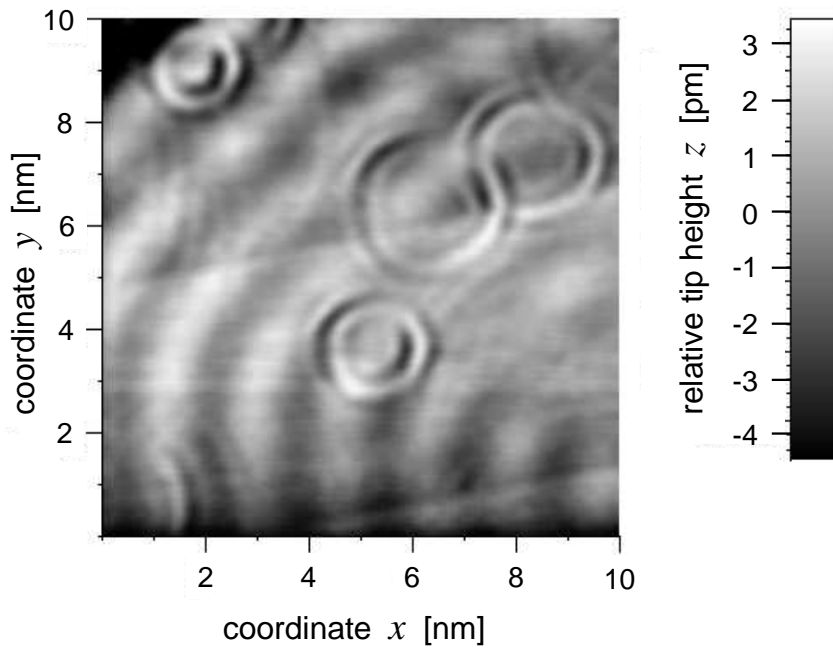
Figure 6.9: *Constant current image of a homogeneous dilute Co-Cu alloy film ($U_B = -0.08$ V, $I_T = 1.0$ nA). The surface state can propagate without being scattered by atomic defects. The ring-shaped patterns originate from buried impurities that scatter bulk electronic states which interfere constructively at the surface.*
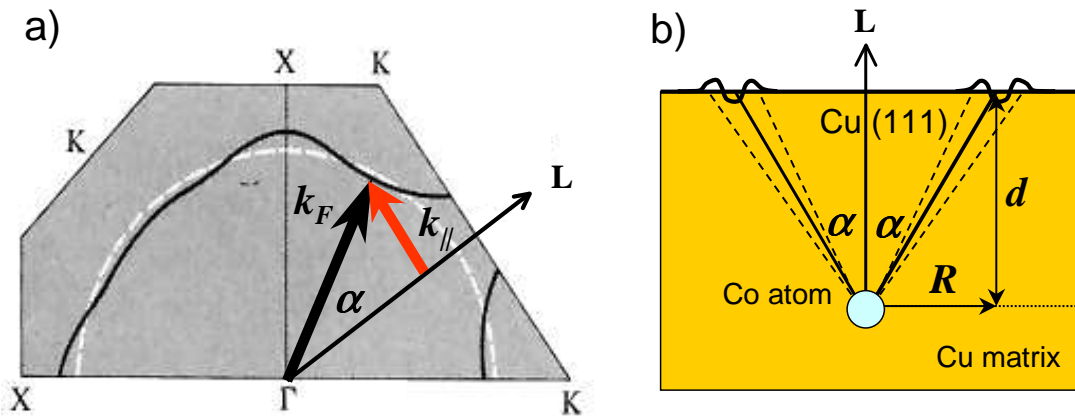

Figure 6.10: *a) Section across the first Brillouin zone showing the bulk states contributing to the ring-shaped interference patterns. The parallel component determined from experiment and the Fermi-surface indicate the contributing bulk wave vectors and their angle α to the (111) direction. b) Real space sketch of the directions under which interference effects originating from bulk atomic defects can occur at the surface.*

Therefore, the conclusion from these observations is that the ring-like structures originate from scattering of bulk state electrons at subsurface Co defects. Obviously, only states propagating at a certain angle α from impurity to surface can interfere with a sufficient amplitude, which must be due to the special properties of the bulk band structure. A 2D-sketch of the bulk states that contribute to the ring patterns according to our determination of $k_\parallel$ is shown in Fig. 6.10 a). At first glance, these bulk states are characterized by a minimum of $|\vec{k_F}|$ in this region. Here, $\partial|\vec{k_F}|/\partial\alpha$ is zero and the curvature positive. The mechanism leading to the observed oscillation patterns is the coherent superposition of electron waves, and formation of a standing wave between tip and atomic scatterer. A high amplitude of bulk states at the surface can arise, when states at E_F with differing orientation of $\vec{k_F}$ propagate in the same direction. Such an electron focussing effect is possible in the concave regions of the Fermi-surface, that have a positive curvature [133]. Since the bulk electron group velocity $\vec{v_{gr}} = \frac{1}{\hbar} \, grad_{\vec{k}} \, E(\vec{k})|_{E_F}$ is oriented normal to the Fermi-surface, it becomes clear from Fig. 6.10 that the bulk state amplitude is especially high around an angle α to the surface normal. To rigorously verify the contribution of the sketched states according to the mechanism proposed here, a scattering problem considering the details of the Cu band structure must be solved. However, a simplified model considering the shape of the Fermi-surface only to second order for a limited set of wave vectors might give first information on the curvature of the Fermi-surface around this particular extremum.

For a rough estimate of the depths d, the measured component $k_\parallel$ can be matched to the Fermi-surface as shown in the Fig. 6.10, which delivers an angle α of about 25 to 30°. From the different radii R of the rings, and this angle under which the bulk electrons propagate towards the (111) surface, the depth d at which the impurities lie can be calculated by

$$tan \, \alpha = \frac{R}{d}. \tag{6.9}$$

The radii which lie between 0.8 nm and 1.4 nm, approximately, then indicate impurity depths between 1.4 nm and 2.4 nm for the four most prominent rings in Fig. 6.9. These correspond to layers 7 to 12 below the surface, which is in accordance with the conclusion that the defects must lie below the fifth layer.

6.3.3 Spectroscopy of surface layer Co impurities

Using the spectroscopic mode, single near-surface defects that have been located in the constant current mode and were imaged and simultaneously characterized by spatially resolved STS. The constant current trace of such a scan is displayed in part *c)* of Fig. 6.11. It exhibits four embedded atomic impurities, three of which have distinct appearances, corresponding to three different depths below the surface. The two identical impurities, located to the upper left and to the lower right, are identified as surface layer Co atoms according to the classification made in the preceeding paragraph. The spectra taken at
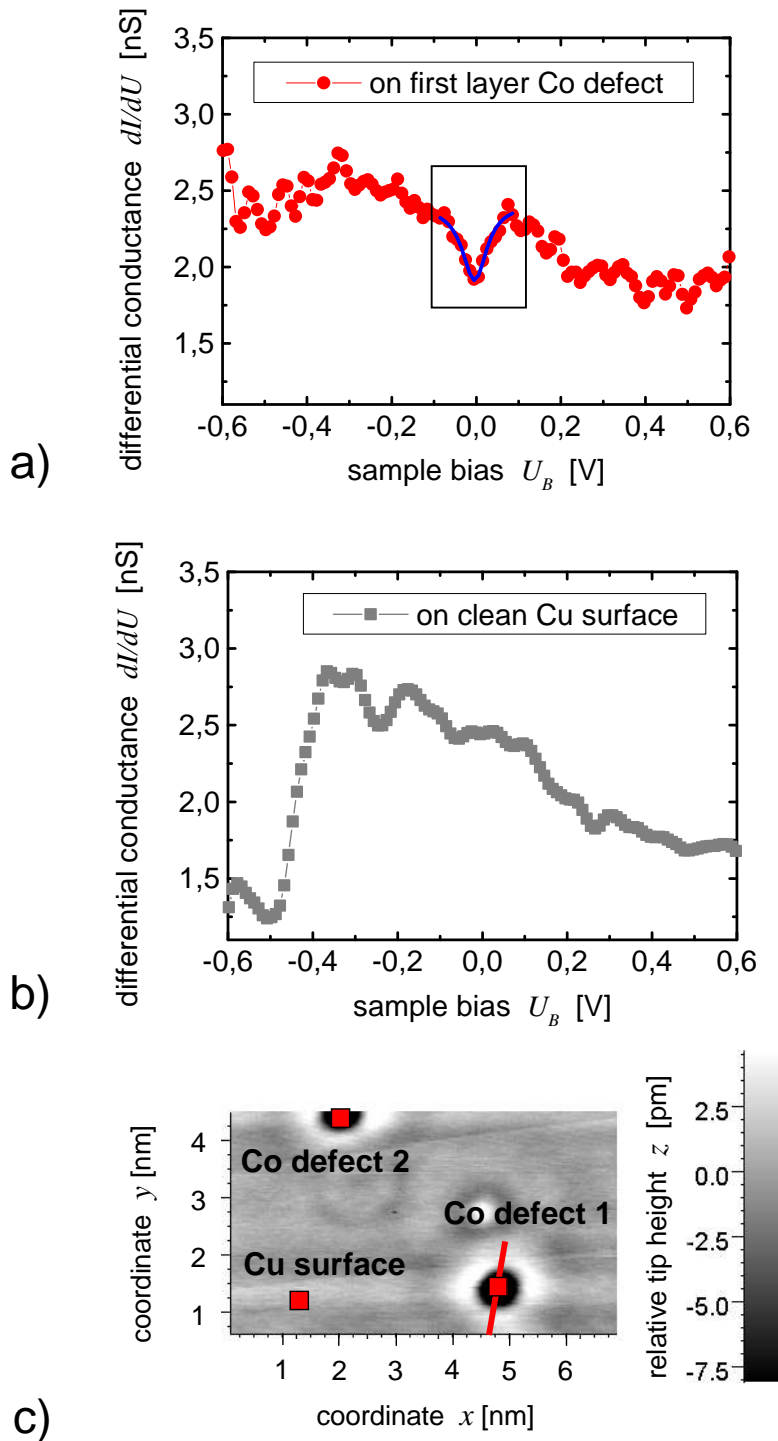
Figure 6.11: *Spatially resolved tunnelling spectroscopy of surface-layer Co defect atoms in Cu(111) (Setpoint: $U_B = 0.5$ V, $I_T = 1.0$ nA). In a), the averaged dI/dU spectrum of defects 1 and 2 shows a dip around zero bias. The surface state which is present on the clean surface shown in b) is absent in the defect spectra. The positions corresponding to the spectra are indicated by the squares in c).*

both of these impurity positions are averaged and plotted in *a)*. They show a *dI/dU* spectrum markedly different from that taken on the plain Cu surface indicated by *b)*. One single *dI/dU* spectrum represents a sum of 49 single *I(U)* spectra that were averaged over an area of $(1.9\text{Å})^2$ at each impurity location on the one hand, and on a clean surface spot on the other hand, marked by the squares in *c)*. The differential conductance was then gained via differentiation according to the procedure described in Section 2.4.1.

The plain-Cu spectrum was taken about 40 Å apart and therefore shows some variation with sample voltage due to potential scattering of the surface state at the defects. In the spectra of the surface defects, the sharp onset of the surface state that is present at -440 mV in *b)* has vanished, and instead a spectral feature around zero bias is observed as a dip in the differential conductance. This is the typical signature of the Kondo-resonance as it previously has been observed and interpreted in the case of adsorbate systems. It provides new evidence that the characteristic dip that was reported for Co adsorbates also appears in the embedded-atom geometry. The dip is found to be much broader than in the case of adsorbates. As was already mentioned earlier, we can therefore safely assign the corresponding 30 pm depression in the constant current image to Co impurities embedded in the surface layer of Cu(111).

Determination of the Kondo-temperature

In theoretical studies that model the Kondo-effect in STS, several authors have worked out expressions for the zero-bias feature using the single-impurity Anderson-model [134, 128, 129]. They agree that the correct description of the local conductivity is given by a generalization of an interference effect first studied by Fano [131]. While the extensive work of Plihal and Gadzuk is limited to temperatures around and above the Kondo-temperature, Ujsaghy *et al.* claim that their approximate scheme is valid in the limit $T \ll T_K$. For the low temperature case, they deduced Fano's function as the correction $\Delta\rho$ to a jellium *LDOS* ρ_0 and calculated its variation as a function of tip position R. This function is given by

$$\rho_0 + \Delta\rho(U, R) = c + a(R)\frac{q(R)^2 - 1 + 2q(R)\epsilon(U)}{\epsilon^2(U) + 1} \quad \propto \frac{dI}{dU}(U, R) \qquad (6.10)$$

and will be used in the following to analyze the impurity spectra at $r = 0$. The bias dependence is contained in $\epsilon(U) = (eU + \epsilon_K)/k_B T_K$ with ϵ_K the offset of the resonance from the Fermi-energy and T_K the Kondo-temperature of the specific system. The quantity q is Fano's asymmetry parameter of the spectral line shape, which can lie between 0 and ∞. It is proportional to the quotient of the transition matrix elements t_i for tunnelling to the localized impurity state and t_s describing tunnelling directly to the substrate continuum states [131, 129].

The Kondo-temperature can be determined as a parameter from the fit of Eq. 6.10 to the experimental curve. The energy range in which the fit was performed comprised the

symmetric interval [-90,+90] meV around the Fermi-level. Two data sets were considered, one being the identical data shown in Fig. 6.11, and the other with the average slope of the spectrum (-0.9 nS/V) subtracted. Which one of these two data sets best represents the real properties of the Kondo-system is difficult to judge. *Ideally*, a feature in STS lying at zero bias should not need a background subtraction because of the symmetry around E_F when particle-hole symmetry is valid. Yet, it is possible that the tip DOS influences the tunnelling matrix elements, which can be corrected approximately by a slope substraction. Therefore, the two sets can be regarded as limiting cases, where the correct parameters will lie within the boundaries given by these two fit results. The best fits to the spectra are plotted in Fig. 6.12 and in both cases they yield a half-width of the nearly symmetric dip of $k_B T_K = 35 \pm 3$ meV (HWHM). The slope substraction only affects the asymmetry
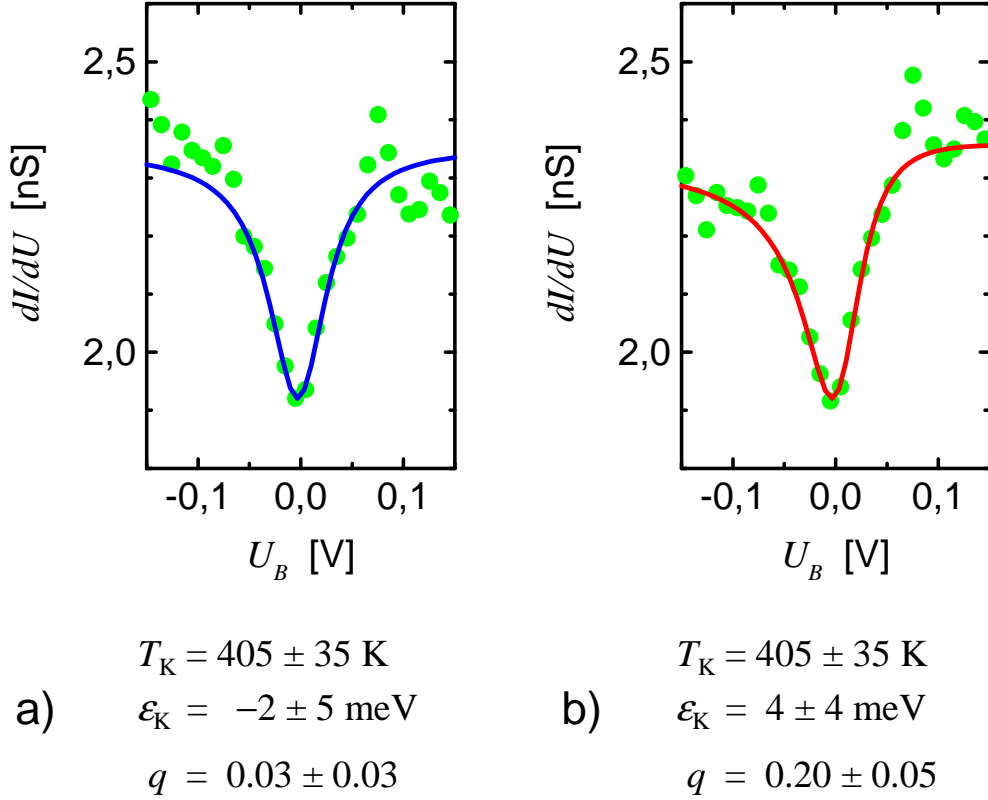
$$
\begin{array}{ll}
& T_K = 405 \pm 35 \text{ K} \\
\text{a)} & \varepsilon_K = -2 \pm 5 \text{ meV} \\
& q = 0.03 \pm 0.03
\end{array}
\qquad
\begin{array}{ll}
& T_K = 405 \pm 35 \text{ K} \\
\text{b)} & \varepsilon_K = 4 \pm 4 \text{ meV} \\
& q = 0.20 \pm 0.05
\end{array}
$$

Figure 6.12: *Fit of Eq. 6.10 to the experimental dI/dU characteristics of embedded Co atoms in Cu(111). The Kondo-feature is very broad, corresponding to a T_K of $\sim$ 405 K. In a) the fit to the original data, a nearly symmetric antiresonance, results in a parameter q of 0.03 and a slightly negative ϵ_K. In b) a linear background with a slope of -0.9 nS/V has been subtracted before fitting, which leads to a q-value of 0.2 and a slightly positive ϵ_K.*
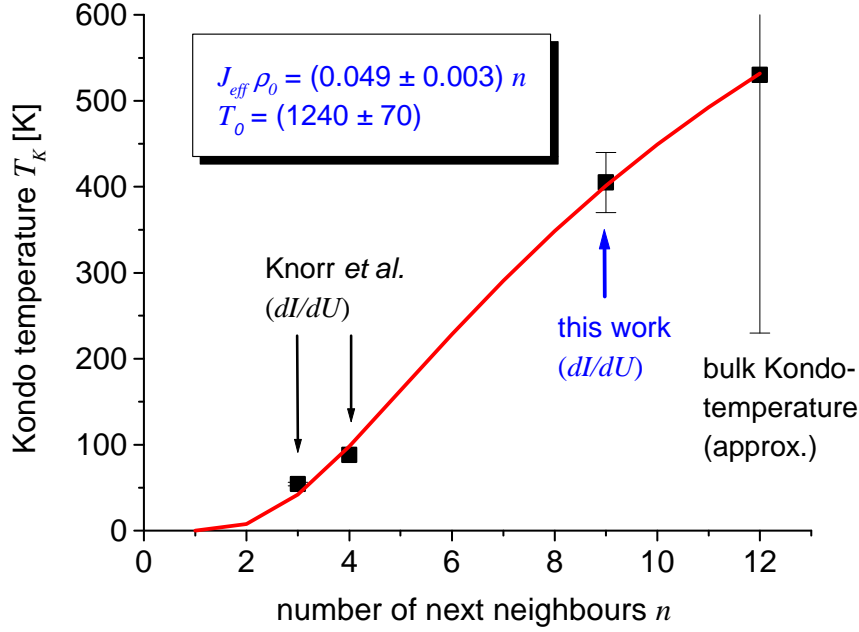
Figure 6.13: *Fit of T_K according to Eq. 6.1 to the experimental Kondo-temperature data. The simple scaling of $J_{eff}\rho_0 \propto n$, the number of nearest-neighbours [107], is very well followed by the present data points.*

parameter q and the offset of the resonance from E_F, which is found to be $\epsilon_K = -2 \pm 5$ meV in the one case and $\epsilon_K = 4 \pm 4$ in the other. The half-width corresponds to a Kondo-temperature of $T_K = 405 \pm 35$ K, which nearly is a factor of 8 larger than the T_K of ~ 54 K measured with STS in the case of adatoms [106, 107]. The comparably high statistical error in our determination of T_K has its origin in the relatively low energy resolution of the measurement for the sake of gaining good spatial resolution within a short acquisition time.

Qualitatively, this increase of the Kondo-temperature for an embedded Co impurity was expected according to Equation 6.1. Together with the adsorbate Kondo-temperatures reported by Knorr *et al.*, we can check whether the scaling $J_{eff}\rho_0 \propto n$ proposed by these authors still is an appropriate assumption when the Kondo-temperature of embedded Co is included. The number of nearest-neighbour matrix atoms for the case of an embedded Co in Cu(111) is $n = 9$. This gives us a relatively accurate value of a highly coordinated impurity, in contrast to the large uncertainty attributed to the bulk T_K. A fit of Eq. 6.1 to the available experimental data is shown in Fig. 6.13, taking into account $n = 3, 4, 9, 12$. Here, $T_K(12) = 530K$ is displayed, representing the value for the bulk T_K according to Tournier and Blandin's estimate [118]. The figure shows that a convincing fit of this function to all of the data points can be found. The experimental value for T_K determined in this work thus provides additional support for the scaling relation proposed by Knorr

and coworkers. Within that model, it also provides strong support that T_K^{bulk}, the bulk
Kondo-temperature of dilute Co in Cu, lies around 530 K. This can be asserted on the
basis of the limited error of $T_K(9)$ determined here by STS.

Spatial extension of the Kondo-dip

In the spectroscopic data acquisition mode, the complete information on the surface area
within the chosen bias voltage range is collected, contained in the $I(U)$ curves. Therefore,
an arbitrary cross section may be placed in that surface area, along which a spatially
resolved sequence of tunnelling spectra can be extracted. By differentiating these spectra,
a position-dependent differential conductivity plot can be generated and displayed in a grey
scale representation. Such dI/dU section plots provide insight into the spatial variation
of the $LDOS$, which is particularly interesting in the vicinity of the magnetic impurity.
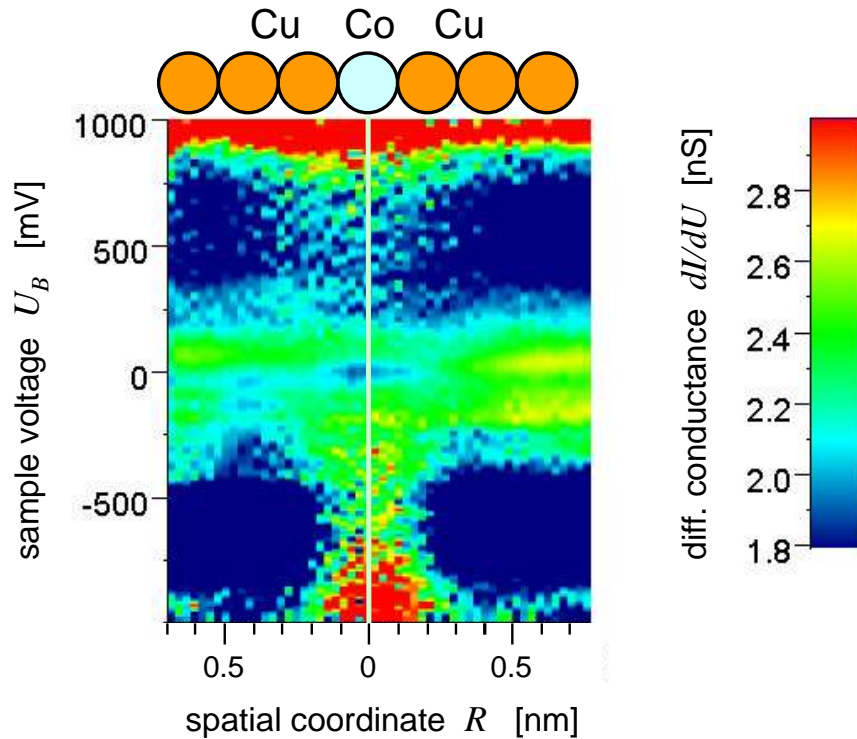The spatial extension of the zero-bias Kondo-resonance feature found for the embedded

Figure 6.14: *Differential conductance dI/dU section plot across a surface layer Co impu-*
rity in the Cu(111) surface. The Kondo-dip is resolved as the dark spot in the centre at
zero bias. Above $U_B \sim -400$ meV the surface state contributes to the tunnelling current.
The bright area at large negative and large positive voltages indicates the region around
the impurity site where enhanced tunnelling into bulk states occurs.

Co impurity thus may be visualized. According to the result of Ujsaghy *et al.* and others [128, 129], the spatial variation of the resonance line shape should be determined by k_F, the Fermi-wave vector of the continuum states that participate in the Kondo-resonance.

Fig. 6.14 shows a dI/dU spectra section across the Co defect 1 along the line indicated in Fig. 6.11. The plot represents an average over a seven pixel wide strip along the section line with a subsequently applied 5x5 median fiter. The tunnelling into the surface state channel is visible as the mostly green region above $U_B \sim -400$ meV, while below the blue colour corresponds to tunnelling only into bulk states. The observation of strong surface state electron scattering that has been made in the constant current images is also visible in this plot. The surface state *LDOS* clearly goes down in the vicinity of the defect atom. The most obvious spatial inhomogeneity seen in this figure is that of a strong differential conductance signal at the location of the Co atom at negative bias. Since it is evident from the constant current image that the tip moves down at the Co location, the increase of the signal is due to enhanced overlap with the bulk states. At positive bias values, the overall signal is weaker and the spatial variation is much less pronounced, which may be be explained by the characteristics of the tunnelling tip.

Focusing on the zero-bias line, the dip-like Kondo-feature is also clearly visible as the dark blue region centered at $r = 0$ nm. It is notable that the spatial extension of the Kondo-dip is comparable with that of the enhanced bulk state tunnelling at higher negative voltages. Both extend over a radius of about 2 or 3 Å, while the shape of the dI/dU spectra around E_F obviously changes when placing the tip off-center with respect to the Co impurity. From Fig. 6.14 it thus appears that the Kondo-feature, the pronounced dip in the spectra, is present only up to a radial distance of less than 3 Å. This corresponds to about 1.5 Cu lattice constants, which is symbolized by the hard sphere model shown in the figure. This result is clearly different from the behaviour reported for adsorbate Kondo-systems. There, the Kondo-feature remained present in the tunnelling spectra up to a lateral tip distance of about 10 Å [135, 107].

In order to investigate the spatial dependence of the Kondo-feature more accurately, we assume for simplicity that the impurity system roughly has rotational symmetry. To gain best-possible data quality, the spectra can then be averaged circularly around the impurity centre, which was done and is shown in Fig. 6.15. Four rings were evaluated at average distances of $R =$1.8 Å, 3.2 Å, 4.6 Å and 6.5 Å, and the averaged curves are compared to the central dip on the Co impurity around E_F. As Fig. 6.15 shows, the form of the dI/dU-spectra near zero bias develop with the lateral tip-impurity distance R from a nearly symmetric dip to an asymmetric peak about two lattice spacings apart. The black lines in a) show individual fits of Eq. 6.10 that were made to the four data sets. Interestingly, with all the parameters left unconstrained, the fits deliver Kondo-temperatures of around 400 K at *all* of the radial distances considered here. If a larger bias range is considered, which is shown in Fig. 6.15 b), additional information is gained on the tunnelling channels involved. The form of the spectra at -400 mV indicates that already at $R \sim 3$ Å tunnelling into surface states gives a distinct contribution to the signal. At $R \sim 6$ Å, the conductance has
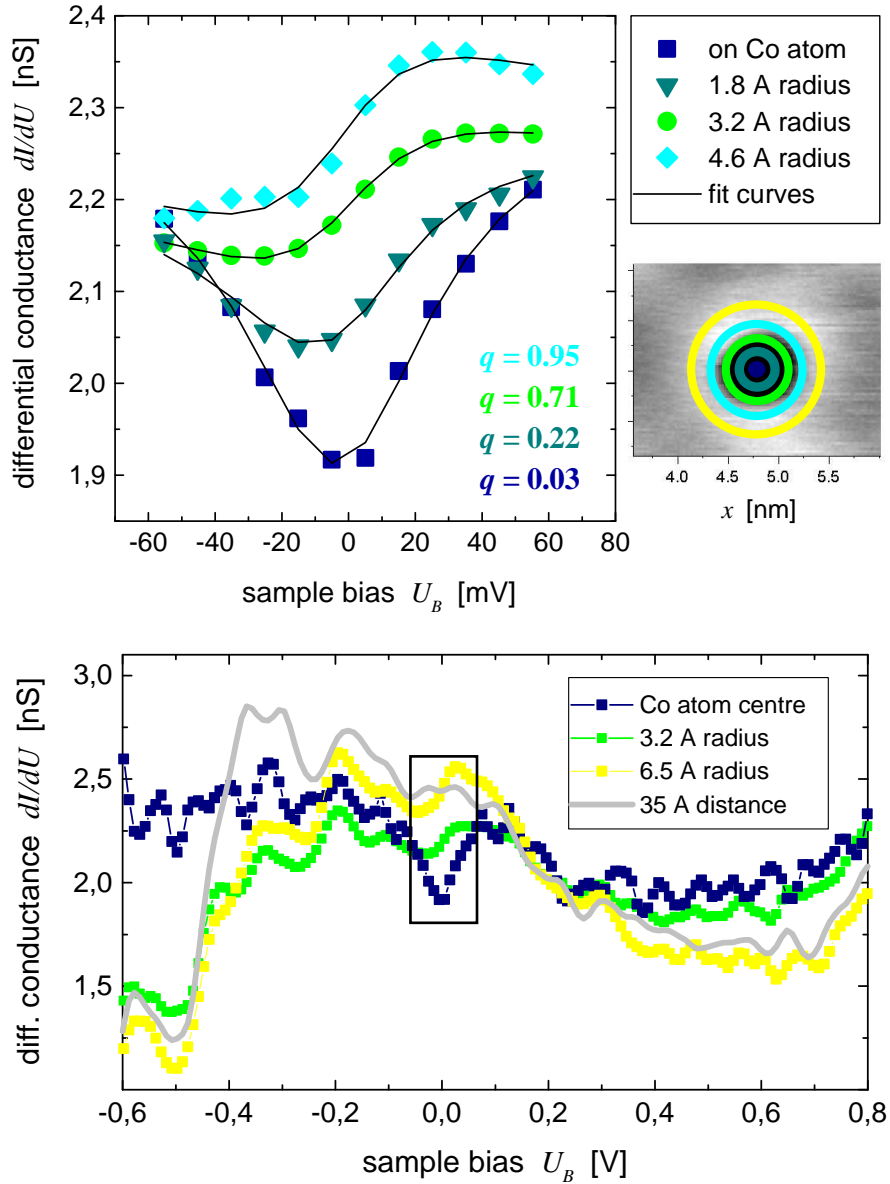
Figure 6.15: *Comparison of the dI/dU spectra at different radial distances from the Co impurity. The line shape develops from the central antiresonance to an asymmetric shape two lattice spacings apart. In a) Fano-lineshapes are fitted to the spectra around E_F which deliver an increasing asymmetry parameter q with distance R from the centre. In b) the onset of the surface state around $U_B \sim -400$ meV becomes visible already at distances of $R > 3$ Å.*
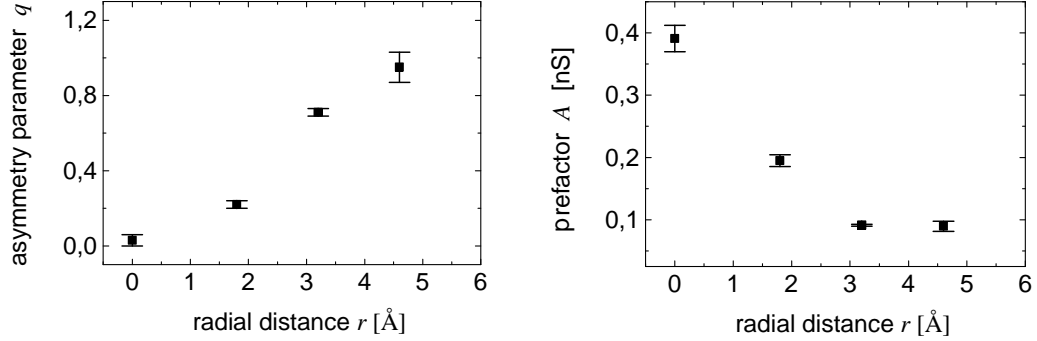
Figure 6.16: *The radial dependence of the shape parameters determined by the fits in Fig. 6.15 using fixed energy parameters as determined in Fig. 6.12.*

increased and shows a small peak somewhat above E_F. It is also evident from Fig. 6.15 b) that wiggles in the spectra appear consistently at particular energies, while the overall shape of the spectrum varies. The characteristic variation with R consists of the gradual disappearance of the surface state onset together with the appearance of the zero-bias Kondo-dip directly above the impurity. The $R = 6.5$ Å curve is already very close to the Cu reference spectrum taken 35 Å apart. This suggests that surface state tunnelling starts to dominate the spectra when the tip is as little as three to six Ångstrøms away from the Co impurity.

For the fits shown in Fig. 6.15 a), the energy scale parameters $T_K = 405$ K and $\epsilon_K = -2$ meV were set as fixed, and only the asymmetry parameter $q(r)$ and the amplitude $A(r)$ were allowed to vary as a function of radial distance. The results of the fits are shown in Fig. 6.16. These plots indicate a monotonous increase of the asymmetry parameter q and an asymptotic decrease of the amplitude parameter A with the radius r. The fact that the dI/dU spectra shown in Fig. 6.15 can be fitted with identical T_K and ϵ_K suggests that also at tip distances of $R \geq 3$ Å where the characteristic dip in the spectra has already vanished, a coherent impurity-substrate Kondo-state is probed.

6.3.4 Spectroscopy of subsurface impurities

The presence of Co atoms in different subsurface layers provided the possibility to also probe shallow impurities below the surface by STS. Since these defects are clearly visible in constant current mode, one should also expect a certain fingerprint of the defect in STS. In the constant current image in Fig. 6.17 e), three markers indicate subsurface defects which we expect to be Co by our film preparation, and the position of a reference spectrum for comparison. The squares again correspond to a sum of 49 single $I(U)$ spectra that were averaged over an area of $(1.9\text{Å})^2$. The lines indicate the direction along which spatially resolved spectra sections were analyzed.
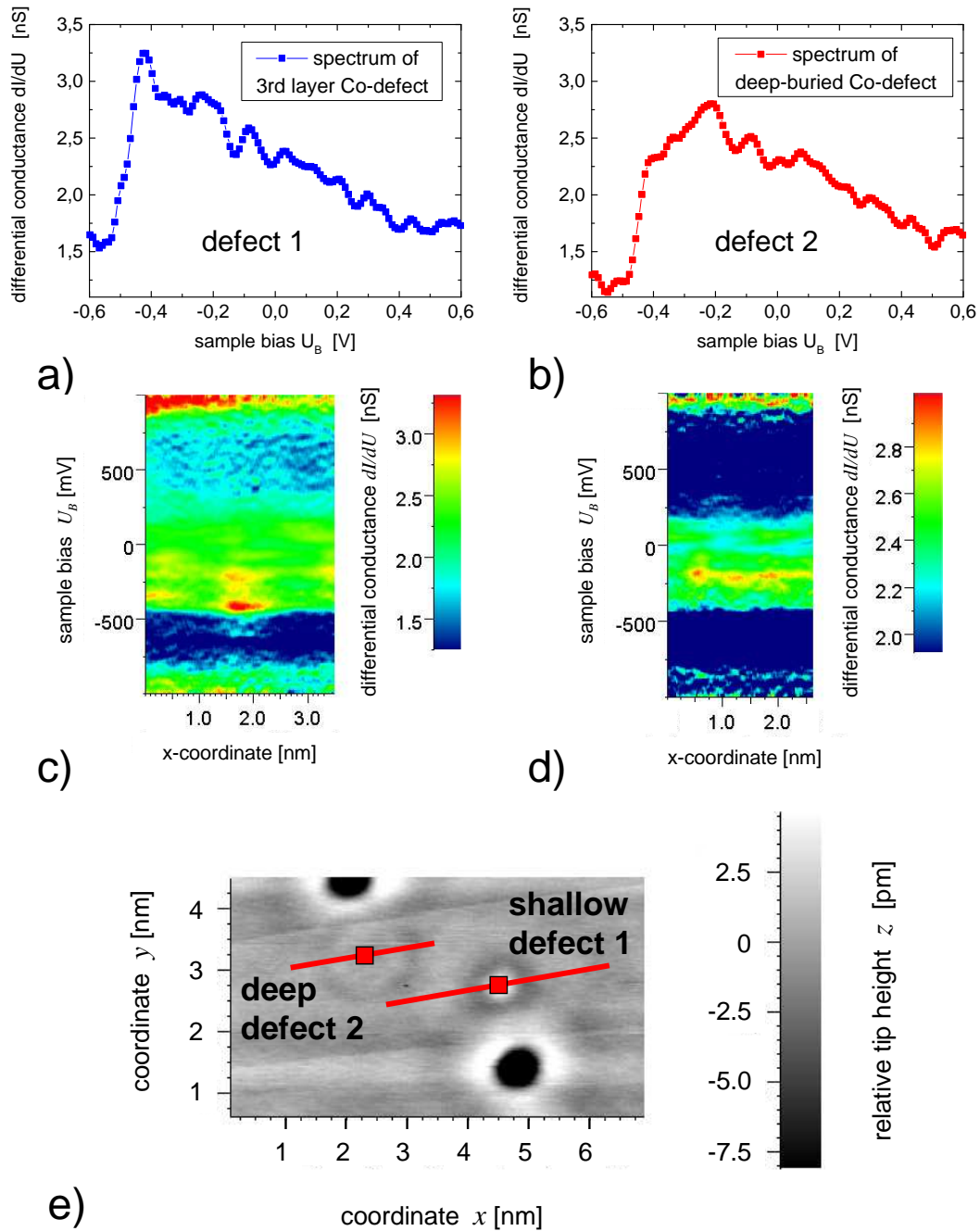
Figure 6.17: *Differential conductance dI/dU measured with the tip central on top of a) an impurity atom buried in the third-layer and b) an even deeper-lying defect atom. The spectra sections c) and d) show the spatial variation of the dI/dU spectra when moving the tip across the Co impurities along the lines indicated in the constant current image displayed in e).*
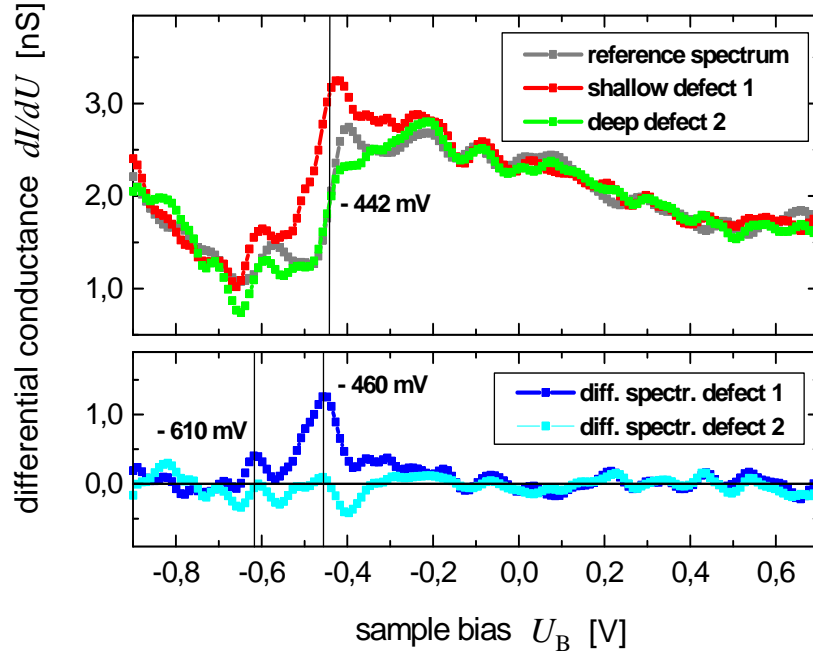
Figure 6.18: *Comparison of the LDOS of subsurface Co impurities with the spectrum of clean Cu(111). Characteristic differences appear only near the onset of the surface state around −400 mV.*

The resulting dI/dU spectra are shown in Fig. 6.17 a) and b). The curves mainly differ in their intensity at the bottom of the surface state band, representing the *LDOS* of a Co impurity in the third layer, and that in the centre of a deeper lying defect, respectively. In c) and d), the corresponding spectra sections are displayed. The contrast of the colour scale is adjusted individually, in order to emphasize the spatial variations. In the case of the third-layer defect, the pronounced peak at the onset of the surface state is seen to extend over roughly 7 Å in radius. Enhanced signal in this area is also observed at voltages around $U_B \sim$-200 meV and $U_B \sim$-600 meV. At a radial distance of about 10 Å or more, these anomalies have vanished and the spectra closely resemble the well-known dI/dU spectrum of the free surface. In contrast to that, the spectroscopy centered on the deep-buried defect shows a particularly low dI/dU signal directly at the surface state onset. The maximum is reached at about $U_B \sim$-200 meV and this is where the spatial variation in the corresponding spectra section d) comes out most clearly. Three regions of enhanced differential conductance are seen there, which correspond to the slight depressions seen as a dark pattern in the constant current image shown in e).

For direct comparison, Fig. 6.17 displays difference spectra obtained by subtraction of the Cu surface reference spectrum from the defect spectra. As expected, the plot reveals an increased intensity slightly below the onset of the surface state at the location of the

shallow impurity, which is seen as a lower lying peak centered at about -460 meV in the difference spectrum. As well, the deeper-lying impurity exhibits a spectrum that lacks intensity in this range. The onset of the surface state here fits perfectly with the reference, only the maximum that the reference spectrum reaches at -400 meV is not present on the deep impurity.

Towards higher energies, above -200 meV, the three spectra can be considered identical. One has to note, that the character of these spectra is dominated by the *DOS* of the surface state electrons. Especially, there is no sign of a spectral feature around the Fermi-energy, such as the dip observed for the surface layer Co impurities. The possibility that the reason for this is trivial, and the impurities are no Co atoms, must be acknowledged, but the probability for this is also considered to be very low. Instead, these observations must lead to the opinion that the surface state electrons locally respond to the crystal defect represented by the Co impurity. It is interesting to compare the present spectra with the data of Madhavan *et al.*, who studied Co *adsorbates* on Au(111) also over an extended bias range [135]. Their spectrum show the Kondo-dip at zero bias, but it *also* shows a peak at an energy somewhat *below* the surface-state onset on the free terrace. This peak obviously persists when a non-magnetic adsorbate atom like Cu is probed, while the Kondo-dip disappears. It thus seems that these peaks at negative bias are ordinary defect-induced features in the *LDOS* of the surface state.

6.3.5 Co_n complexes – thermal stability of $Co_{0.001}Cu_{0.999}$

One of the samples, the homogeneously mixed alloy film, was held in the UHV chamber at room temperature for some time after the first examination with the tunnelling microscope. The film was allowed to undergo a ripening process at 295 K for about 20 days and was then reexamined with the STM at low temperatures. The observations made in these experiments differed to some extent from the data we had from the freshly prepared film. Although the properties of the bulk alloy are dominated by phase separation, an admixture of 0.1% of Co to Cu is generally believed to be completely solvated in the bulk [136]. The present images recorded on the aged alloy film, however, suggest a slightly different picture.

First, it must be mentioned that the surface of the sample has remained very clean over the comparably long time it was held in UHV (p_{STM} better than $1 \cdot 10^{-10}$ mbar). However, although a number of adsorbates was observed at the surface, the majority of the defects was not of that type. The defects that were visible had increased in number, but they seemed to be located inside the crystal, which is indicated by the very low tip heigth profile of only few pm (compare with Fig. 6.8). A major change concerns the deep-buried Co scattering centers that are described in paragraph 6.3.2. The film on which these ring-like patterns originally had been observed did not show such defects anymore after being kept three weeks at room temperature. Additionally, this film was the only sample which showed signs of impurity clustering, which is shown in Fig. 6.19. It should be noted that these constant current images display height variations of some few picometers. It is
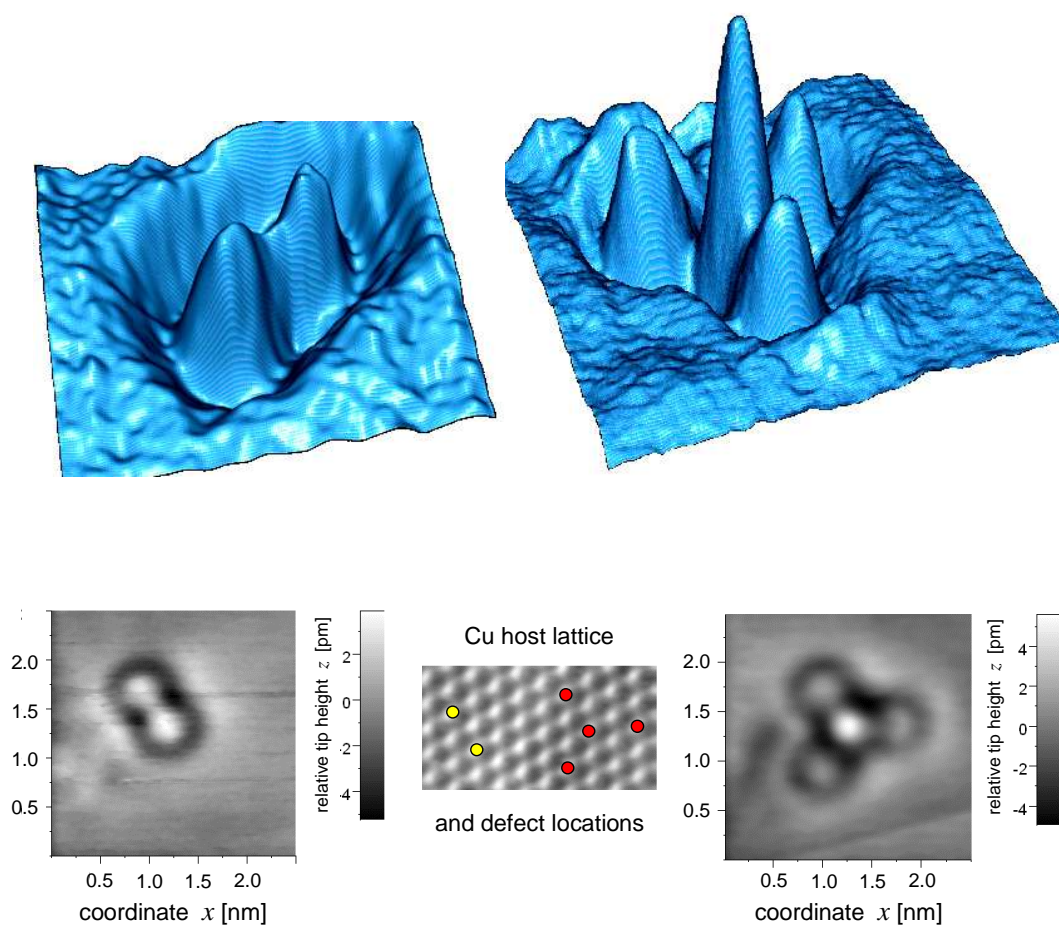
Figure 6.19: *Complexes of Co_n below the surface of Cu(111) aggregated by RT diffusion. The structure fits with the Cu host lattice, while the Co occupy next-nearest-neighbour sites, their axes having [110] orientation.*

rather clear that they depict no adsorbate or surface layer structures. Comparison with the classification of surface-near single defects made in paragraph 6.3.2 proposes that the constituents of the clusters lie in the *third layer*, and thereby actually *below* the surface. It therefore seems that the room temperature storage results in diffusive ripening of the surface-near homogeneously prepared dilute alloy film. The bulk impurities detected before by the ring-shaped patterns appear to have moved towards the surface, where they prefer surface-near subsurface positions with a tendency to form complexes.

It is well known from heteroepitaxy of Co on Cu(111) that deposition of sub-monolayer coverages results in two-monolayer high triangular Co islands, which have been studied in detail by STM [137, 138]. These are believed to actually consist of a three layer high partially alloyed object with the lowest layer buried in the surface [139]. The observation

of a sort of etching at the substrate step edges by the deposited Co also promotes the view that microscopic intermixing at the surface is strongly favoured at room temperature. A theoretical study by Robles *et al.* on the ground state properties of Co clusters at the Cu(111) surface has indicated that their stable configuration is not the adsorbate or surface layer position but rather the buried state below the surface [140]. This is in agreement with the general conclusions drawn from the experimental observations of Co-Cu epitaxy. Furthermore, Robles *et al.* found that ground state Co_n clusters should reside mainly in the third layer below the surface, their shape being governed by the aim to have the most Co atoms lying in that layer. Looking at Fig. 6.19, it is obvious that the Co complexes observed in this work comply with both the calculated and the experimental findings. Their structure is such that the third layer is preferred by the Co, and it also is compatible with a strong tendency to locally form an alloy, which is expressed in the observed next-nearest-neighbour configuration instead of the nearest-neighbour structure. This configuration can, however, also be due to kinetic limitations at RT and be not the ground state structure. Nevertheless, it is in accordance with observations of the diffusion behaviour of embedded Co atoms in Cu(001) [141], where it was found that the diffusional jumps occur preferentially in [110]-directions, which are just the directions of the Co-Co axes visible in Fig. 6.19. In order to get definitive experimental evidence in these points, a systematic preparational study on controlled annealing of dilute alloy films must be conducted.

6.3.6   Discussion

The discussion in this paragraph will be restricted to the Kondo-effect of embedded magnetic impurities, while other aspects of the experiments that have been mentioned, such as the bulk state impurity scattering and the subsurface clustering, were shortly discussed in the respective paragraphs.

The present STM and STS investigations of dilute Co in Cu demonstrate that it is possible to successfully probe the properties of embedded impurities in a dilute magnetic alloy with the tip of an STM. The characteristic dip in the differential conductance that is attributed to the Kondo resonance at E_F is only resolved in local tunnelling spectroscopy when the impurity is directly accessible from the surface, i.e. located in the surface layer. Surface as well as subsurface impurities can be identified easily in constant current mode, so that even a classification of their depths is possible, within certain limits. However, tunnelling spectroscopy performed on shallow, buried defects cannot identify them as Kondo impurities by the typical dip at E_F. This fact alone is an important finding, since it clarifies that the well-known Kondo-feature in STS does not extend beyond the two atomic spacings vertically from the impurity to the surface. So far, all experimental studies were performed on adsorbates, which are directly accessible with the tip. Actually, an adsorbate lies inside the tunnelling gap, and the STM tip necessarily retracts from the substrate while scanning across. In the adsorbate geometry, the current going directly

through the impurity atom must play a prominent role, and it surely carries the complete tunnelling current with the tip directly above it. In contrast, the spectroscopies of the subsurface layer impurities have shown that in case of a third-layer Co atom, the surface state has already fully developed at the surface above the impurity. Thus, a Co atom buried in the third layer is screened and thus located outside the tunnelling junction. The absence of a Kondo-dip in their spectra finally is consistent with the absence of a dip near surface Co impurities at a lateral distance $R \sim 5$ Å (Section 6.3.3).

The geometry in the present experiments on embedded surface impurities should be the simplest one for an interpretation using available theoretical work. The tip height change while scanning across is minimal, while direct tunnelling into the Co atom is possible. The surface layer Co impurities imaged in constant current mode appear as 30 pm depressions in the Cu surface. This amount of change in tip height corresponds to a reduction in the local conductance by a factor of two, based on a decade's current change per Å. The surface state - as was already mentioned - also causes an increase of factor two in the conductance. Thus, the constant current image of the embedded Co can be explained by assuming that the surface state is depleted and does not contribute to the tunnelling current at the position of the Co impurity. From the spectra section shown in Fig. 6.20 it
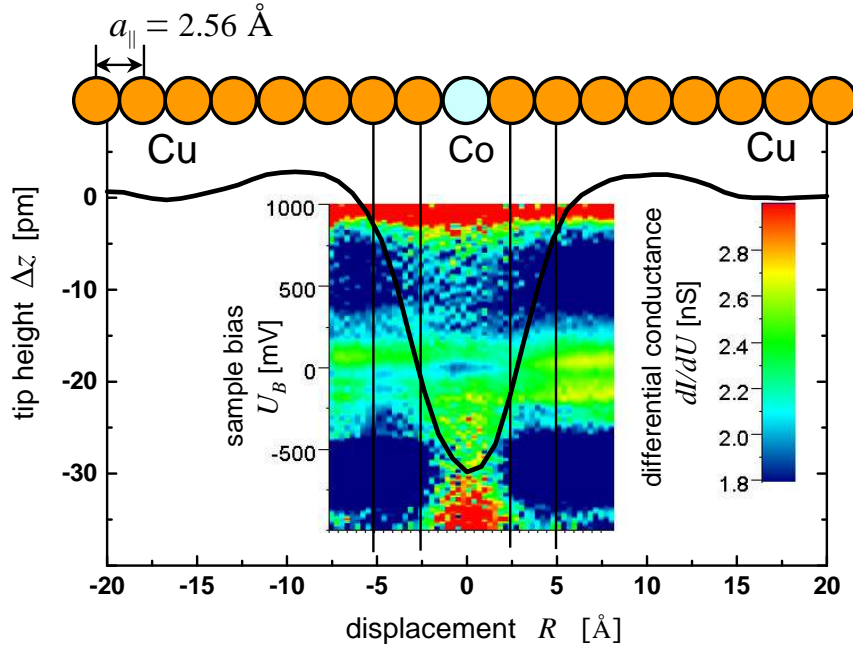

Figure 6.20: *Comparison of length scales involved with differential conductance spectra across a surface layer Co impurity in the Cu(111) surface. The tip height profile is dominated by the surface state LDOS ($\lambda_F/2 \sim 14$ Å) and shows that the Kondo-dip at zero bias coincides with a vertical proximity between tip and Co atom. Laterally, the dip appears within about twice the hard-shell radius of the Co defect.*

is evident that the characteristic dip is only seen in a very restricted region. The spatial extension of this feature is hardly larger than the area taken in by the embedded impurity atom in the matrix. Therewith, its extension is much smaller than what was reported for adsorbate atoms. In critically reviewing the data in ref. [107], it must be noted that also in the adsorbate cases, the spatial extension of the dip coincides with that of the bump produced by the adatom in the tip height profile in the constant current trace. The sum of these observations therefore proposes that the Kondo-*dip* in dI/dU spectra only appears, when the tunnelling current, or at least a substantial fraction of it, can directly go through the impurity atom.

The width of the dip was used to determine the Kondo-temperature of a single Co atom embedded in the surface. The function fitted to the differential conductance data is based on the result of the theoretical work of Ujsaghy *et al.* [128] who recover Fano's result [131], which yields the parameters T_K and q. The Kondo-temperature with $T_K = 405$ K was found to be nearly eight times higher than the Kondo temperatures that were extracted from earlier measurements on Co adsorbates. This outcome complies with general expectations (Eq. 6.1). A quantitative comparison was made using the simple scaling relation introduced by Knorr *et al.* [107]. This scaling $\rho_0 \cdot J_{eff} \sim n$ with the number of nearest-neighbour matrix atoms fits surprisingly well for the Kondo-temperatures determined on single adsorbates [106, 107], on single embedded impurities measured in this work, and for the bulk system [118]. The good agreement indeed shows that Cu can be considered to provide a perfect jellium-like environment for the impurity, where at a fixed exchange constant the host electron density at the impurity site increases proportional to the solid angle under which the host electrons can impinge. The bonding properties of the Co sp-shell electrons with the host thus seem to be ideally metallic down to the size of an atomic volume. The special value that falls to the T_K determination made here with STS on the embedded system is that the high values that were measured at bulk samples using macroscopic methods have now been confirmed by a local, microscopic method. The result grants more confidence to the Kondo-temperature of Co in Cu that on average lies around 500 K. Provided that the scaling is accurate enough, Fig. 6.13 even indicates that it might lie slightly higher. Comparing the present result with very recent theoretical work by Lin *et al.* [142], we find that their calculation of the Kondo temperature as a function of impurity-surface distance gives a too low value to fit the experimental T_K of an embedded surface impurity at $z = 0$, but yet their function is exponentially increasing as expected from Eq. 6.1 in Section 6.1.

One further aspect of the experimental Kondo-dip to be discussed is the very low asymmetry parameter q, which was found to be $0.03 \leq q \leq 0.2$ in the present measurements. In the case of Co adsorbed on Cu(111), q was determined to be around 0.2 [107]. An embedded Co impurity therefore has a q equal to or smaller than that of an adsorbed Co atom. The difference between the two experiments might be explained by a simple argument based on Plihal and Gadzuk's analysis of the line shape variation with the tip height over an adsorbate [129]. The reason for this is that *different* decay constants govern the vacuum tail of the localized impurity state and the delocalized substrate states. By

placing the impurity into the surface layer, rather than on top of it, the vacuum tail of the substrate electrons are shifted up for some amount. Therefore, the transfer directly to the substrate is enhanced, which results in a lower value of q. The relatively high setpoint that necessarily was used in the present experiments also contributes to a dominant tunnelling into the substrate states, since they have the longer decay length. This experimental result contradicts the conclusions of a very recent theoretical study on the Co-on-Cu adsorbate system [130]. That work finds the tendency of an increasing asymmetry q with decreasing adsorbate-substrate distance z. For embedded impurities with $z = 0$, this is not observed experimentally here. However, the calculations also indicate a strong q-dependence on the details of the solid-vacuum interface model. In that case, the adsorbate is reduced to its localized d-level held in vacuum at a certain distance from the surface. A more realistic description of the situation might be the inclusion of the adsorbate s-state as a protrusion of the otherwise flat surface, that encompasses the d-state due to the metallic bonding of the adatom to the substrate.

For discussing the spatial variation of the impurity spectra around E_F, we consult the careful theoretical modelling of the experimental circumstances by Plihal and Gadzuk, who considered the complete tip-adsorbate-substrate system in their work [129]. The calculations of Ujsaghy *et al.*, whose Fano-result was used in the analysis to fit the line shapes, disregard the *direct* tunnelling between tip and localized state in their theory. The results of Plihal and Gadzuk in fact indicate that the dependence of local conductivity
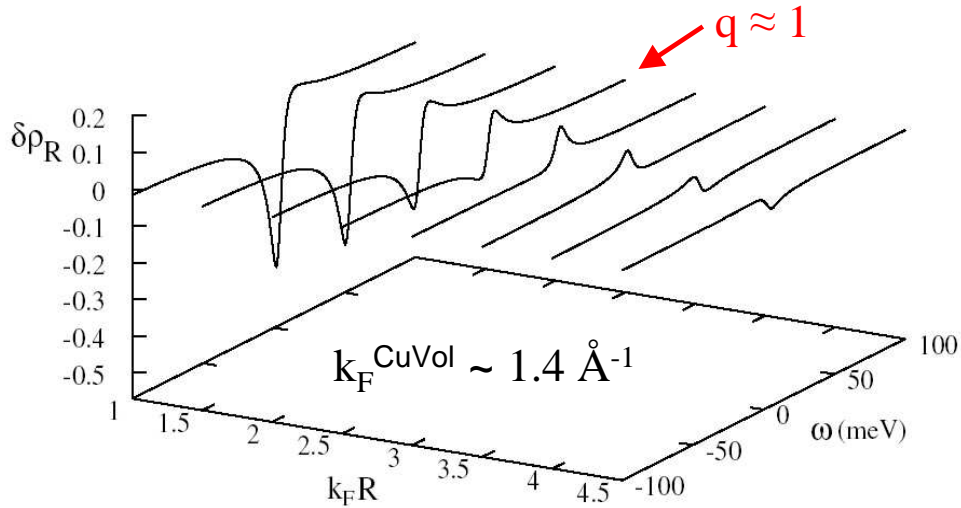

Figure 6.21: *Calculated modification of a uniform sample LDOS due to a magnetic impurity atom by Ujsaghy and coworkers [128]. The spectral shape around E_F is plotted parametrized with the product of $k_F R$, where R is the lateral tip distance from the impurity. Graphics reproduced from ref. [128].*

spectra on the direct transfer between localized state and tip can safely be neglected, especially at finite lateral distances between tip and impurity centre. For this case, they find a Fano line shape with an asymmetry parameter q that oscillates between zero and ∞ with the radial distance R between tip and impurity (see Fig. 6.21). A similar result is gained by Plihal and Gadzuk, however under conditions of unrealistically small tip-surface separations. An ordinary s-wave tip modelling here tends to smear out the oscillations at experimentally realistic tip heigths over the substrate. The function for the spatial dependence that Plihal and Gadzuk calculate for a tunnelling gap of 5 Å and a substrate-$k_\parallel$ of 1.2 Å^{-1} shows that the Kondo anomaly in the dI/dU signal should vanish within a radius of 3 Å [129]. This in turn agrees with the predictions made by Ujsaghy *et al.*, assuming the identical substrate-$k_\parallel$. The spectra recorded in this work actually show a disappearance of the *characteristic dip* within this range. As was already proposed above, it is therefore quite probable, that the measured extension of the dip up to 10 Å in the case of adatoms [106, 135] is artificially enlarged due to the non-constant tip height, which of course experimentally is inevitable in the adatom geometry.

The closer examination of the dI/dU signal recorded near the embedded Co impurity with the tip some Ångstrøms apart has given well averaged quantitative information on
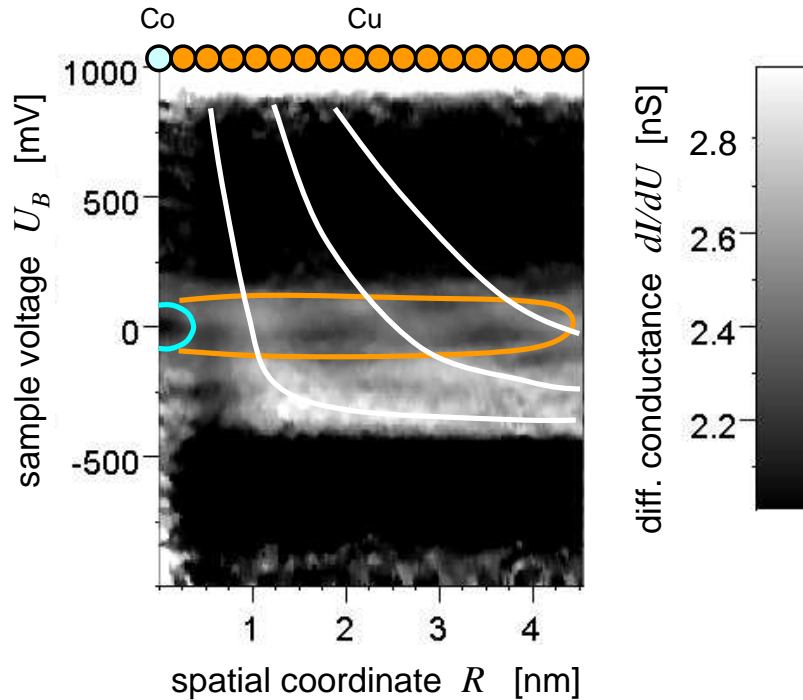

Figure 6.22: *dI/dU spectrum section radially outwards from a surface layer Co impurity in the Cu(111) surface. To the left, at the location of the Co atom, the Kondo-dip is seen as the dark spot at zero bias, while with half the wavelength of the surface state Fermi-wave vector, the spectra around E_F show a clear periodicity.*

the shape of the spectrum and its change with the radius R. Qualitatively, this is also evident from the spatially resolved spectra section representation shown in Fig. 6.14 and Fig. 6.20. The fact that the changing line shapes at different r can well be fitted by a Fano-function with identical T_K and ϵ_K suggests that the electronic properties probed in the vicinity of the Co might actually show the substrate $LDOS$ perturbation effects shown in Fig. 6.21. The asymmetry factor q increasing with radius R qualitatively agrees with the theoretical prediction [128]. This behaviour is different from the spatial dependence reported by Manoharan *et al.* and Knorr *et al.*, who saw a largely constant q, rather showing a small decrease with the distance from the scatterer on Cu(111) [106, 107]. In our data, the asymmetry parameter grows, but not much above $q \sim 1$ when R increases beyond 5 Å.

However, if one looks at the $LDOS$ farther out from the impurity, which is shown here as a spectra section in Fig. 6.22, there are distinct oscillations in the $LDOS$ in the energy range around E_F, having the period of about half the surface state Fermi-wave vector. Clearly, these are the Friedel-oscillations of the surface state electrons scattering at the impurity. The figure should illustrate that there are two length scales visible in our data – the short-range one is the local Kondo-dip disappearing on a length scale of Ångstrøms, and the other one is the rather long-range surface state period, also with pronounced $LDOS$ variations seen around E_F. An analysis of the $LDOS$ at such larger distances might give further insight into the scattering behaviour of the surface state, but this ideally requires data on a widely isolated Co impurity. In conjunction with the present results, Fig. 6.22 shows how the surface state $LDOS$ is gaining weigth if the tip is moved farther apart from the scattering centre. This also becomes obvious from the absolute values of the differential conductance in Fig. 6.15 a) and the overall shape of the spectra in Fig. 6.15 b). Around zero bias, data taken at $R = 6.5$ Å already resemble more closely the reference spectrum of the surface state than the data taken at $R = 0$ Å. In the embedded geometry, the charge density of the surface state thus is contributing to the tunnelling current already at very small distances of the tip from the Co atom, so that probably a superposition of two channels, the impurity or bulk state channel and the surface state channel,is present in the measurement. Finally, this is also evident from the constant current cross section of the top layer Co in Fig. 6.8 and Fig. 6.20, where the tip has already moved up 20 pm at a displacement of 5 Å from the central minimum due to the surface state contribution to the tunnelling current. It is hard to clearly distinguish whether the line shape variation seen around the Co in the region outside about 3 Å is to be assigned to the small scale or the large scale, but some indication is found for the surface state contribution.

6.4   Conclusion

The results presented in this chapter bridge a gap in the experimental data presently available on the dilute Co/Cu Kondo system. The investigation of single *embedded* surface layer impurities is the first step towards investigating bulk Kondo systems locally using

atomically resolved STS. The Kondo-temperature that was measured for the embedded impurity with $T_K = 405 \pm 35$ K is much higher than the T_K previously reported for Co adsorbate atoms on Cu(111) and Cu(100). The T_K found here does substantially support a scaling model for the Kondo-temperature proposed by Knorr and coworkers, which considers the number of nearest-neighbour matrix atoms [107]. The shape of the Kondo-antiresonance is found nearly symmetric with the tip on top of the Co impurity. A Fano asymmetry factor between $q = 0.03 \pm 0.03$ and $q = 0.20 \pm 0.05$ has been determined, dependent on the application of a background slope substraction. This finding contradicts very recent theoretical results, which predict an increased q-value with reduced adsorbate-substrate distance for an adsorbate atom [130]. The analysis of the spatial dependence of the tunnelling spectra around the embedded Co atom shows a disappearance of the antiresonance within 3 Å , but develops to an asymmetric shape at about 5Å from the defect. Such a behaviour qualitatively is predicted for the Cu matrix $LDOS$ theoretically, while we cannot safely exclude other reasons for this spectral shape around zero bias at the present point. Some indication is found that the surface state $LDOS$ starts to strongly contribute to the tunnelling spectra when the tip is placed as little as 3 Å off the defect centre.

Chapter 7

Summary

This thesis addresses three topics in the solid state and surface sciences by use of scanning tunnelling microscopy methods on metal surfaces. Rigorously, the investigated systems all would have to be considered as many-particle systems, however, in two cases - analysis of surface diffusion and spectroscopy of surface electronic states - a sufficiently accurate single particle theoretical description can be employed. In the third case - measuring the Kondo-effect at isolated impurity atoms - a single particle picture is not appropriate. Experimental and theoretical work in this field is an ongoing challenge in solid state and many-body physics.

The first topic that is investigated are the diffusion processes on Ag(111) which are activated at room temperature. Nanoscale step and island structures have been observed by recording STM movies documenting the change of their shape with time. The decay of a monatomic island due to a special crossing-step geometry was analyzed using time-resolved STM imaging. By observing how the relaxation of local non-equilibrium structures proceeds, we could directly identify diffusion along step edges as the most efficient mass transport channel at room temperature on Ag(111). The Gibbs-Thomson relation was used to evaluate the corresponding transport coefficient, which enables the determination of an effective activation barrier for step edge diffusion. We find $E_{eff} = 0.49 \pm 0.05$ eV, which within the error limits is identical with barriers reported for island diffusion [61]. This experimentally confirms that island boundary fluctuations at room temperature are governed by the mechanisms of step edge diffusion, and proposes that kink upward hopping is the rate-limiting elementary step in this process.

Using the spectroscopic mode of the STM, the L-gap surface state electron bands both on Ag(111) and Cu(111) were characterized using spatially resolved STS at temperatures below 8 K. The border of nanometer-sized hexagonal islands that are formed during homoepitaxial growth sets up a confinement for surface state electrons. On Ag(111), characteristic energy-dependent $LDOS$ patterns of confined surface state electrons were observed

on such islands. A progression of peaks that was measured locally at the island centre originates from seven states having a non-zero weight at this high-symmetry centre. The spectrum clearly exhibits *all of* the confined states that were predicted theoretically by use of a single-particle model [99]. Thus, three peaks could be assigned that have not been resolved in a previous study by Li *et al.* [99]. The theoretical analysis was used to determine the energy of the onset $E_\Gamma = -68 \pm 1$ meV, and the effective mass $m^* = 0.41 \pm 0.02$ meV for the Ag(111) surface state. On Cu(111), the surface state spectroscopy on a large island was analyzed in terms of a 2D model for electron scattering at a straight step edge. The spectral analysis using this approach yields a dispersion curve with the parameters $E_\Gamma = -433 \pm 2$ meV and $m^* = 0.40 \pm 0.02$ meV. For both Ag and Cu, the results are in very good agreement with values gained in previous STM and PES studies. On Ag(111), the width of the peaks in the progression was found to increase stronger than linearly, suggesting a quadratic dependence of the electron lifetimes with energy, which is in contrast to the findings from previous experiments.

Finally, results are presented which bridge the gap between microscopic and macroscopic investigations of the Co/Cu Kondo-system, constituted by dilute Co atoms in a Cu matrix. The Kondo-effect arising from dissolved transition metal impurity atoms in a non-magnetic host metal is known to be responsible for a variety of low-temperature anomalies that modify the physical properties of the pure noble metal. The local spectroscopy of single surface layer impurities as it was done here is the first step towards investigating bulk Kondo systems microscopically, using atomically resolved STS at $T < 8$ K. The Kondo-temperature of an *embedded* Co surface impurity with $T_K = 405 \pm 35$ K was found much higher than the T_K previously reported for Co *adsorbate* atoms on Cu(111) and Cu(100). The T_K of the embedded impurity measured in this work substantially supports a scaling proposed by Knorr and coworkers [107], after which the Kondo-temperature is determined by the number of nearest-neighbour matrix atoms. The shape of the Kondo-antiresonance is found nearly symmetric with the tip on top of the Co impurity. A Fano asymmetry factor between $q = 0.03 \pm 0.03$ and $q = 0.20 \pm 0.05$ has been determined, depending on the application of a background slope substraction. This contradicts very recent theoretical results, predicting an increased q-value with reduced adsorbate-substrate distance for an adsorbate atom [130]. The analysis of the spatial dependence of the tunnelling spectra around the embedded Co atom shows that the antiresonance disappears within 3 Å , but develops towards an asymmetric shape at about 5Å from the defect. Qualitatively, such a behaviour is predicted by theory for the Cu matrix $LDOS$, while we cannot safely exclude other reasons for this behaviour of the spectral shape around zero bias. Some indication is found that the surface state $LDOS$ starts to strongly contribute to the tunnelling spectra when the tip is placed as little as only 3 Å off the defect centre.

Appendix A

Eigenstates of a particle in a hexagonal box

The calculations of Li *et al.* that were compared to our tunnelling spectra in the centre of a hexagonal Ag island in Chapter 5 are summed up here from ref. [100].

As the most simple assumption, Li *et al.* used a two-dimensional 'particle-in-a-box' model to calculate the energies and the eigenstates of a hexagonal box with infinetely high barriers. An analytic solution for this geometry is not possible, and a numerical approach was used based on an embedding scheme for confined quantum systems [143]. The zero-amplitude boundary condition is imposed variationally. The basis functions are chosen as a product of the cylindrical Bessel function and an oscillating angular part. A finite basis set (see ref. [100]) suffices to accurately calculate the first 20 eigenvalues. These individual confined states are shown in Fig. A.1 with the state densities $|\Psi_n(r)|^2$ normalized to equal maximum amplitude. They are labelled according to the irreducible representations of the C_6 group of the hexagon. Their eigenvalues are calculated according to Eq. 5.3 from the λ_n that are listed below:

Table A.1: *Normalized eigenvalues λ_n of a hexagonal box with $m^* = 1$ and $\Omega = 1$ in atomic units $\hbar = m_e = e^2 = 1$. Unit of Ω is $2.80 \cdot 10^{-3}$ Å^2 and unit of E is 27.21 eV.*

n	λ_n	n	λ_n	n	λ_n	n	λ_n
1	9.296	6	68.38	11	122.5	16	162.4
2	23.55	7	78.08	12	143.4	17	189.0
3	42.16	8	91.12	13	157.0	18	198.3
4	48.70	9	113.7	14	159.6	19	215.0
5	61.87	10	117.0	15	159.6	20	219.3

n=1 : A_1 n=2 : E_1 n=3 : E_2

n=4 : A_1 n=5 : B_1 n=6 : B_2

n=7 : E_1 n=8 : E_2 n=9 : E_2

n=10: A_1 n=11: E_1 n=12: B_1

n=13: A_1 n=14: A_2 n=15: B_2

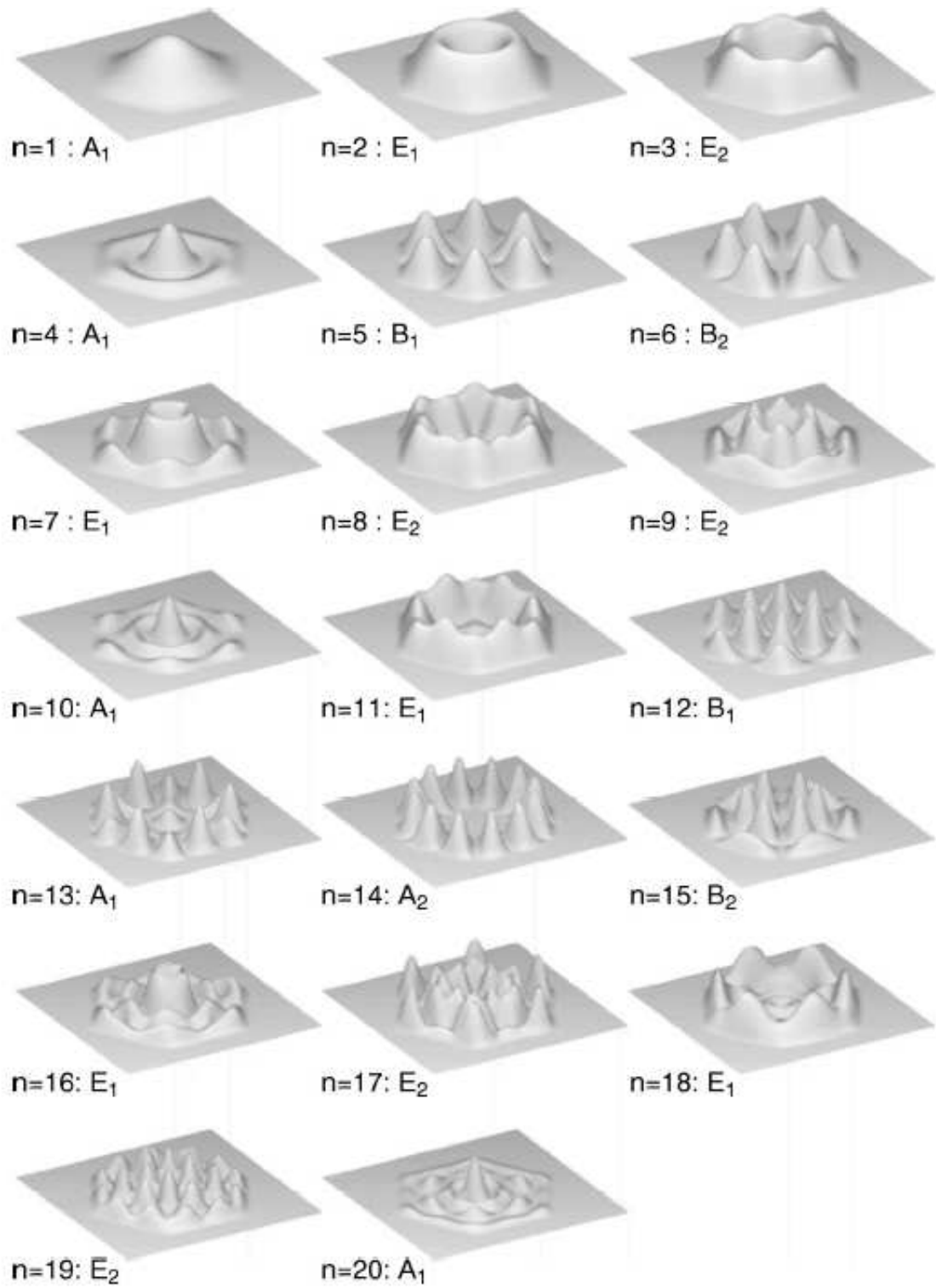n=16: E_1 n=17: E_2 n=18: E_1

n=19: E_2 n=20: A_1

Figure A.1: *See the previous page for description. Graphics reproduced from ref. [100].*

Appendix B

Low-density limit in step edge diffusion

The estimates made here are based on the experimental kink energy by Steimer [69] and the calculated elementary energies by Schlöser/Stoltze [61] for Ag(111).

The kink density of a macroscopically straight step at room temperature is given by

$$P_k^{-1} = 2e^{E_k/k_B T} \tag{B.1}$$

with $E_k = 0.1$ eV and $T = 295$ K resulting in an average distance between two kinks of $d_{av} = 26.6$ sites. The two processes that produce single adatoms at the step are detachment from a kink site to the lower or the upper part of the step. The corresponding probabilities calculated with the energies from [61] are

$$P_{kl}^{diff} = e^{-0.37eV/k_B T} = 4.77 \cdot 10^{-7} \tag{B.2}$$

$$P_{ku}^{diff} = e^{-0.49eV/k_B T} = 4.25 \cdot 10^{-9}. \tag{B.3}$$

Compared to that are the probabilities for a step-adatom to execute a diffusive jump

$$P_A^{diff} = e^{-0.22eV/k_B T} = 1.74 \cdot 10^{-4} \tag{B.4}$$

$$P_B^{diff} = e^{-0.30eV/k_B T} = 7.49 \cdot 10^{-6}. \tag{B.5}$$

The number of steps N necessary on average for a step adatom to traverse 26.6 sites in one direction is determined by Eq. 4.1 to be $N = 708$. The low density limit can be considered a good approximation when the ratio of diffusion probability and detachment probability is on the order of N, which means that approximately only one adatom is moving between

two kink sites at a time. The ratios resulting from the above probabilities are

$$P_{kl}^{diff}/P_A^{diff} = 365 \tag{B.6}$$

$$P_{ku}^{diff}/P_A^{diff} = 1762 \tag{B.7}$$

$$P_{kl}^{diff}/P_B^{diff} = 15 \tag{B.8}$$

$$P_{ku}^{diff}/P_B^{diff} = 40940. \tag{B.9}$$

The low-density condition is well satisfied in all cases except for B.8. It can be concluded from these estimates that overall the low-density condition can be considered as being approximately fulfilled.

Bibliography

[1] G. Binnig and H. Rohrer, 'Scanning tunneling microscopy', Helv. Phys. Acta **55**, 726 (1982).

[2] R. Wiesendanger, *Scanning Probe Microscopy and Spectroscopy* (Cambridge University Press, 1994).

[3] Technical University of Eindhoven, *Proccedings of the 12th International Conference on Scanning Tunneling Microscopy/Spectroscopy and Related Techniques* (AIP, 2003).

[4] H.J. Hug, B. Stiefel, P.J.A. van Schendel, A. Moser, R. Hofer, S. Martin, S. Porthun, L. Abelmann, J.C. Lodder, G. Bochi, and R.C. O'Handley, 'Quantitative magnetic force microscopy on perpendicularly magnetized samples', J. Appl. Phys. **83**, 5609 (1998).

[5] J. Tersoff and D. Hamann, 'Theory and application for the Scanning Tunneling Microscope', Phys. Rev. Lett. **50**, 1998 (1983).

[6] I. Markov, 'Surface energetics from the transition from step-flow growth to two-dimensional nucleation in metal homoepitaxy', Phys. Rev. B **56**, 12544 (1997).

[7] A. Zangwill, *Physics at surfaces* (Cambridge University Press, 1988).

[8] S.G. Davison and M. Steslicka, *Basic theory of surface states* (Oxford University Press, 1992).

[9] A. M. Zagoskin, *Quantum theory of many-body systems* (Springer, New York, 1998).

[10] M.F. Crommie, 'Observing scattering in atomic-scale structures on metals', J. Electr. Spectr. and Rel. Phenom. **109**, 1 (2000).

[11] Ph. Avouris and I.W. Lyo, 'Observation of quantum-size effects at room temperature on metal surfaces with STM', Science **264**, 942 (1994).

[12] A.C. Hewson, *The Kondo Problem to Heavy Fermions* (Cambridge University Press, 1993).

[13] C.J. Chen, *Introduction to Scanning Tunneling Microscopy* (Oxford University Press, New York, 1993).

[14] J. Bardeen, 'Tunneling from a many-particle point of view', Phys. Rev. Lett. **6**, 57 (1961).

[15] I. Giaever, 'Energy gap in superconductors measured by electron tunneling', Phys. Rev. Lett **5**, 147 (1960).

[16] J. Tersoff and D.R. Hamann, 'Theory of the scanning tunneling microscope', Phys. Rev. B **31**, 805 (1985).

[17] C.J. Chen, 'Origin of atomic resolution on metal surfaces in Scanning Tunneling Microscopy', Phys. Rev. Lett. **65**, 448 (1990).

[18] J. Wintterlin, J. Wiechers, H. Brune, T. Gritsch, H. Höfer, and R.J. Behm, 'Atomic resolution imaging of close-packed metal surfaces by scanning tunneling microscopy', Phys. Rev. Lett. **62**, 59 (1989).

[19] N.D. Lang, 'Theory of single-atom imaging in the scanning tunneling microscope', Phys. Rev. Lett. **56**, 1164 (1986).

[20] C. Domke, Ph. Ebert, and K. Urban, 'Changes of defect and active-dopant concentrations induced by annealing of highly Si-doped GaAs', Phys. Rev. B **57**, 4482 (1998).

[21] R.M. Feenstra, J.A. Stroscio, J. Tersoff, and A.P. Fein, 'Atom-selective imaging of the GaAs(110) surface', Phys. Rev. Lett. **58**, 1192 (1987).

[22] K. Engel, 'Laboratory documentation IVC', (2001). IV. Physikalisches Institut, Georg-August-Universität Göttingen.

[23] A. Weismann, *Rastertunnelspektroskopie auf magnetisch verunreinigten Cu- und Ag-Einkristalloberflächen*, Diplom thesis, Georg-August-Universität Göttingen, IV. Physikalisches Institut (2003). Unpublished.

[24] K. Sauthoff, *Rastertunnelspektroskopie an einzelnen Donatoren und Donatorkomplexen nahe der GaAs(110)-Oberfläche*, Doktor thesis, Georg-August-Universität Göttingen, IV. Physikalisches Institut (2003). Published by Cuvillier Verlag, Göttingen.

[25] J. Müller, *Herstellung und Charakterisierung ultradünner Cu-Filme auf GaAs(110)-Spaltflächen für Ladungstransportmessungen mit dem Rastertunnelmikroskop*, Diplom thesis, Georg-August-Universität Göttingen, IV. Physikalisches Institut (2003). Unpublished.

[26] R.G. Musket, W. McLean, C.A.Colmenares, D.M. Makowiecki, and W.J. Siekhaus, 'Preparation of atomically clean surfaces of selected elements: A review', Applications of Surface Science **10** (1982).

[27] A.R. Smith, K.J. Chao, Q. Niu, and C.K. Shih, 'Formation of atomically flat silver films on GaAs with a *silver mean* quasi periodicity', Science **273**, 226 (1996).

[28] J. Müller, M. Wenderoth, N. Quaas, T.C.G. Reusch, and R.G. Ulbrich, 'Evolution of thin Cu films on GaAs(110) towards atomically flat epitaxial overlayers', Appl. Phys. Lett. **85**, 2220 (2004).

[29] M.A. Rosentreter, *Rastertunnelmikroskropie auf der GaAs(110)-Oberfläche bei Temperaturen von 8 K bis 300 K*, Doktor thesis, Georg-August-Universität Göttingen, IV. Physikalisches Institut (1997). Published by Cuvillier Verlag, Göttingen.

[30] N. Quaas, M. Wenderoth, and R.G. Ulbrich, 'Diffusive atom transport along step edges on Ag(111) at 295 K', Surface Science **550**, 57 (2004).

[31] D.M. Eigler and E.K. Schweizer, 'Positioning single atoms with a scanning tunnelling microscope', Nature **344**, 524 (1990).

[32] G. Meyer, L. Bartels, S. Zophel, E. Henze, and K.H. Rieder, 'Controlled atom by atom restructuring of a metal surface with the scanning tunneling microscope', Phys. Rev. Lett. **78**, 1512 (1997).

[33] G. Ayrault and G. Ehrlich, 'Surface self-diffusion on an fcc crystal: an atomic view', J. Chem. Phys. **60**, 281 (1974).

[34] G. Ehrlich and K. Stolt, 'Surface diffusion', Ann. Rev. Phys. Chem. **31**, 603 (1980).

[35] J. Wintterlin in: B.C. Gates and H. Knötzinger (eds.), *Impact of Surface Science on Catalysis* (Academic Press, 2000), vol. 45 of *Advances in Catalysis*, 131.

[36] M. Giesen, 'Step and island dynamics at solid/vacuum and solid/liquid interfaces', Prog. Surf. Sci. **68**, 1 (2001).

[37] J. Repp, F. Moresco, G. Meyer, and K.H. Rieder, 'Substrate mediated long-range interaction between adatoms: Cu/Cu(111)', Phys. Rev. Lett. **85**, 2981 (2000).

[38] N. Knorr, H. Brune, M. Epple, A. Hirstein, M.A. Schneider, and K. Kern, 'Long-range adsorbate interactions mediated by a two-dimensional electron gas', Phys. Rev. B **65**, 115420 (2002).

[39] F. Besenbacher, 'Scanning tunnelling microscopy studies of metal surfaces', Rep. Prog. Phys. **59**, 1737 (1996).

[40] H. Brune, 'Microscopic view of epitaxial metal growth: nucleation and aggregation', Surf. Sci. Rep. **31**, 121 (1998).

[41] A. Pimpinelli and J. Villain, *Physics of Crystal Growth* (Cambridge University Press, 1998).

[42] M. Poensgen, J.F. Wolf, J. Frohn, and H. Ibach, 'Step dynamics on Ag(111) and Cu(100) surfaces', Surf. Sci. **274**, 430 (1992).

[43] M. Giesen and H. Ibach, 'On the time structure of tunneling images of steps', Surf. Sci. **316**, 205 (1994).

[44] S.V. Khare and T.L. Einstein, 'Brownian motion and shape fluctuations of single-layer adatom and vacancy clusters on surfaces: Theory and simulations', Phys. Rev. B **54**, 11752 (1996).

[45] T. Ihle, C. Misbah, and O. Pierre-Louis, 'Equilibrium step dynamics on vicinal surfaces revisited', Phys. Rev. B **58**, 2289 (1998).

[46] K. Morgenstern, G. Rosenfeld, and G. Comsa, 'Decay of two-dimensional Ag islands on Ag(111)', Phys. Rev. Lett. **76**, 2113 (1996).

[47] M. Giesen, G. Schulze Icking-Konert, and H. Ibach, 'Fast decay of adatom islands and mounds on Cu(111): A new effective channel for interlayer mass transport', Phys. Rev. Lett. **80**, 552 (1998).

[48] M. Giesen and G. Schulze Icking-Konert, 'Equilibrium fluctuations and decay of step bumps on vicinal Cu(111) surfaces', Surf. Sci. **412**, 645 (1998).

[49] G. Rosenfeld, K. Morgenstern, M. Eßer, and G. Comsa, 'Dynamics and stability of nanostructures on metal surfaces', Appl. Phys. A **69**, 489 (1999).

[50] H. Ibach M. Giesen, C. Steimer, 'What does one learn from equilibrium shapes of two-dimensional islands on surfaces', Surf. Sci. **471**, 80 (2001).

[51] N.W. Ashcroft and N.D. Mermin, *Solid State Physics* (Harcourt college publishers, 1976).

[52] T. Michely and G. Comsa, 'Temperature dependence of the sputtering morphology of Pt(111)', Surf. Sci. **256**, 217 (1991).

[53] P. Stoltze, 'Simulation of surface defects', J. Phys. Cond. Matt. **6**, 9495 (1994).

[54] H. Brune, H. Röder, K. Bromann, K. Kern, J. Jacobsen, P. Stoltze, K. Jacobsen, and J. Nørskov, 'Anisotropic corner diffusion as origin for dendritic growth on hexagonal substrates', Surf. Sci. **349**, L115 (1996).

[55] R. Gomer, 'Diffusion of adsorbates on metal surfaces', Rep. Prog. Phys. **53**, 917 (1990).

[56] A. Einstein, 'Über die von der molekularkinetischen Theorie der Wärme geforderten Bewegung von in ruhenden Flüssigkeiten suspendierten Teilchen', Ann. d. Physik **17**, 549 (1905).

[57] D.A. Reed and G. Ehrlich, 'Surface diffusion, atomic jump rates and thermodynamics', Surf. Sci. **102**, 588 (1981).

[58] G.E. Murch and R.J. Thorn, 'Isothermal transport in the lattice gas', Philos. Mag. A **40**, 477 (1979).

[59] K. Maser, 'Darken's equation and other diffusion relations in the light of atomistic kinetic concepts', J. Solid State Electrochem. **4**, 3 (1999).

[60] G. Schulze Icking-Konert, M. Giesen, and H. Ibach, 'Decay of Cu adatom islands on Cu(111)', Surf. Sci. **398**, 37 (1998).

[61] D.C. Schlößer, K. Morgenstern, L. Verheij, G. Rosenfeld, F. Besenbacher, and G. Comsa, 'Kinetics of island diffusion on Cu(111) and Ag(111) studied with variable-temperature STM', Surf. Sci. **465**, 19 (2000).

[62] J.F. Wolf, B. Vicenzi, and H. Ibach, 'Step roughness on vicinal Ag(111)', Surf. Sci. **249**, 233 (1991).

[63] J. Christiansen, K. Morgenstern, J.Schiøtz, K.W. Jacobsen, K.-F. Braun, K.-H. Rieder, E. Lægsgaard, and F. Besenbacher, 'Atomic scale structure of dislocations revealed by scanning tunneling microscopy and molecular dynamics', Phys. Rev. Lett. **88**, 206106 (2002).

[64] K. Morgenstern, G. Rosenfeld, B. Poelsema, and G. Comsa, 'Brownian motion of vacancy islands on Ag(111)', Phys. Rev. Lett. **74**, 2058 (1995).

[65] M. Eßer, K. Morgenstern, G. Rosenfeld, and G. Comsa, 'Dynamics of vacancy island coalescence on Ag(111)', Surf. Sci. **402**, 341 (1998).

[66] K. Morgenstern, G. Rosenfeld, G. Comsa, M.R. Sørensen, B. Hammer, E. Lægsgaard, and F. Besenbacher, 'Kinetics of fast island decay on Ag(111)', Phys. Rev. B **63**, 045412 (2001).

[67] H. Ibach and H. Lüth, *Festkörperphysik* (Springer-Verlag, 1990).

[68] K. Morgenstern, G. Rosenfeld, E. Lægsgaard, F. Besenbacher, and G. Comsa, 'Measurement of energies controlling ripening and annealing on metal surfaces', Phys. Rev. Lett. **80**, 556 (1998).

[69] C. Steimer, M. Giesen, L. Verheij, and H. Ibach, 'Experimental determination of step energies from island shape fluctuations: A comparison to the equilibrium shape method for Cu(100), Cu(111), and Ag(111)', Phys. Rev. B **64**, 085416 (2001).

[70] A.F. Voter, 'Classically exact overlayer dynamics: Diffusion of Rhodium clusters on Rh(100)', Phys. Rev. B **34**, 6819 (1986).

[71] G. Rosenfeld, K. Morgenstern, and G. Comsa in: M.C. Tringides (ed.), *Surface Diffusion: Atomistic and Collective Processes* (Plenum Press, 1997), vol. 360 of *NATO ASI Series B*, 361.

[72] W.W. Pai, A.K. Swan, Z. Zhang, and J.F. Wendelken, 'Island diffusion and coarsening on metal(100) surfaces', Phys. Rev. Lett. **79**, 3210 (1997).

[73] A. Bogicevic, S. Liu, J. Jacobsen, B. Lundqvist, and H. Metiu, 'Island migration caused by the motion of the atoms at the border: Size and temperature dependence of the diffusion coefficient', Phys. Rev. B **57**, R9459 (1998).

[74] D.A. Sholl and R.T. Skodje, 'Diffusion of clusters of atoms and vacancies on surfaces and the dynamics of diffusion-driven coarsening', Phys. Rev. Lett. **75**, 3158 (1995).

[75] O. Jepsen, D. Glöetzel, and A.R. Mackintosh, 'Potentials, band structures, and Fermi surfaces in the noble metals', Phys. Rev. B **23**, 2684 (1981).

[76] H. Ehrenreich and H.R. Philipp, 'Optical properties of Ag and Cu', Phys. Rev. **128**, 1622 (1962).

[77] A. Bartelt, J.D. Close, F. Federmann, N. Quaas, and J.P. Toennies, 'Cold metal clusters: Helium droplets as a nanoscale cryostat', Phys. Rev. Lett. **77**, 3525 (1996).

[78] F. Federmann, K. Hoffmann, N. Quaas, and J.P. Toennies, 'Spectroscopy of extremely cold silver clusters in Helium droplets', Eur. Phys. J. D **9**, 11 (1999).

[79] U. Mizutani, *Electron Theory of Metals* (Cambridge University Press, 2001).

[80] J.A. Verges and E. Louis, 'Electron states on the (111) surface of copper', Sol. State Comm. **22**, 663 (1977).

[81] F. Reinert, G. Nicolay, S. Schmidt, D. Ehm, and S. Hüfner, 'Direct measurements of the L-gap surface states on the (111) face of noble metals by photoelectron spectroscopy', Phys. Rev. B **63**, 115415 (2001).

[82] H. Lüth, *Solid Surfaces, Interfaces and Thin Films* (Springer, Berlin, Heidelberg, 2001), fourth edn.

[83] A. Euceda, D.M. Bylander, and L. Kleinmann, 'Self-consistent electronic structure of 6- and 18-layer Cu(111) films', Phys. Rev. B **28**, 528 (1983).

[84] W. Shockley, 'On the surface states associated with a periodic potential', Phys. Rev. **56**, 317 (1939).

[85] I. Tamm, 'Über eine mögliche Art der Elektronenbindung an Kristalloberflächen', Z. Physik **76**, 849 (1932).

[86] L. Bürgi, L. Petersen, H. Brune, and K. Kern, 'Noble metal surface states: deviations from parabolic dispersion', Surf. Sci. **447**, L157 (2000).

[87] M.F. Crommie, C.P. Lutz, and D.M. Eigler, 'Imaging standing waves in a two-dimensional electron gas', Nature **363**, 524 (1993).

[88] Y. Hasegawa and P. Avouris, 'Direct observation of standing wave formation at surface steps using scanning tunneling spectroscopy', Phys. Rev. Lett. **71**, 1071 (1993).

[89] J. Li, W.D. Schneider, and R. Berndt, 'Local density of states from spectroscopic scanning-tunneling-microscope images: Ag(111)', Phys. Rev. B **56**, 7656 (1997).

[90] O. Jeandupeux, L. Bürgi, A. Hirstein, H. Brune, and K. Kern, 'Thermal damping of quantum interference patterns of surface-state electrons', Phys. Rev. B **59**, 15926 (1999).

[91] L. Bürgi, *Scanning Tunneling Microscopy as local probe of electron density, dynamics, and transport at metal surfaces*, Ph.D. thesis, Ecole Polytechnique Federale de Lausanne (1999).

[92] J. Li, W.D. Schneider, R. Berndt, O.R. Bryant, and S. Crampin, 'Surface-state lifetime measured by scanning tunneling spectroscopy', Phys. Rev. Lett. **81**, 4464 (1998).

[93] J. Kliewer, R. Berndt, E.V. Chulkov, V.M. Silkin, P.M. Echenique, and S. Crampin, 'Dimensionality effects in the lifetime of surface states', Science **288**, 1399 (2000).

[94] L. Bürgi, J. Jeandupeux, A. Hirstein, H. Brune, and K. Kern, 'Confinement of surface state electrons in Fabry-Prot resonators', Phys. Rev. Lett. **81**, 5370 (1998).

[95] M.F. Crommie, C.P. Lutz, and D.M. Eigler, 'Confinement of electrons to quantum corrals on a metal surface', Science **262**, 218 (1993).

[96] E.J. Heller, M.F. Crommie, C.P. Lutz, and D.M. Eigler, 'Scattering and absorption of surface electron waves in quantum corrals', Nature **369**, 464 (1994).

[97] S. Crampin, M.H. Boon, and J.E. Inglesfield, 'Influence of bulk states on laterally confined surface state electrons', Phys. Rev. Lett. **73**, 1015 (1994).

[98] S. Crampin and O.R. Bryant, 'Fully three-dimensional scattering calculations of standing electron waves in quantum nanostructures: The importance of quasiparticle interactions', Phys. Rev. B **54**, R17367 (1996).

[99] J. Li, W.D. Schneider, R. Berndt, and S. Crampin, 'Electron confinement to nanoscale Ag islands on Ag(111): A quantitative study', Phys. Rev. Lett. **80**, 3332 (1998).

[100] J. Li, W.D. Schneider, S. Crampin, and R. Berndt, 'Tunnelling spectroscopy of surface state scattering and confinement', Surf. Sci. **422**, 95 (1999).

[101] F. Baumberger, T. Greber, and J. Osterwalder, 'Step-induced one-dimensional surface state on Cu(332)', Phys. Rev. B **62**, 15431 (2000).

[102] O. Sanchez, J.M. Garcia, P. Segovia, J. Alvarez, A.L. Vazquez de Parga, J.E. Ortega, M. Prietsch, and R. Miranda, 'Lateral confinement of surface states on stepped Cu(111)', Phys. Rev. B **52**, 7894 (1995).

[103] Ph. Avouris, I.-W. Lyo, and R.E. Walkup, 'Real space imaging of electron scattering phenomena at metal surfaces', J. Vac. Sci. Technol. B **12**, 1447 (1994).

[104] G. Hörmandinger, 'Imaging of the Cu(111) surface state in scanning tunneling microscopy', Phys. Rev. B **49**, 13897 (1994).

[105] N. Quaas, M. Wenderoth, A. Weismann, R.G. Ulbrich, and K. Schönhammer, 'Kondo resonance of single Co atoms embedded in Cu(111)', Phys. Rev. B **69**, (R)201103 (2004).

[106] H.C. Manoharan, C.P. Lutz, and D.M. Eigler, 'Quantum mirages formed by coherent projection of electronic structure', Nature **403**, 512 (2000).

[107] N. Knorr, M.A. Schneider, L. Diekhöner, P. Wahl, and K. Kern, 'Kondo effect of single Co adatoms on Cu surfaces', Phys. Rev. Lett. **88**, 096804 (2002).

[108] E. Hildebrand, 'Zum Dia- und Paramagnetismus in metallischen Mischkristallreihen. Das Verhalten von gelöstem Kobalt und Rhodium', Ann. d. Physik **30**, 593 (1937).

[109] W.J. de Haas, J. de Boer, and G.J. van den Berg, Physica **1**, 1115 (1933).

[110] J. Kondo, 'Resistance Minimum in Dilute Magnetic Alloys', Prog. Theor. Phys. **32**, 37 (1964).

[111] M.D. Daybell and W.A. Steyert, 'Localized magnetic impurity states in metals: Some experimental relationships', Rev. of Mod. Phys. **40**, 380 (1968).

[112] J.T. Li, W.D. Schneider, R. Berndt, and B. Delley, 'Kondo scattering observed at a single magnetic impurity', Phys. Rev. Lett. **80**, 2893 (1998).

[113] V. Madhavan, W. Chen, T. Jamneala, M.F. Crommie, and N.S. Wingreen, 'Tunneling into a single magnetic atom: Spectroscopic evidence of the Kondo resonance', Science **280**, 567 (1998).

[114] T. Jamneala, V. Madhavan, W. Chen, and M.F. Crommie, 'Scanning tunneling spectroscopy of transition-metal impurities at the surface of gold', Phys. Rev. B **61**, 9990 (2000).

[115] M.A. Schneider, L. Vitali, N. Knorr, and K. Kern, 'Observing the scattering phase shift of isolated Kondo impurities at surfaces', Phys. Rev. B **65**, 121406(R) (2002).

[116] H. Suhl, 'Dispersion theory of the Kondo effect', Phys. Rev. **138**, A515 (1965).

[117] M.D. Daybell in: G.T. Rado and H. Suhl (eds.) (eds.), *Magnetism* (Academic, New York, 1973), vol. V, chap. 4, 121.

[118] R. Tournier and A. Blandin, 'Influence of interactions between impurities on the appearance of magnetic moments in copper-cobalt dilute alloys', Phys. Rev. Lett. **24**, 397 (1970).

[119] G.J. van den Berg, 'Anomalies in dilute metallic solutions of transition elements', Prog. Low Temp. Phys. **4**, 194 (1964).

[120] M.P. Sarachik, E. Corenzwit, and L.D. Longinotti, 'Resistivity of Mo-Nb and Mo-Re Alloys containing 1% Fe', Phys. Rev. **135**, A1041 (1964).

[121] C. Zener, 'Interaction between the d-shells in the Transition Metals', Phys. Rev. **81**, 440 (1951).

[122] K. Yosida, 'Ground state energy of conduction electrons interacting with a localized spin', Prog. Theor. Phys. **36**, 875 (1966).

[123] Y. Nagaoka, 'Self-consistent theory of low-temperature anomalies due to s-d exchange interaction', Prog. Theor. Phys. **37**, 13 (1967).

[124] P.W. Anderson, 'Localized Magnetic States in Metals', Phys. Rev. **124**, 41 (1961).

[125] J.R. Schrieffer and P.A. Wolff, 'Relation between the Anderson and Kondo Hamiltonians', Phys. Rev. **149**, 491 (1966).

[126] S. Hüfner, *Photoelectron Spectroscopy* (Springer, Berlin, Heidelberg, 2003), third edn.

[127] O. Gunnarsson and K. Schönhammer, 'Electron Spectroscopies for Ce Compounds in the Impurity Model', Phys. Rev. B **28**, 4315 (1983).

[128] O. Ujsaghy, J. Kroha, L. Szunyogh, and A. Zawadowski, 'Theory of the Fano resonance in the STM tunneling density-of-states due to a single Kondo impurity', Phys. Rev. Lett. **85**, 2557 (2000).

[129] M. Plihal and J.W. Gadzuk, 'Nonequilibrium theory of scanning tunneling spectroscopy via adsorbate resonances: Nonmagnetic and Kondo impurities', Phys. Rev. B **63**, 085404 (2001).

[130] J. Merino and O. Gunnarsson, 'Simple model for scanning tunneling spectroscopy of noble metal surfaces with adsorbed Kondo impurities', Phys. Rev. B **69**, 115404 (2004).

[131] U. Fano, 'Effects of configuration interaction on intensities and phase shifts', Phys. Rev. **124**, 1866 (1961).

[132] S. Crampin, 'Surface states as probes of buried impurities', J. Phys. Cond. Mat. **6**, L613 (1994).

[133] A. Weismann, M. Wenderoth, N. Quaas, and R.G. Ulbrich, 'Focussing of bulk electrons in Ag', submitted to Phys. Rev .

[134] A. Schiller and S. Hershfield, 'Theory of scanning tunneling spectroscopy of a magnetic adatom on a metallic surface', Phys. Rev. B **61**, 9036 (2000).

[135] V. Madhavan, W. Chen, T. Jamneala, M.F. Crommie, and N.S. Wingreen, 'Local Spectroscopy of a Kondo impurity: Co on Au(111)', Phys. Rev. B **64**, 165412 (2001).

[136] T. Nishizawa and K. Ishida, Bulletin of Alloy Phase Diagrams **5**, 161 (1984).

[137] J. de la Figuera, J.E. Prieto, C. Ocal, and R. Miranda, 'Surface etching and enhanced diffusion during the early stages of the growth of Co on Cu(111)', Surf. Sci. **307-309**, 538 (1994).

[138] J.E. Prieto, J. de la Figuera, and R. Miranda, 'Surface energetics in a heteroepitaxial model system: Co/Cu(111)', Phys. Rev. B **62**, 2126 (2000).

[139] M.Ø. Pedersen, I.A. Bönicke, E. Lægsgaard, I. Stensgaard, A. Ruban, J.K. Nørskov, and F. Besenbacher, 'Growth of Co on Cu(111): subsurface growth of trilayer Co islands', Surf. Sci. **387**, 86 (1997).

[140] R. Robles, R.C. Longo, A. Vega, C. Rey, V. Stepanyuk, and L.J. Gallego, 'Magnetic magic numbers are not magic for clusters embedded in noble metals', Phys. Rev. B **66**, 064410 (2002).

[141] O. Kurnosikov, J.T. Kohlhepp, and W.J.M. deJonge, 'Displacement of Co atoms embedded in a Cu(001) surface', in 'Book of Abstracts, 12th International Conference on STM/STS and related Techniques', (Eindhoven, 2003).

[142] C.Y. Lin, A.H. Castro Neto, and B.A. Jones, 'Microscopic theory of the single impurity surface Kondo resonance', arXiv: cond-mat/0307185 (2003). To be published in Phys. Rev. B.

[143] S. Crampin, M. Nevokee, and J.E. Inglesfield, 'Embedding method for confined quantum systems', Phys. Rev. B **51**, 7318 (1995).

Lebenslauf

Name:	Norbert Quaas
Familienstand:	verheiratet, ein Kind
Nationalität:	deutsch
Geboren am:	16. Januar 1970
Geburtsort:	Bremen

08-1986 bis 05-1989:	Gymnasiale Oberstufe und Abitur, Gymnasium am Leibnizplatz, Bremen.
09-1989 bis 03-1990:	Hochschulpraktikum Elektrotechnik, Siemens AG, Bremen.
03-1990 bis 07-1990:	Technische Aushilfstätigkeit, Bereich Automatisierung, Siemens AG, Bremen.
10-1990 bis 09-1992:	Grundstudium Physik und Vordiplom, Universität Bremen.
10-1992 bis 08-1993:	Hauptstudium Physik, Universität Göttingen.
09-1993 bis 06-1994:	Visiting Student, McGill University, Montreal, Quebec (Kanada).
10-1994 bis 06-1997:	Hauptstudium Physik und Diplomarbeit am Max-Planck-Institut für Strömungsforschung im Rahmen des SFB 357. Thema der Arbeit: Spektroskopie an kalten Metallclustern eingelagert in Heliumtröpfchen. Diplom der Universität Göttingen am 26.6.1997.
09-1997 bis 11-1998:	Wissenschaftlicher Mitarbeiter am Max-Planck-Institut für Strömungsforschung. Untersuchung von ultrakalten Metall- und van-der-Waals-Clustern.
12-1998 bis 12-2003:	Wissenschaftlicher Mitarbeiter und Doktorand am IV. Physikalischen Institut der Universität Göttingen. Untersuchung von Metalloberflächen mit dem STM und verwandten Techniken im Rahmen des SFB 345 und 602.
Seit 02-2004:	Wissenschaftlicher Mitarbeiter am Max-Planck-Institut für biophysikalische Chemie, Abteilung Nanobiophotonik. Experimentelle Untersuchung von Konzepten zur Überwindung des Beugungslimits in der optischen Mikroskopie.

Danksagung

Am Ende einer langen und am Schluß auch spannenden Zeit möchte ich hier all den zahlreichen Leuten danken, die großen Anteil an deren Erfolg gehabt haben.